XFEL.EU TR-2012-006

## TECHNICAL DESIGN REPORT

# X-Ray Optics and Beam Transport

December 2012

*H. Sinn, M. Dommach, X. Dong, D. La Civita,*
*L. Samoylova, R. Villanueva, and F. Yang*
*for X-Ray Optics and Beam Transport (WP73)*
*at the European XFEL*

**European X-Ray Free-Electron Laser Facility GmbH**
Albert-Einstein-Ring 19
22761 Hamburg
Germany

# Contents

# Introduction

This report describes the technical realization of the X-ray beam transport systems presented in the *Conceptual Design Report: X-Ray Optics and Beam Transport,* 2011 [1] (referred to as “CDR2011” in the following text).

After a short update on the conceptual design, the sequence of X-ray optical components and the ray-tracing layout, including relevant beams and apertures, are discussed for each beamline. This is followed by a discussion of radiation safety and equipment protection: for the European XFEL facility, these are particularly relevant since a mis-steered X-ray beam can potentially burn through several millimetres of materials during one pulse train. Operational aspects that can lead to a coupling of experiments by the equipment protection system are discussed as well.

One of the main characteristics of the beam transport systems is the use of 800 mm long mirrors to offset and distribute the beam. The performance of the beamlines depends critically on these mirrors since profile errors and unwanted deformations on the order of a few nanometres, due to mounting and heat load, will cause noticeable beam distortions. A prototype development for these mirrors is discussed as well as the design of the mirror chambers, which face high requirements in terms of vibration stability and motion capabilities at the best possible UHV conditions.

An important conceptual change with respect to CDR2011 was done in the choice of the soft X-ray monochromator design. While the previous design was in the horizontal geometry and more optimized towards higher energy resolution, the new design is now focused more on a faster time response. The vertical in-line geometry makes a monochromatic beam now equally available to all three branch beamlines at SASE3.

The cryogenically cooled silicon monochromator for hard X-rays was designed on the basis of an artificial channel-cut monochromator developed by Argonne National Laboratory. In contrast to the previous design, the angular range was extended, and cooling tests were performed on a test setup.

The vacuum system, consisting of a more than 2.5 km long beam transport, will be built mostly from 18 m long units, which are assembled by orbital welding inside the tunnels. The pump-down of these large systems and the interface to the accelerator vacuum and experiment vacuum are discussed. A gas attenuator system for the SASE3 beamline is presented and will be tested and optimized.

Several other beamline components, which will be close to existing designs developed for storage ring optics, are then briefly discussed.

Finally, the CAD integration process that is used to avoid collisions with other installation throughout the construction project is presented shortly.

In the appendices, a collection of ray-tracing plots is given, as well as a list of links to other technical documents related to this report and a project plan.

# 1 Design of beam transport systems

The conceptual design with respect to CDR2011 remains mostly unchanged.

However, a further development of the design of the instruments in the experiment hall led to some adjustments:

1. It was decided that only two branches will be built at the SASE1 beamline. The third instrument, Serial Femtosecond Crystallography (SFX), which is currently proposed by a user consortium, will be positioned behind the Single Particles, Clusters, and Biomolecules (SPB) instrument, using the same beam transport.
2. To improve the beam stability, the hard X-ray monochromators will now be positioned closer to the experiments, either at the very end of the photon tunnels or directly inside the experiment hall. To compensate for the vertical offset, the beam will be steered vertically by the second offset mirror or the distribution mirror. For the Femtosecond X-ray Experiments (FXE) instrument, a four-bounce configuration is foreseen for the monochromator, which keeps the beam offset constant.
3. The intermediate, horizontal focus (or collimated beam), which is needed to transport the full beam footprint over the distribution mirrors, can now be generated also by beryllium compound refractive lenses (CRLs) in the case of the FXE and Materials Imaging and Dynamics (MID) experiments. The capability of generating this focus with the second offset mirror remains. However, since the microfocusing at these experiments will be done also with spherical CRLs, an astigmatism coming from the mirror's intermediate focus would lead to unsatisfactory focusing results. Also, the use of upstream CRLs offers the advantage of pre-collimation in the vertical plane, which is otherwise impossible for the hard X-ray beamlines.

**4** As discussed in the introduction, the concept of the soft X-ray monochromator was modified and will be presented later in a dedicated section.

**5** The range of grazing-incidence angles at the SASE3 offset mirrors was changed from 9–25 mrad to 6–20 mrad. The main reason is the smaller wavefront distortion coming from shape errors of the mirrors. Also, by decreasing the smallest possible offset mirror angle, the Small Quantum System (SQS) experiment could now receive pink beam up to nearly 4 keV.

**6** Due to the slight reduction of offset angles for SASE3 (which still meets the requirements formulated in CDR2011), the horizontal offset variation at all beamlines could be limited to less than 80 mm. This led to a unified design of the mirror chambers for all offset and distribution mirrors.

**7** The beam offset direction for all SASE beamlines was oriented such that the deflection of the first mirror is directed towards the closer tunnel wall, away from the transport path. In this way, unwanted heating of the driving mechanics for the pitch angle by Compton radiation can be significantly reduced.

# X-ray optical design

A schematic layout of the three beamlines associated with the undulators SASE1, SASE2, and SASE3 is shown in Figure 1. In the following, the expressions “SASE1”, etc. are used jointly for undulators, beam transport systems and the corresponding experiment areas. The southbound direction is “+*x*” in the European XFEL coordinate systems, the downstream direction of the beam is “+*z*”, and “+*y*” is vertically up.

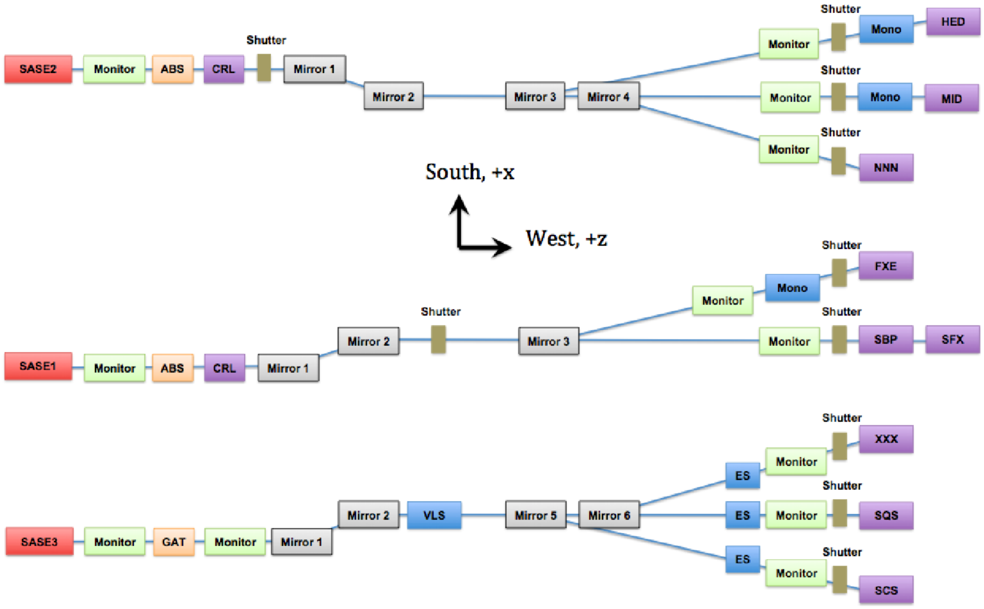

***Figure 1:*** *Layout of the three SASE beamlines. The distances of the components are not to scale, but the beamlines are arranged such that the relative positions of the experiments correspond to their sequence in the experiment hall.*

The components labelled “Monitor” indicate a combination of gas-based beam position and intensity monitor systems (X-ray beam position monitors (XBPM) and X-ray gas monitor detectors (XGMD) [2]. “ABS” at SASE1 and SASE2 are removable, water-cooled, solid-state beam attenuators. For the soft X-ray beamline SASE3, a gas attenuator (“GAT”) is used instead. The offset mirrors M1 and M2 work with a variable offset: 25–85 mm at SASE1 and SASE2, and 35–115 mm at SASE3. At the locations of the shaft buildings, SASE1 and SASE2 have intermediate shutters that separate the undulator tunnels and shaft buildings upstream from the photon tunnels downstream. Because the distance to the source point would otherwise be too large, a significant part of the SASE1 X-ray optics has been moved into the undulator tunnel.

The downstream mirrors shown in grey in Figure 1 are the distribution mirrors that can be moved into the beam to direct it to the branch instrument stations. Only one of the up to three instrument ports can receive beam at the same time.

The hard X-ray monochromators (“Mono”) are located at the very end of the photon tunnels or directly at the instruments in the experiment hall. The soft

X-ray monochromator consists of a varied line space (VLS) grating upstream of the distribution mirrors and the exit slits ("ES"). In contrast to the hard X-ray beamlines SASE1 and SASE2, where each experiment has a dedicated monochromator, all instrument stations at SASE3 can use the VLS monochromator.

# Beamline components

The sequence of X-ray optical components for SASE1 is shown in more detail in Figure 2. All components for which the X-ray Optics and Beam Transport group (WP73) is responsible are shown in grey. Components under the responsibility of the Undulator Vacuum group (WP19) are shown in orange, of the X-Ray Diagnostics group (WP74) in green, and the instruments in blue. Components that are foreseen as placeholders, but not budgeted, are white.

One difference compared to CDR2011 is the sequence of diagnostics elements for the hard X-ray beamlines (Figure 2, Figure 3): one pair of XBPM and XGMD monitors is moved to the back of the beamline. This will enable more precise information on the intensity and beam position right before the experiments. On the other hand, the pointing information of the beam from the undulator must now be derived from the combination of one XBPM and one electron beam position monitor or one of the X-ray screens.

At the SASE3 beamline (Figure 4), two gas monitor sections are located around the gas attenuator in order to be able to measure the gas absorption precisely after a pressure change. The gas diagnostics section at the end of the beamlines is foreseen as an upgrade option—similar at the branch beamlines of SASE1 and SASE2.

The detailed position of each component is maintained in an Excel list, which is updated every six months ("Component list": EDMS D*2278111).

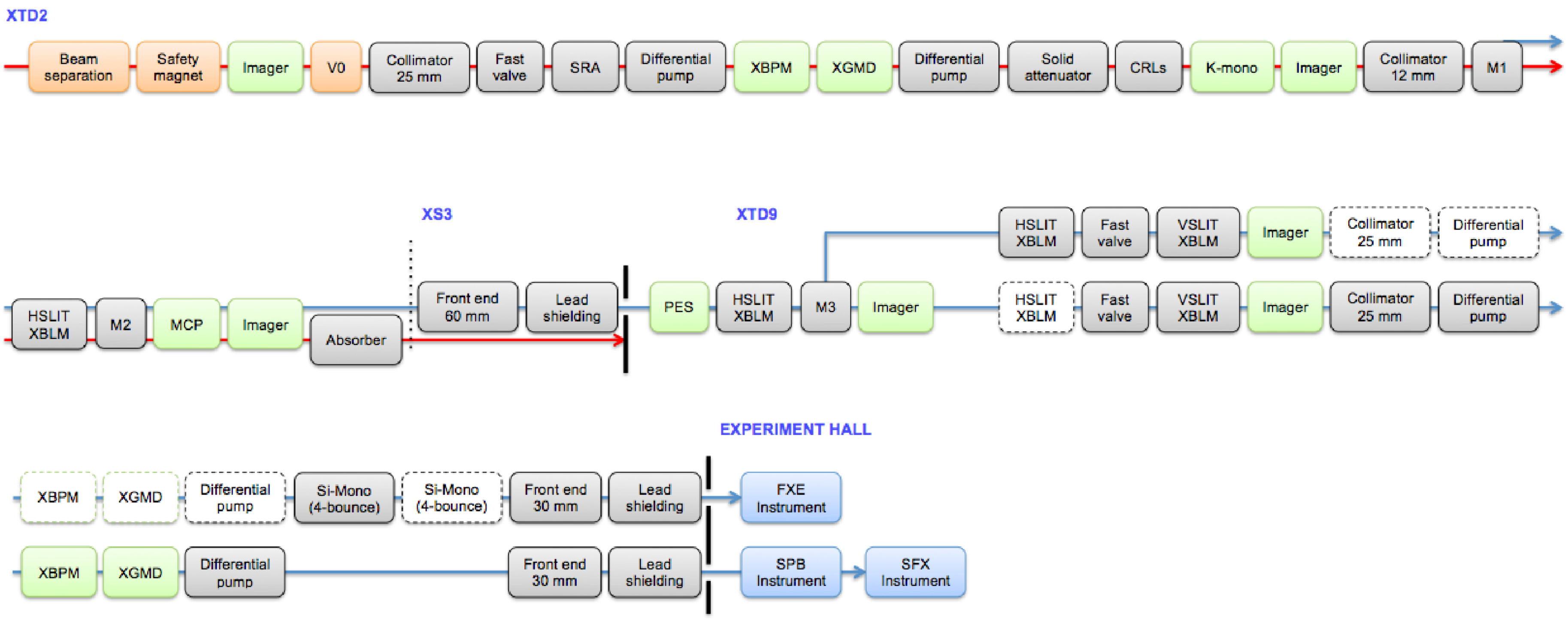

***Figure 2:*** *SASE1 beamline components*

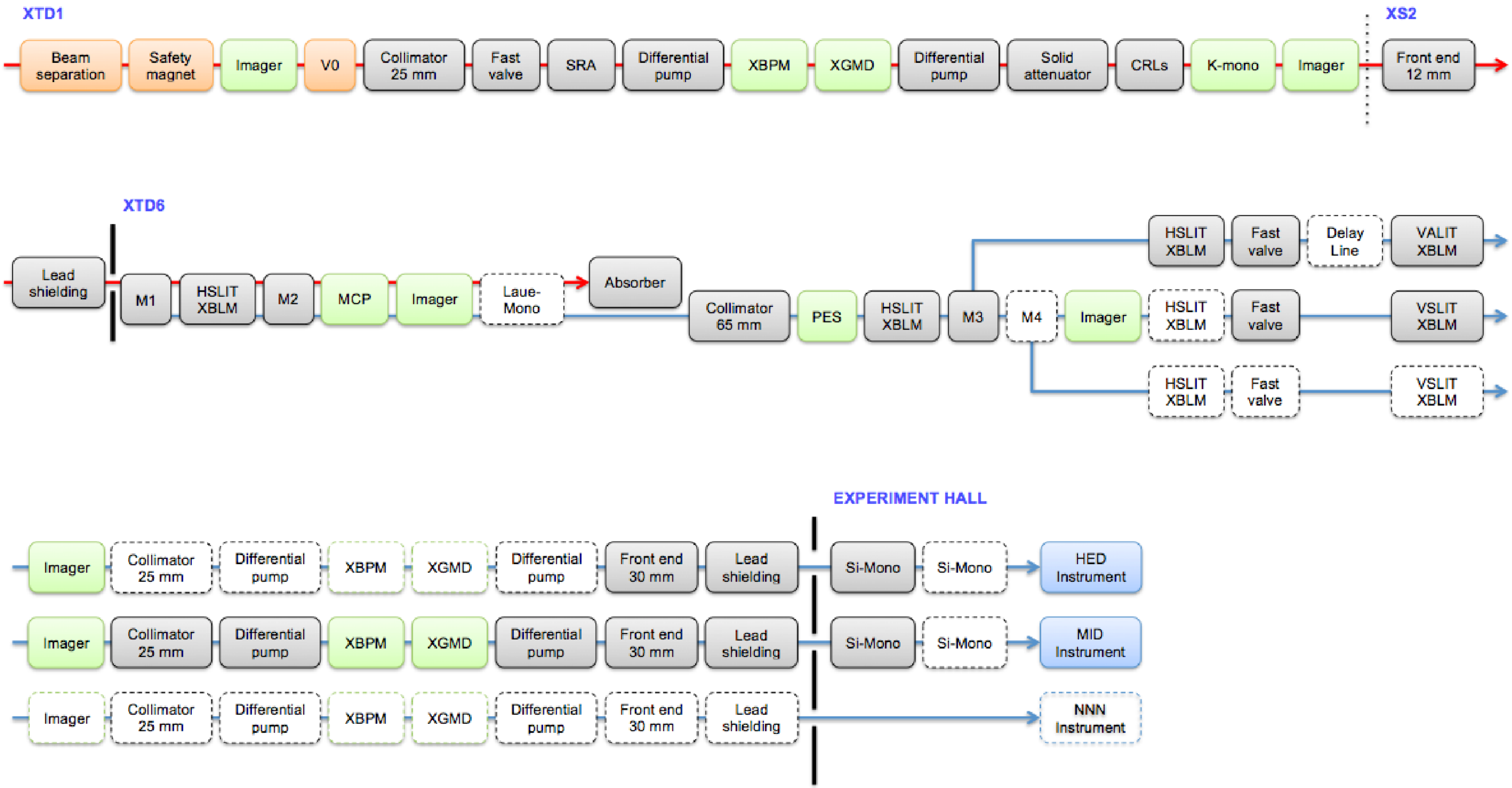

***Figure 3:*** *SASE2 beamline components*

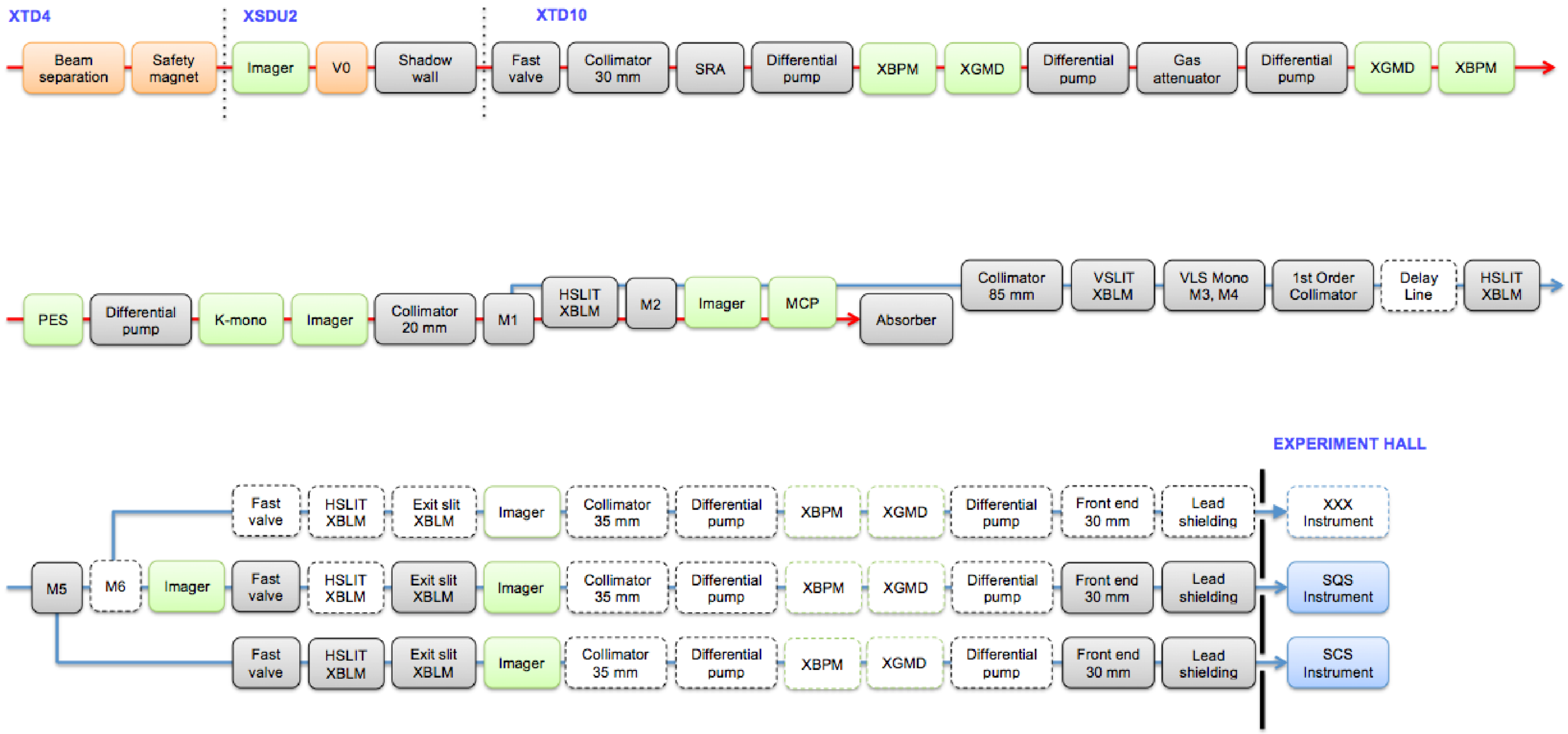

*Figure 4*: *SASE3 beamline components*

# Ray tracing

To precisely define the size and position of apertures and beam pipes, a quantitative ray tracing is required. Unfortunately, the 3D CAD model of the beamlines is not suited for this since it is segmented into sections that are about 50 m long due to its large size. Instead, 2D cuts in the horizontal and vertical plane are used for ray tracing. To be able to plot the entire beam transport system at once, the *z*-axis (beam direction) is compressed by a factor of 2000 (SASE1 and SASE2) or 1000 (SASE3), while the *x*-axis perpendicular to the beam is scaled 1:1.

Examples for such a plot for the SPB instrument at SASE1 are shown in Figure 5 and Figure 6. The beam pipes and fixed apertures for radiation safety (for example, tungsten collimators protected by boron carbide $B_4C$) are shown in black. The beam coming from the undulator is shown in red. Before the offset mirrors, rays in all directions are considered, while the offset mirrors limit the angular range. Two beam offsets are considered: the large horizontal offset corresponds to the low photon energy boundary (3 keV for SASE1 and SASE2, and 270 eV for SASE3) and the small offset to the higher boundary (24 keV for SASE1 and SASE2, and 3 keV for SASE3). The beam sizes in the experiment hall are defined by the cutoff from the offset mirror and the minimum and maximum angular position. The beam shift of the offset mirrors generates virtual sources, which are shown as vertically displaced undulator sources in the plot.

Apertures shown in blue are $B_4C$ apertures for beam guiding and equipment protection purposes. Some of these apertures are movable and follow the adjustable beam offset as indicated with arrows.

A complete set of ray-tracing diagrams for all beamlines and experiments is shown in Appendix A and in EDMS D*3004861.

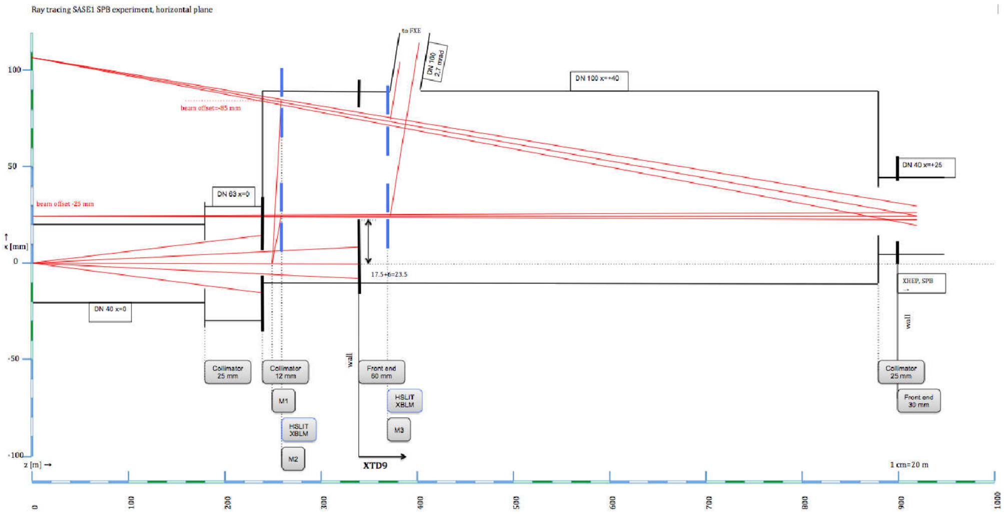

*Figure 5*: *SASE1 ray tracing for SPB instrument in the horizontal plane*

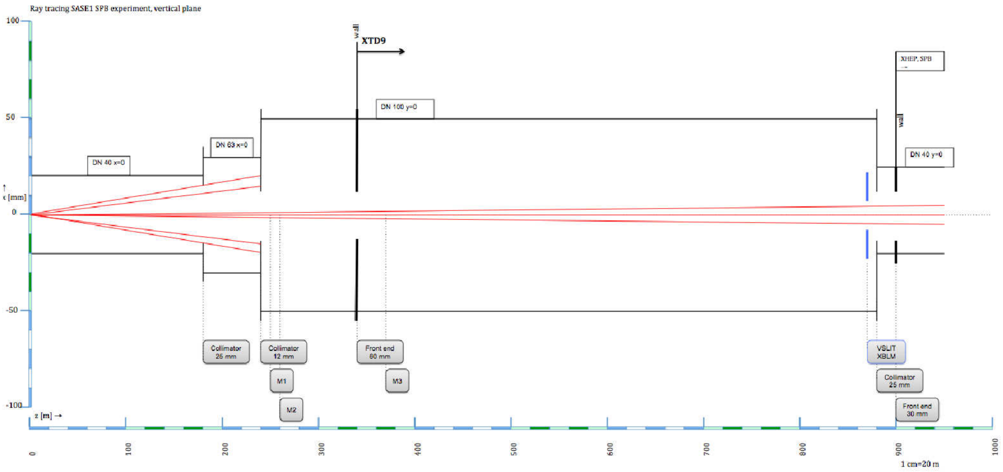

*Figure 6*: *SASE1 ray tracing for SPB instrument in the vertical plane*

# 2 Operation and safety

Radiation safety includes all measures to protect people from harmful radiation. For example, people will work during operation in the experiment hall or inside of a radiation safety hutch with the photon shutter closed. The shielding requirements are defined by the DESY radiation protection group and—as far as they concern the beam transport—are explained in the next section.

The aim of the equipment protection systems is to minimize failures and downtimes due to equipment damaged by a mis-steered or too intense FEL beam. A failure of the equipment protection system should in no case compromise the radiation safety.

## Radiation safety

Several sources of radiation are considered: bremsstrahlung created by the electron beam hitting residual gas in the electron beamline, bremsstrahlung from a target, like a closed valve inside the undulator section, spontaneous (synchrotron) radiation, and FEL radiation. The precise shielding and radiation protection requirements are currently calculated by the DESY group and refined as the technical design of the beam transports and the experiments advances.

So far, the following guidelines were developed:

- To protect the experiment hall against the very hard bremsstrahlung and spontaneous radiation, a minimum beam offset of 25 mm (SASE1 and SASE2) or 35 mm (SASE3) has to be introduced.
- The shutters and shielding requirements towards the experiment hall should match the effective thickness of the labyrinth wall of 1 m normal concrete. This corresponds to about 8 cm of tungsten for the scattered bremsstrahlung and the X-ray spectrum considered.

- The shutters and shielding requirements in the shaft buildings should match the labyrinth walls of 1.35 m heavy concrete, corresponding to about 20 cm of tungsten. Here the bremsstrahlung on the electron beam axis has to be absorbed.
- The FEL beam stops relevant for radiation safety are built as “burn-through absorbers”. This means that, even if the FEL beam were to burn through the beam stop, a vacuum leak will be generated triggering a shutdown of the accelerator.
- The shielding of the experiment radiation safety hutches depends strongly on the minimum transport mirror angles and their coatings. For the current beam transport design, wall thicknesses between $\leq$1 mm steel (SCS station) and 10 mm steel + 17 mm lead (SPB back wall) are required.

## Equipment protection

Conceptually, there are three safety layers to protect hardware against damage:

1. Passive protection of all parts that can directly see the beam by water-cooled $B_4C$ or diamond. All beam-defining apertures and beam absorbers will be made out of $B_4C$.
2. Preventive protection of certain components by the implementation of beam modes. Not all parts can be protected by $B_4C$, for example the silicon monochromator, a YAG screen, or a silicon diode. As shown below, even water-cooled $B_4C$ cannot survive direct exposure to full pulse trains under all conditions. Therefore, depending on the status of the beam transport system, only a certain maximum beam power is allowed.
3. Active protection by monitors. Thermocouples will be placed at most components and allow the monitoring of average heat load effects, comparing it to FEA calculations or tests. However, the extreme temperature cycling of a hot spot exposed to a direct hit from a pulse train is invisible to a thermal sensor a few mm away. Therefore, fast X-ray beam loss monitors that can detect a mis-steered beam and shut down

the beam delivery even within one pulse train will be used at several places.

A schematic of the beam transport equipment protection system and the interaction with other control systems is shown in Figure 7.

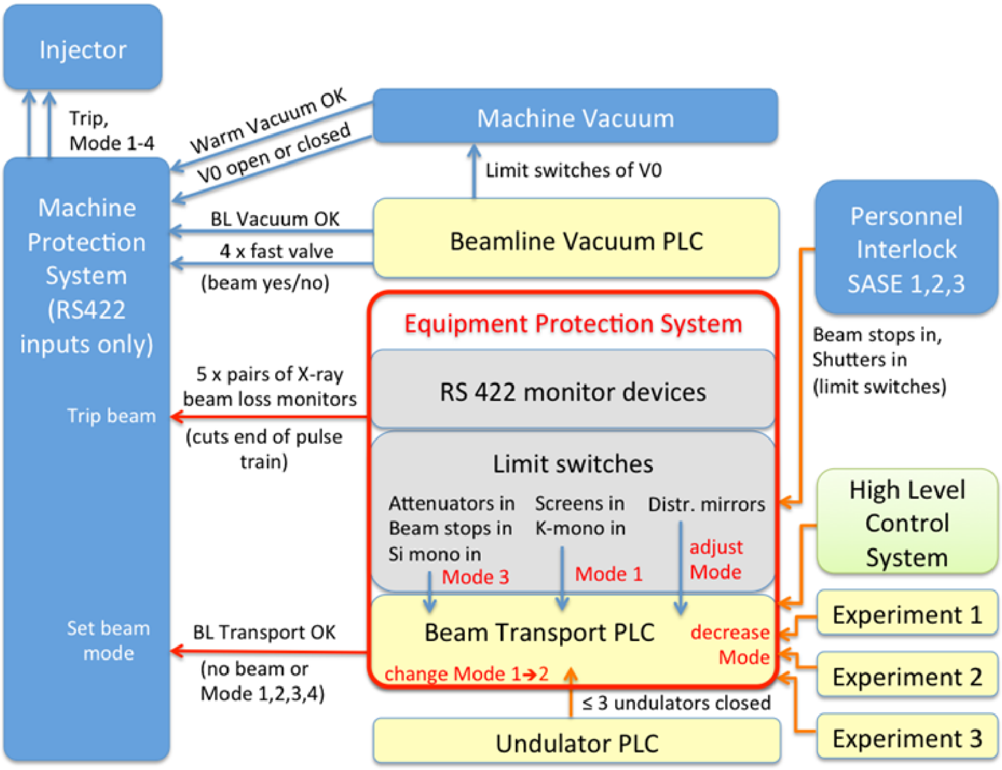

***Figure 7***: *Equipment protection system for a beam transport*

Apart from binary conditions, like the tripping of a beam loss monitor or activation of a limit switch, more complex situations might occur, for example the focusing of a beryllium CRL onto a slit or shutter at the hard X-ray beamlines or the positioning of the horizontal focus at the SASE3 beamline at the vertical exit slit via the adaptive mirror. For these cases, watchdog functions on the higher-level control system could be implemented, making it possible to reduce the beam mode under certain critical alignment conditions (Figure 8) on a slow time scale.

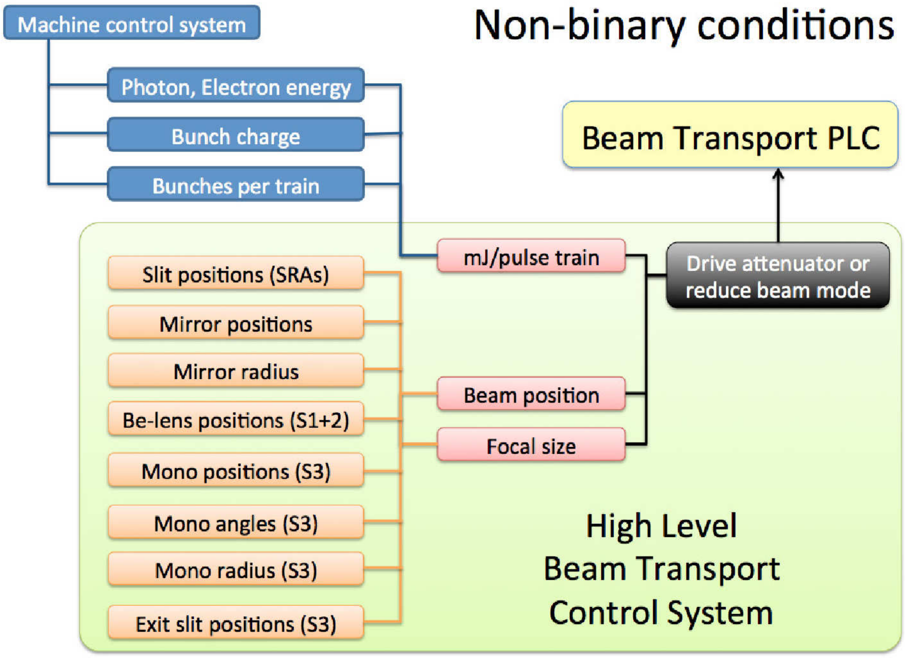

***Figure 8****: Higher-level macros could be used to reduce the allowed beam mode if a critical condition is reached.*

# Beam modes and operation

When, for example, a fluorescence screen is driven into the beam or a monochromator is inserted, limit switches are activated and the beam transport control system notifies the machine protection system that a certain beam power coming into the beamline should not be exceeded. These discrete power levels are called beam modes and have to be defined uniformly for the accelerator and all beamlines. Currently, the following beam modes are being discussed with the machine protection system group at DESY (Table 1).

***Table 1:*** *Proposed definition of beam modes. The numbers indicate the maximum number of allowed pulses within one pulse train. Modes highlighted in green were proposed for the accelerator, while the others are additionally proposed for the X-ray beamlines.*

| | ≤ 0.1 nC | ≤ 0.25 nC | ≤ 1nC | > 1nC |
|---|---|---|---|---|
| Mode 1 | 1 | 1 | 1 | 1 |
| Mode 2 | 600 | 200 | 30 | 1 |
| Mode 3 | 2700 | 1350 | 200 | 10 |
| Mode 4 | 2700 | 2700 | < 2700 | < 2700 |

*Mode 1*: Basic commissioning mode of accelerator, beam transport and experiments. With one pulse per pulse train (10 Hz operation), even a missteered beam should not be able to destroy components of the beam transport.

*Mode 2*: Basic commissioning mode of the accelerator with pulse trains (30 pulses). For the beam transport, we propose to make this mode charge-dependent, so it can be used to run experiments with a diamond window in air (FXE and MID).

*Mode 3*: This mode is requested from the beam transport. It is essentially defined by the number of pulses that a water-cooled piece of $B_4C$ can absorb without being damaged. Also, the hard X-ray monochromator and beryllium lenses work only up to Mode 3.

*Mode 4*: Full beam: The beam power is only limited by the performance of the accelerator and the electron beam dumps. Typically, only the total-reflecting mirrors can handle this beam power. X-ray beam loss monitors have to be operational and fully commissioned to reach this mode.

The machine protection system can either initiate a dump of pulses before they enter the undulator section (dump in the shaft building XS1), or change the injection pattern at the electron gun. One problem occurring with the application of beam modes is that radiators and experiments are being coupled. This is illustrated in Figure 9.

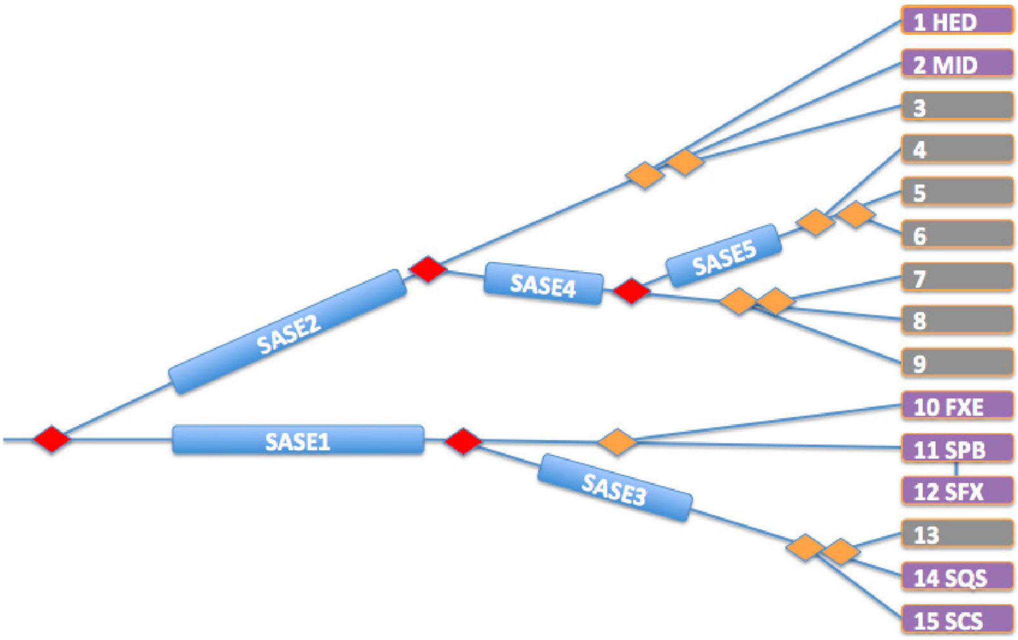

***Figure 9***: *Distribution of experiments in the startup configuration of the facility. Experiments on the same electron beamline will have to run in the same beam mode, unless the fresh-bunch technique can be fully implemented.*

If, for example, the experiment on the SASE3 beamline requires readjustment and switches to Mode 1, SASE1 will also be affected. And vice versa, if SASE1 runs with a silicon monochromator or uses Mode 2 to protect a diamond window, SASE3 will not get the full pulse pattern. A way out of this is the "fresh-bunch" technique [3], in which a particular bunch will be kicked out of the lasing orbit e.g. in SASE1 and kicked back later to lase in SASE3. Whether this will be technically possible and reliable enough to tie into the machine protection has to be shown once the facility is in operation. However, at least from the architecture of the machine protection system, it is foreseen that this decoupling with respect to beam modes will be possible.

A particular challenge for the European XFEL will be the simultaneous lasing in three or more undulators fed by the same accelerator. To obtain stability during operation, it is likely that the bunch pattern distribution over the electron beamlines will be fixed at least over one week of user operation and that the accelerator will run with a constant repetition rate (for example, 4.5 MHz or 1 MHz). Examples for splitting of the entire pulse train with and without fresh-bunch technique are shown in Figure 10. Pulses that are not desired by an experiment or rejected by the equipment or machine protection system could then be dumped into the XS1 electron dump before the undulator section. However, the dump limit for each of the three electron dumps has to be respected. With 1 nC per bunch and 10 Hz operation, this corresponds to a maximum of 1714 bunches (300 kW and 17.5 GeV). In the example in Figure 10, in the lower panel, this would mean that, if the experiments at SASE1 and SASE3 both switched to Mode 1, the pulse pattern in the injector would have to be altered since the limit of the XS1 electron dump would be exceeded. This could lead to crosstalk with the lasing performance also in SASE2, since bunches are removed from the leading edge of the train and are not available for feedback stabilization. An advantage of running the facility at lower electron energy, bunch charge, or repetition rate would be that such instabilities could be avoided, if the first electron dump were able to absorb the full pulse train.

A request from the experiments is to choose the bunch pattern freely and directly, without special request to the operator. This is important if a certain bunch pattern (for example, a logarithmic distribution or two bunches at a certain distance) is related to the underlying physics of the experiment. As discussed above, this could be implemented by fixing the pulse pattern at the injector (to obtain operational stability) but dumping unwanted bunches in the dump in XS1. If such a “bunch selection tool” would be available, accessible through the beam transport control system, and tied into the machine protection system, it could also simplify the definition of the required beam modes in Table 1, since the equipment protection system could then directly limit the number of bunches, without switching back the beam mode.

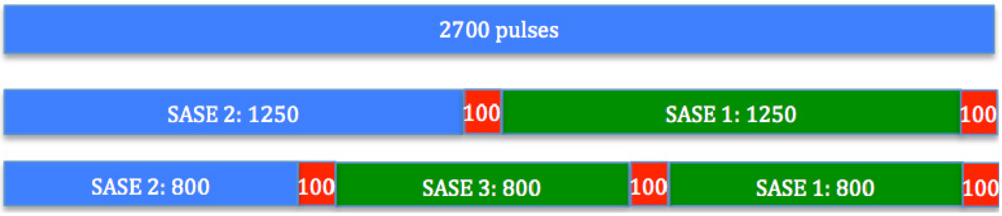

***Figure 10***: *Examples of possible bunch distribution schemes for one train without fresh-bunch technique (middle panel) and with fresh-bunch technique (lower panel) for equally distributed pulse numbers for each station. The pulses marked in red are used for feedback or are lost during the switching.*

# X-ray beam loss monitors

X-ray beam loss monitors are of particular importance for running a beamline with full beam (Mode 4). These monitors are based on electron beam loss monitors, developed by the Standard e-Beam Diagnostics group (WP17) to detect a loss of the electron beam in a section of the accelerator or undulator. The basic functionality of the X-ray beam loss monitor is shown in Figure 11: a mis-steered photon beam hits a fluorescing material (for example, CVD diamond or YAG crystal). Some of the optical photons generated will go through an optical window and hit a photomultiplier. A rough estimate leads to a sensitivity of 10 µJ/pulse or better for a 20 keV photon beam and 0.5 mm thick diamond. With the readout electronics developed by WP17, it is possible to set triggers for a maximum pulse number above a certain threshold, which would induce the device to send a trip signal to the electron gun or a fast kicker via the machine protection system. In this way, it is possible to stop the accelerator even during one pulse train; however, at least 30 pulses will pass due to the runtime of the signals.

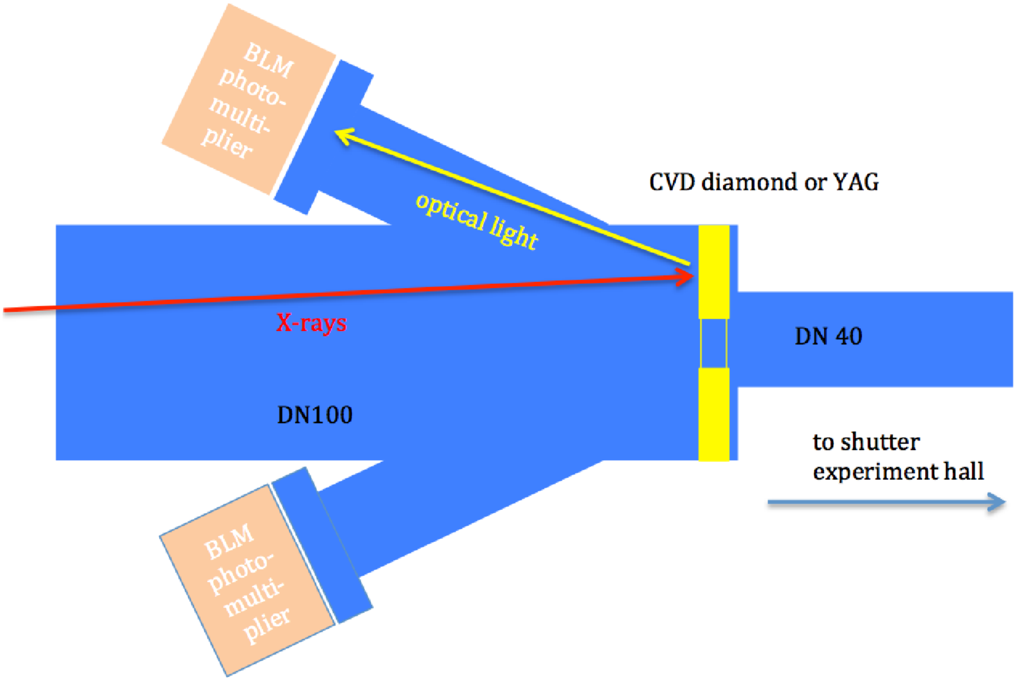

***Figure 11:*** *X-ray beam loss monitor*

For the photon beamlines, it is foreseen to have one X-ray beam loss monitor before the experiment hall, as sketched in Figure 11. Further beam loss monitors will be integrated into the beam-defining slit before each offset and distribution mirror.

## Damage experiments

For each optical element, there is an expectation, based on calculations or experiments, up to which power level it can withstand the FEL beam. The knowledge of these limits is vital for the design and operation of the beam transport systems: Damage thresholds of mirrors and gratings set an absolute limit to the full-beam operation in Mode 4; destruction limits of all other optical elements define the ranges of Mode 3 and lower beam mode operation. If these limits are too high, optics will be destroyed and long downtimes of beam loss for the experiments can be expected. If the limits are set too low, the scientific potential of the facility will be reduced. Over the past years, extensive destructive tests on mirror coatings have been performed. One result was that diamond-like carbon undergoes a structural phase transition well below its melting threshold [4]. Therefore, $B_4C$, where such an effect was so far not observed, is chosen instead as the baseline coating for all reflective optical elements.

Two damage mechanisms have to be considered. The “single-shot” damage threshold is typically a material constant and does not depend on cooling geometry and incidence angle. Around and below the critical angle, however, this can change, as a recent experiment on a grating structure in reflection geometry demonstrated [5]: the edges that are facing the incident beam show damage at lower beam power levels than the flat parts that are exposed under grazing incidence. This behaviour can be explained by the interplay of reflectivity and extinction depth under total-reflection conditions.

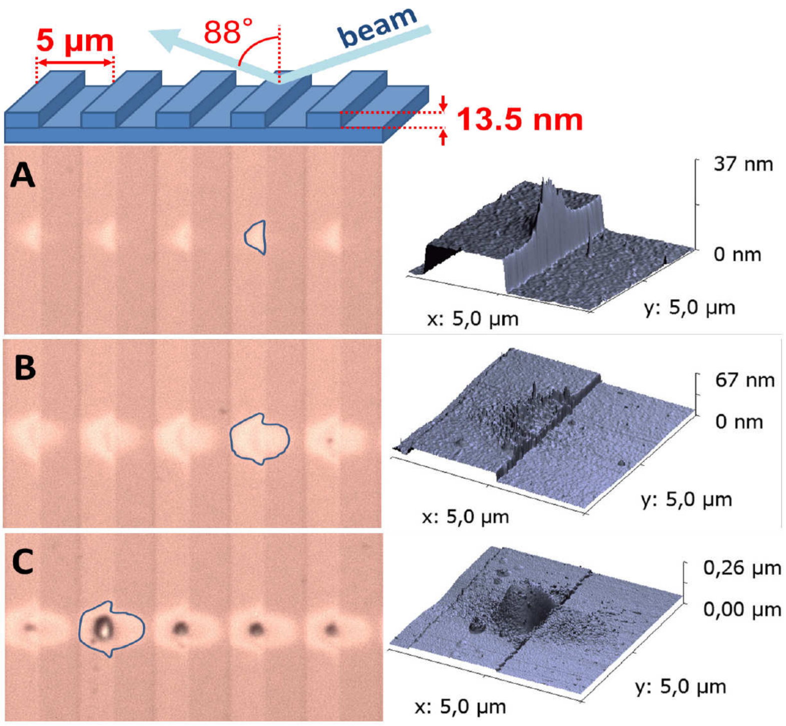

***Figure 12***: *Single-shot damage on a grating structure coated with diamond-like carbon*

The second damage mechanism comes from the local accumulation of absorbed X-ray energy in the X-ray optics. For optics in total-reflection geometry, this typically does not lead to destruction since a significant part of the absorbed heat can be removed from the hot spot in between two X-ray pulses.

One example where pulse train damage is important is the beam absorber after the offset mirrors, which is exposed to the full SASE beam if the first mirror is moved out of the beam. Figure 13 shows the total energy the optics can absorb during a 0.3 ms long pulse train. If thermal conduction is neglected in the calculations, the energy is distributed over a volume given by the footprint of the beam and the absorption depth, resulting in the single-shot melting threshold shown as a dashed line in the figure. For photon energies larger than 10 keV, the absorption length is larger than the thermal diffusion on this time scale, and the pulse train damage threshold becomes equal to the single-shot damage threshold. For lower photon energies, X-ray absorption lengths reach the range of a few µm, and a significant heat flow can build up during the 0.3 ms. This causes the pulse train damage threshold to increase with lower photon energies below 3 keV (solid blue curve and

FEA calculation). As the incidence angle is changed from normal incidence to more grazing incidence (but still above the critical angle of total reflection), the heat flow increases, and the tolerable pulse train energy shifts up significantly (red curves).

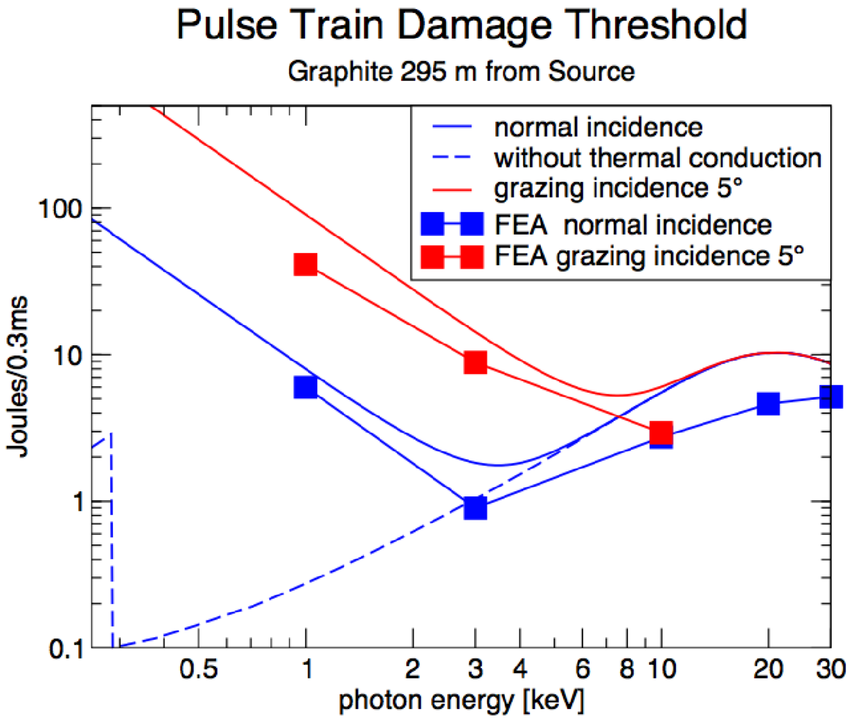

***Figure 13***: *Calculation of damage at a beam absorber. The solid lines are a one-dimensional analytical calculation with constant transport coefficients, the squares are three-dimensional FEA simulations with temperature-dependent transport properties.*

These two examples show that a precise knowledge of damage thresholds is important for the operation of the beam transports. Damage experiments during the operation phase of the European XFEL will allow us to:

- Update the beam mode definitions.
- Test functionality of the X-ray beam loss monitors (XBLMs).
- Test functionality of burn-through absorbers and measure time constants.
- Test beam stops for experiments.
- Contribute to safety and maximum efficiency in user operation.

# Alignment

The basic alignment of the beam transport systems follows methods developed for alignment of synchrotron radiation beamlines. The beam mode has to be reduced to single-pulse operation (Mode 1) to avoid damage by accidental hitting the transport pipes. After each mirror (typical distances are 10 m at SASE1 and SASE2, and 2 m at SASE3), a “pop-in monitor” will be installed (Figure 14). A fluorescence screen can be inserted, which will be able to intercept the direct beam with the mirror retracted and the beam reflected under the desired angle. Important for these pop-in monitors is a reproducible, relative distance measurement between these two beams to an accuracy of about 100 µm. In this way, the beam trajectory is defined to better than 10 mm over several 100 m, which is enough to enable capturing of the beam at the next optical element downstream the beam path. The beam profile will be shaped by slits in front of the optical element to allow a precise positioning of the optical element by scanning it through the beam and recording the shape and intensity of the reflected beam.

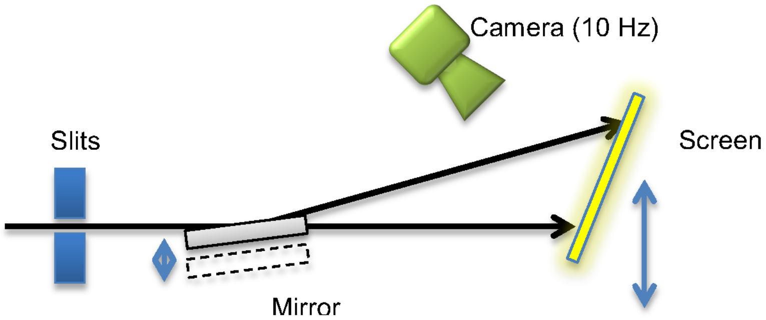

***Figure 14:** Schematic of pop-in monitor for alignment of a mirror*

The alignment of the adaptive mirrors M2 will be done with pencil beams (about 1/10 of the natural beam size) from apertures in front of the mirrors, which will illuminate different parts of the mirror. A pop-in monitor close to the intermediate focus after the distribution mirrors can be used to record the direction of each pencil beam. Because of diffraction, the beam size will be significantly enlarged (mm), which is not a problem as long as the centre of each beam can be measured with an accuracy of about 100 µm. By well-established methods of inversion of the pulse response matrix, an optimized shape of the adaptive mirror can be obtained after a few iterations. It should be noted that there are two motivations to align the adaptive mirror M2: First, a basic alignment is envisioned that corrects effective mounting and polishing errors of M1 and M2 combined. Second, in the case of long pulse train operations, an overall radius adjustment of M2 might be needed to correct heat load effects of M1.

Instead of the pencil beam method, an alignment with a wavefront sensor (for example a grating interferometer [6] or speckle imaging technique [7]) after M2 would allow a faster alignment of the piezo elements of the adaptive mirrors. However, for a precise mapping of the phase error to the local mirror deformation, the wavefront sensor should be no further away than a few metres from M2 (see estimate below). Moreover, since M2 should correct the combined profile errors of M1 and M2, it is not possible over this distance to steer the beam out of the vacuum pipe without a significant change of the M2 pitch angle, which would then increase the fraction of the M2 profile error to the total phase error in proportion to the reflection angle of M2. Therefore, a grating interferometer would have to be inserted into the beam path shortly behind M2 under UHV and particle-free conditions, which is beyond the current state-of-the-art of these devices, but can be considered as an upgrade option.

Neither the pencil beam nor the wavefront sensing method allow an alignment of the adaptive mirrors under heat load conditions. Therefore, radius adjustment compensating static heat load effects could to be done with a fluorescence screen in the experiment hall with suitable X-ray attenuators in order to protect the screen from heat load damage. An alternative would be to measure the flux through a slit at an intermediate horizontal focus of M2 with an XGMD at the end of the beamline. In this way, even dynamic deformations of the mirrors would be detectable; however, they would not be correctable with the currently foreseen hardware.

The range of spatial frequencies, which has substantial impact on the wavefront quality after propagation through the optics to the experiment hall, can be estimated within the following model. The first-order diffraction angle $\theta_d$ for a spatial frequency $1/d$, using small-angle approximation for grazing-incidence angles, is:

$$\theta_d = \theta + \Delta\theta$$
$$\sin\theta\,\Delta\theta = \lambda/d$$

That is:

$$\theta_d \approx \theta + \lambda/(d\sin\theta)$$

When this diffraction angle is less than the angular divergence of the incident beam $\delta\theta$, or the distance to the observation plane is short enough for the specularly reflected and first-order diffracted beam to overlap, a well-pronounced interference pattern can be observed. Taking into account that the beam size at distance $r$ is $\delta\theta\, r$, one can obtain the maximum difference between the specular angle and the first-order diffraction angle, $\Delta\theta = \delta\theta\,(r_1/r_2 + 1)$, and corresponding spatial frequencies:

$$1/d_\mathrm{m} = \theta\,\delta\theta / \lambda\,(r_1 + r_2)/r_2,$$
$$d_\mathrm{m} = \lambda/(\theta\,\delta\theta)\, r_2/(r_1 + r_2)$$

This means that surface errors for $d < d_\mathrm{m}$ will lead only to small-angle scattering outside the beam spot. For instance, for SASE1 offset mirrors, a photon energy of 12.4 keV, an incidence angle of 2 mrad, and a FWHM angular divergence of 2 μrad, $d_\mathrm{m} = 17.5$ mm.

The typical distance $L$ at which the wavefront sensor should be located to observe the wavefront distortions in the reflected field phase can be defined as follows: the diffraction angle $\lambda/(d\sin\theta)$, where $\lambda$ is wavelength, $\theta$ the incidence angle, and $d$ the longitudinal size of the surface feature, should be less than the observation angle for the feature $(d\sin\theta)/L$

$$L << (d\sin\theta)^2/\lambda$$

For example, for $d = 17.5$ mm, i.e. half of the distance between the actuators of the active offset mirror, a photon energy of 12.4 keV, and an incidence angle $\theta$ of 2 mrad, the distance $L$ should be less than 12.5 m.

# 3 Offset and distribution mirrors

The most critical elements for the performance of the beam transport systems are the offset and distribution mirrors, since they are required for any given experiment to receive beam. As was shown in CDR2011, shape errors play an important role, and 2 nm peak-to-valley (PV) have to be achieved over mirror lengths of 800 mm. Such PV values have been recently achieved for a 360 mm substrate [8]. A prototype with 800 mm optical length, eutectic cooling, and a bimorph bending mechanism is currently under development in collaboration with Bruker ASC. It is presented in the next section.

Also of great importance is a mirror chamber that can hold and steer the mirror precisely enough with the least possible amount of vibrations. Furthermore, the UHV environment of the mirror chambers should be as good as possible to avoid contaminations on the mirror surface. A prototype for the mirror chambers has been developed and ordered.

## Adaptive mirrors

For the beam transport systems, 11 offset and distribution mirrors are required to guide the beam to all experiments of the SASE1, SASE2, and SASE3 beamlines. The first mirror of each beamline is exposed to high-energy spontaneous radiation and will absorb up to 10 W (100 W for SASE3) of integrated beam power (see CDR2011). The static deformation can reach up to 200 nm at full beam load. Because the radiation level will be relatively high on the first mirror, the static deformation will be corrected by the second offset mirror. Also, for the branch beamlines, the second offset mirror must be able to generate an intermediate horizontal focus behind the distribution mirrors.

The idea is to make all 11 mirrors the same length and shape, and to have at least the second offset mirrors bendable and adaptive. A prototype development for such a mirror was started in 2012. The basic geometry is shown in Figure 15. The bending action is achieved by four rows of piezo actuators, glued to the bottom and top surface of the mirror substrate (design patented).

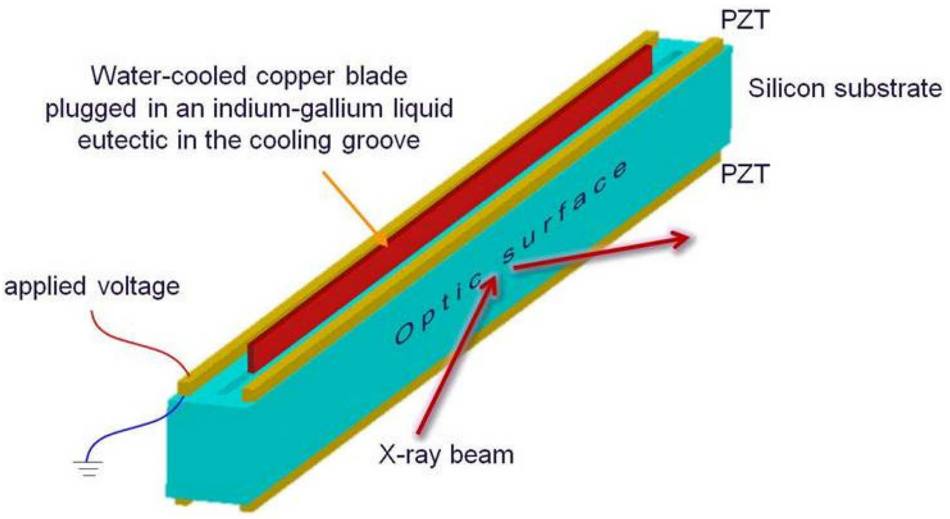

***Figure 15***: *Basic design of the adaptive mirror*

The bending properties were studied intensively with FEA calculations with respect to mirror geometry, geometry of the piezos, and properties of the glue. After subtraction of an ideal cylindrical shape from the surfaces, in the simulation the mirror already reaches a residual shape error on the order of a few nm (Figure 16). This can be further improved by fine-tuning of the individual piezo elements. In the real mirror, this fine-tuning will be also needed to correct polishing and mounting errors.

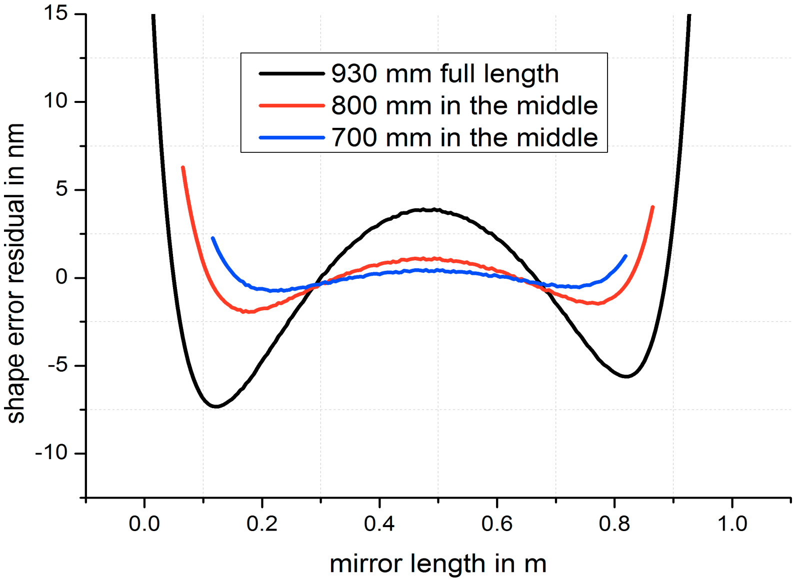

***Figure 16***: *Residual shape error after subtraction of a perfect cylindrical shape*

Cooling will be achieved by a water-cooled copper blade that is connected via an indium–gallium liquid eutectic in a groove on the top of the mirror (Figure 17).

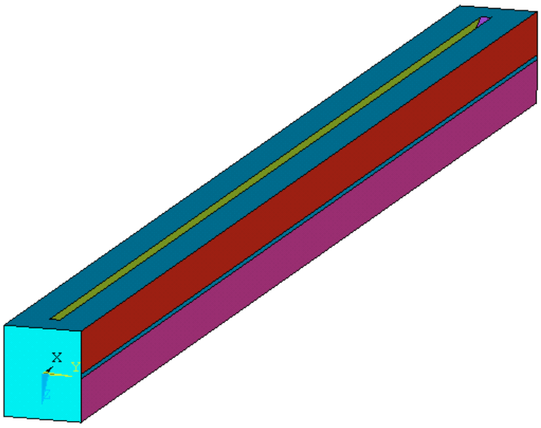

***Figure 17***: *FEA model of the mirror to simulate the effect of the cooling. The footprint of the beam (here 10 W spontaneous radiation) is shown on the side, while the eutectic cooling groove is on the top.*

The temperature profile generated on the reflecting surface assuming different heat transfer coefficients is shown in Figure 18. The resulting errors are in the range of 150 nm (Figure 19). However, by subtracting a cylindrical shape, the residual errors are in the range of less than ±1 nm (Figure 20). The pulse function showing the local bending capability by applying voltage to individual electrodes is shown in Figure 21.

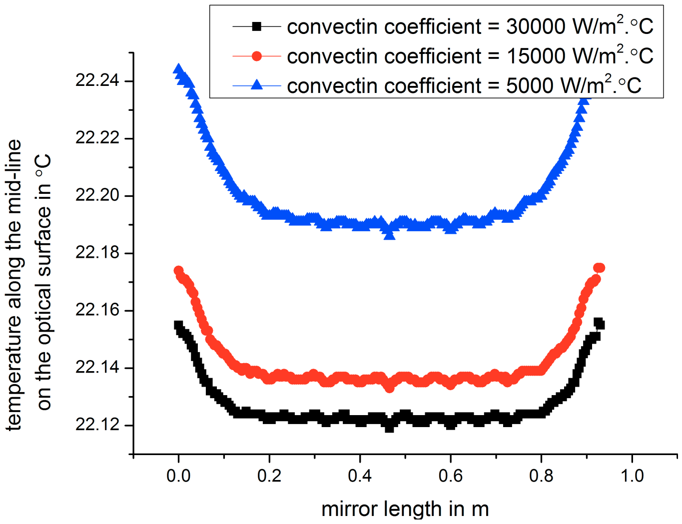

*Figure 18*: *Heat profile along the optical surface*

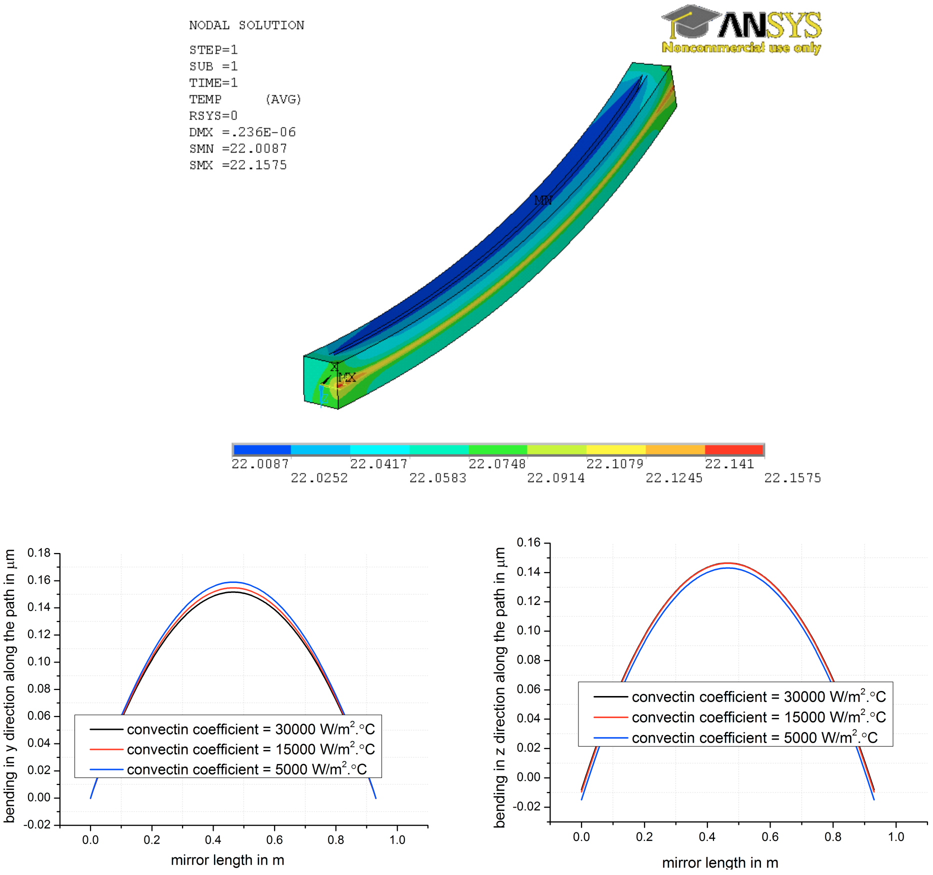

***Figure 19***: *Qualitative illustrations of the deformations. The mirror bends up and to the back in almost equal amounts (see also curves on lower panels).*

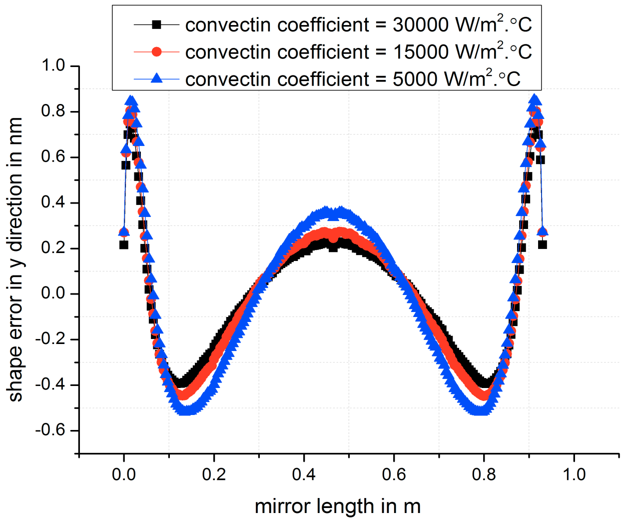

***Figure 20***: *Residual shape error after subtraction of a cylinder with radius 720 km*

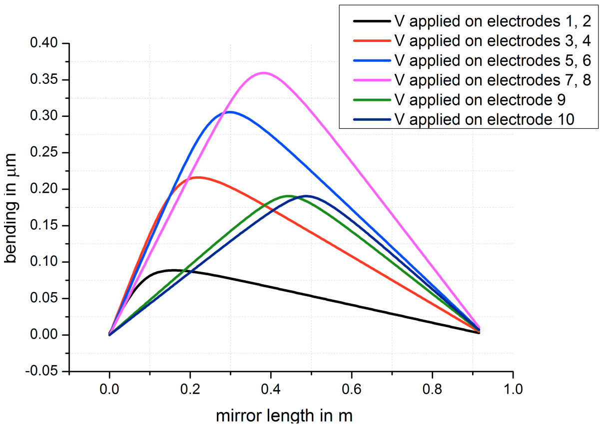

***Figure 21***: *Pulse function calculated by applying 315 V to selected electrodes*

# Mirror chambers (CHOMs)

The mirrors have to be mounted on a stable and vibration-optimized support, capable of performing all required motions. For the second offset mirrors, there is an 80 mm displacement perpendicular to the beam direction required to enable the variable offset described in CDR2011. A motion of at least 20 mm in the vertical direction enables the switching of stripes of different coating material on the mirror. Besides the pitch to control the deflection angle, a tilt motion perpendicular to the pitch enables the steering of the beam up and down at the experiment stations. In the current optical design, this motion is foreseen—besides for alignment purposes—to steer the beam downwards to the hard X-ray monochromator to compensate for the offset of the monochromator at the sample location.

To perform these motions with a maximum stiffness, the design principle of Cartesian parallel-kinematic motion was adopted in collaboration with Tino Noll, HZB BESSY. Similar to a hexapod, the substrate is supported by six struts. However, in order to minimize the crosstalk, the struts are aligned along the Cartesian axes (see Figure 22) [9], [10], [11], [12].

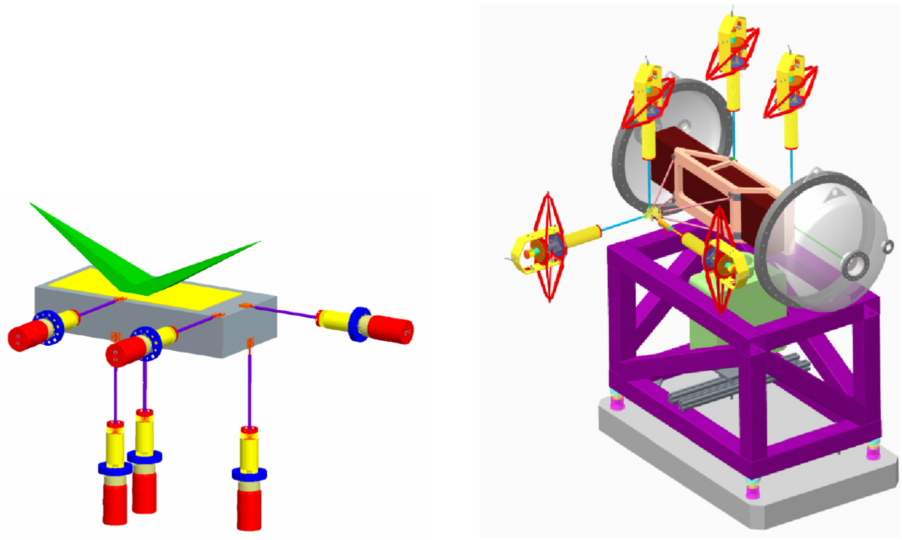

***Figure 22***: Left: *Cartesian parallel kinematics.* Right: *Implementation in the mirror chamber.*

To keep the vacuum as clean as possible from hydrocarbon contaminations, all motors and lead screws are outside of the vacuum. The vacuum chamber serves as a support for these actuators; therefore, the stability and vibration properties are important. By means of FEA simulation, the shape and the structure were optimized so that the eigenfrequencies of the chamber are as high as possible (above 90 Hz for the vacuum chamber). The deformation due to the vacuum force is up to 100 µm. However, by adding stiffeners, the deformation that acts along the critical pitch angle could be reduced to 6 µm (Figure 23). During operation, about 5% of that value could be expected from weather-related air pressure changes, which would then lead to a pitch angle variation of 0.6 µrad. At SASE2, the beam at the experiment would then move by about 700 µm. This could be compensated either by measuring the air pressure and compensating for it using a lookup table, or by interferometric measurements described in the next section.

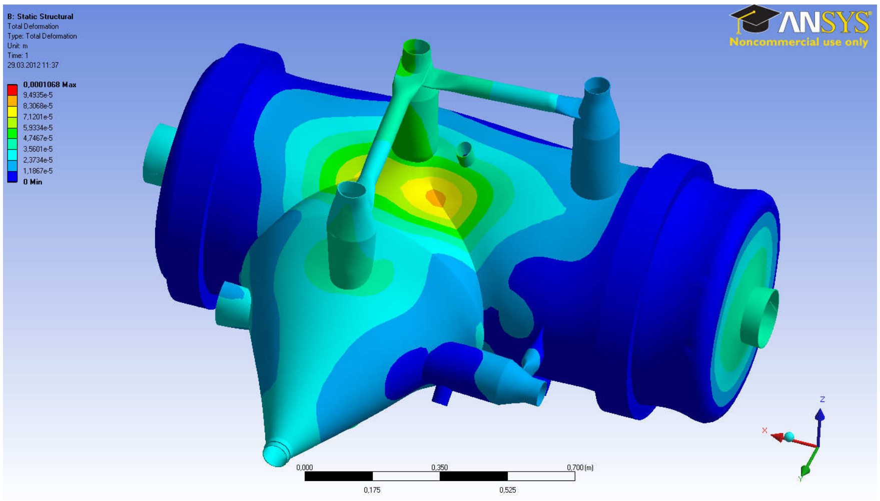

***Figure 23**: Deformation of the mirror chamber through vacuum forces*

A support of granite was chosen to optimize the vibration properties (see Figure 24). The technical specifications for the prototype chamber for horizontal offset mirror (CHOM) are described in EDMS D*3004041.

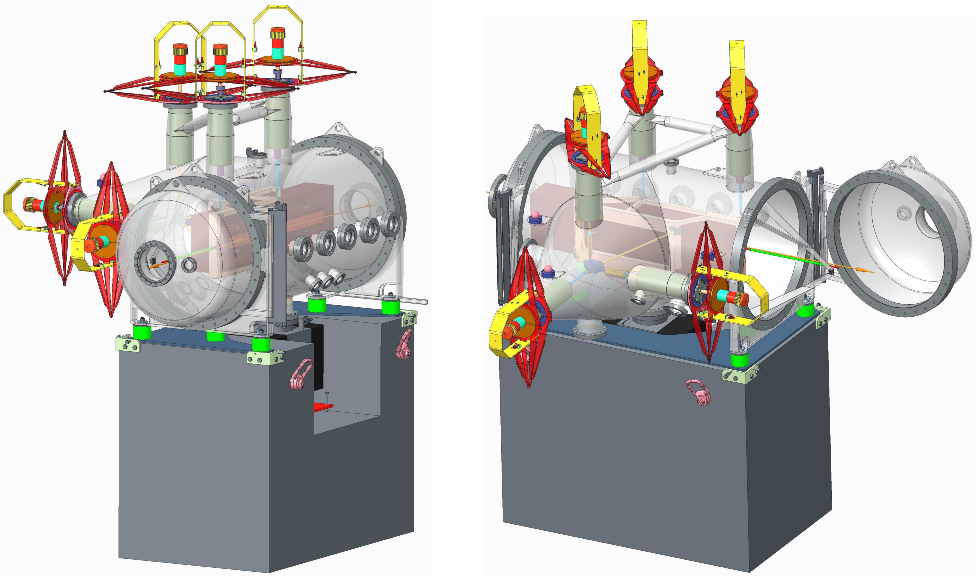

***Figure 24**: Design of the prototype mirror chamber*

# Interferometric measurements

As described above, small deformations of the vacuum chamber can be expected due to air pressure changes. Even though the chambers will be operated in temperature-controlled enclosures, changes related to temperature gradients from heat load effects—especially for the first offset mirror—are also possible. Therefore, an interferometric measurement system was implemented that will be used to characterize the prototype and, if needed, to perform corrections even during operations in the tunnels.

Figure 25 shows the setup of the interferometer, as it is envisioned for the mirror chambers. The laser beam is generated in a central He–Ne laser and split into two parts, which are guided by optical fibres to two interferometer heads. Each head consists of a double-pass interferometer and a detector (Figure 26). As the mirror pitch angle is changed, the interferometers should be able to measure the angle, ideally with a resolution and accuracy of 10 nrad. Because the angular alignment tolerance of the sensors of about 0.6 mrad (400 mm distance) is smaller than the operation range of the mirrors (2.5 mrad for SASE1 and SASE2, and 14 mrad for SASE3), the interferometer heads have to be turned accordingly. For the distribution mirrors, the angular range in pitch is sufficient; however, in order to steer the beam vertically down to compensate the offset of the hard X-ray monochromator, a tilt of the mirrors and interferometer heads in the vertical plane by about 15 mrad is required.

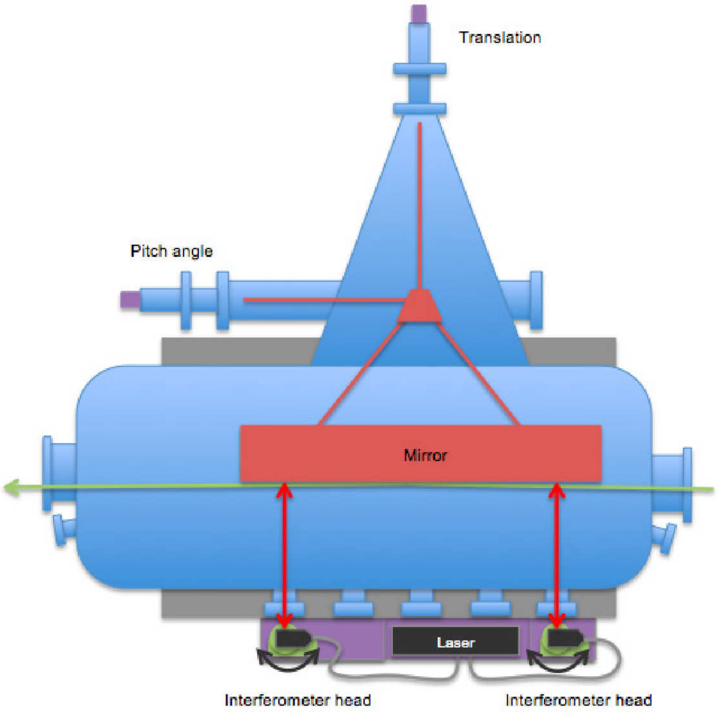

*Figure 25*: *Implementation of laser interferometer at the mirror chamber*

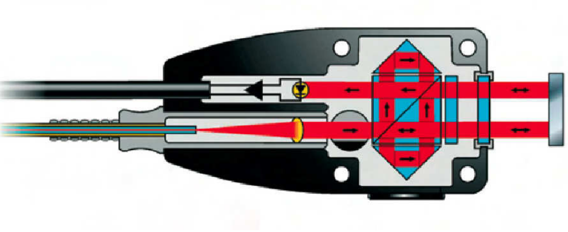

*Figure 26*: *Interferometer head (picture from www.renishaw.de)*

The basic functionalities of this measurement method were tested with a setup including a mirror dummy driven by two translation stages, and two rotation stages for the interferometer heads (Figure 27) [13].

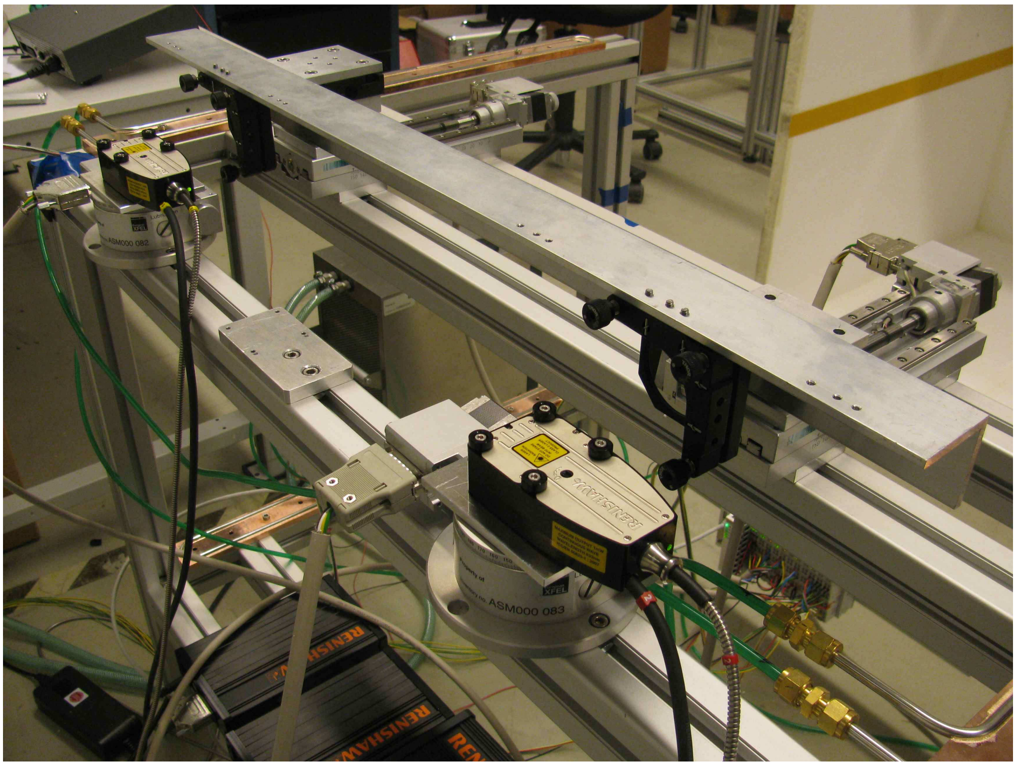

*Figure 27*: *Test setup for interferometric measurements*

In Figure 28, a rotation of the two laser heads was performed without moving the mirror. The observed negative length change is related to the measurement principle, since the distance should increase as the head is rotated out of the perpendicular position. However, these measurements show that the angular accuracy of the goniometer is not critical: the slopes of the observed parabolas are about 1 nm/(0.01°)$^2$, meaning that a precision of 0.01° is sufficient for the rotation stages to obtain 1 nm accuracy, corresponding to < 2 nrad angular accuracy. The deviations from the parabolas (lower panel of Figure 28) are in the range of ± 50 nm. This is probably largely due to temperature fluctuation during the measurements and no backlash compensation of the motor controller (jump around zero position). The eccentricity of the goniometers should contribute as well; however, at this moment, one can only conclude that this contribution is equal to or less than the ± 50 nrad measured over the observed angular range.

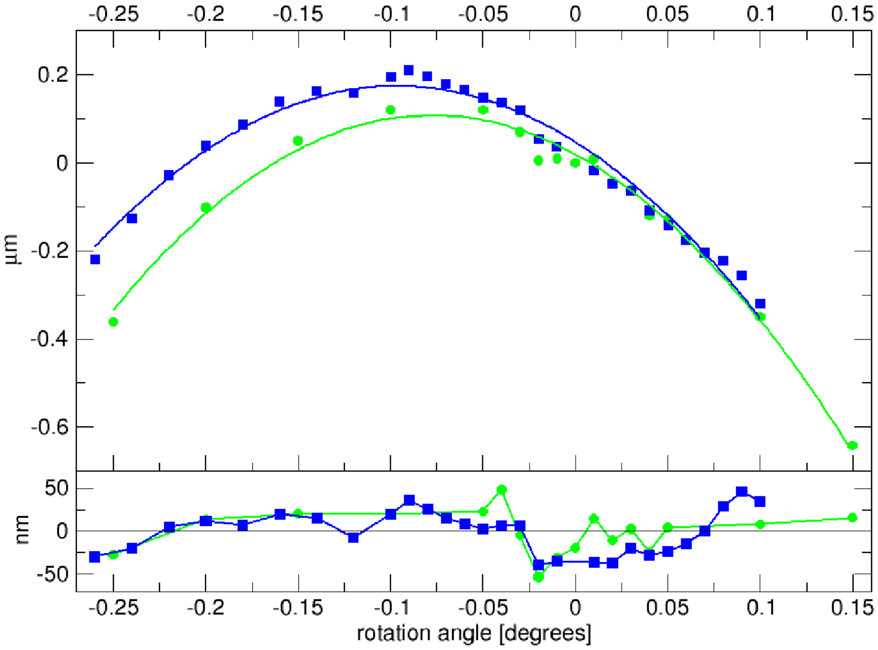

***Figure 28***: *Rotation of the two interferometer heads with mirror fixed. The y-axis shows the displayed distance change of the interferometer. The solid lines are fitted parabolas. Residual errors are shown in the lower panel.*

To perform long-term measurements of the stability, the setup was enclosed with a styrofoam cover and the aluminium frame was temperature-stabilized with a water bath. The result of a seven-day measurement period is shown in Figure 29. While the room temperature has a daily variation of about ± 0.2 K, inside the enclosure the variation is reduced to less than ± 0.1 K. The linear drift measured by one interferometer head is ± 0.5 µm, while the difference between the two sensors drifts by about ± 25 nm over this time.

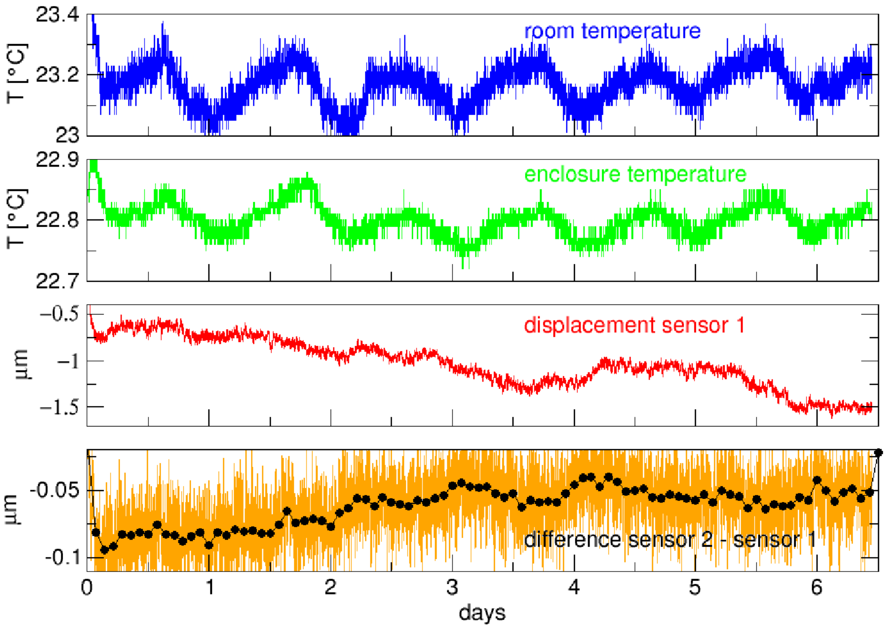

***Figure 29***: *Stability of interferometer in the test setup*

The observed 50 nm drift in the differential signal is much more than the vendor specification of 50 nm/°C from the laser unit and 100 nm/°C for the interferometer heads. Therefore, it is likely that the observed drifts in position and differential signal are caused by relaxation motions of the aluminium frames or the interferometer mounts.

In conclusion, the observed precision levels of the test setup in the range of 50 nm would lead to an accuracy of the angle determination of about 60 nrad for an 800 mm long mirror. With a granite support as well as better temperature control and motion control, this number is likely to improve. However, already with a stability level of 60 nrad, the above-mentioned chamber deformations of 0.6 µrad should be easily detectable.

# 4 Soft X-ray monochromator

Compared to CDR2011, the design of the soft X-ray monochromator was fundamentally revised and optimized. The time broadening was improved, so that now an almost Fourier-limited time response of around 100 fs pulse width can be obtained. This was achieved by designing the monochromator close to the diffraction limit, assuming nearly perfect optics, similar to the offset and distribution mirrors. If the optics do not meet the specification or if the source point in the undulator is broadened beyond the diffraction limit, the monochromator will work with less resolution but unchanged time response.

Another change is the implementation of an in-line design in the vertical plane. In this way, all three SASE3 ports can use the monochromatized beam or—with the pre-mirrors retracted—the non-monochromatized beam (pink beam). In the vertical geometry, the monochromator is independent of the focusing properties and heat load effects of the offset mirrors, which would otherwise influence the resolution. The drawback of the in-line design is that resolutions higher than 40 000 cannot be reached anymore with satisfying efficiency.

Finally, the pre-focusing onto the grating was removed, which enhances the radiation tolerance and will allow the operation of the monochromator with 10 mJ pulse energies and higher, depending on the FEL beam divergences obtained. The grating incidence angle is optimized such that a 4σ beam footprint on the grating is achieved at a certain target energy. For lower energies, the grating is overfilled and diffraction effects influence the resolution. According to wavefront calculations, the resolution still remains acceptable, even though it leads to small side maxima at the very low end of the photon energy range.

# Conceptual design

The updated conceptual design of the SASE3 beamline is shown in Figure 30.

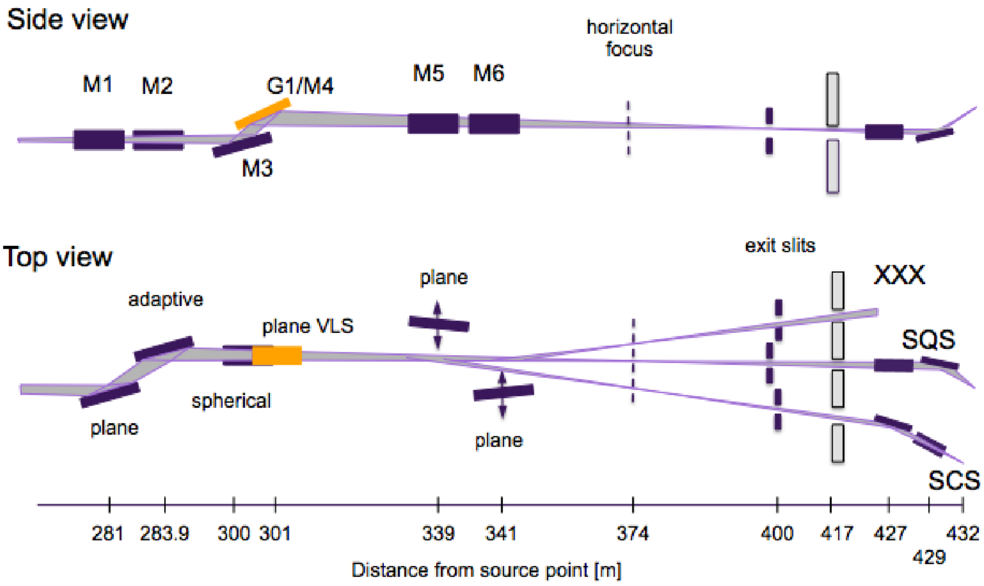

***Figure 30***: *Schematic layout of the SASE3 beamline including the VLS monochromator*

Distances from the source point are given in Table 2.

***Table 2:*** *Positions of optical elements at the SASE3 beamline*

| **Optics element** | **Metres from source** |
|---|---:|
| M1: First offset mirror, 6–20 mrad | 281 |
| M2: Second offset mirror, 6–20 mrad (bendable) | 283.9 |
| FEL beam stop | 297 |
| M3: Focusing mirrors | 299.6/300.4 |
| G1, G2 (M4): Gratings | 301 |
| M5: SCS distribution mirror, 9 mrad | 339 |
| M6: SQS2 distribution mirror, 9 mrad | 341 |
| Horizontal focus (branch beamlines, low energy) | 374 |
| Vertical exit slits (vertical focus) | 400 |
| Shutters | 417 |
| Wall inside XHEP | 418.5 |
| Sample SCS/SQS | 432/450 |

The pre-mirror M3 focuses the zero order of the grating onto the exit slit. The distance between M3 and the exit slits was chosen relatively large (100 m) because this reduces the demagnification of the source point at the exit slit. Otherwise, a too small focus would lead to single-shot damage. For the same reason, the vertical focus has to be at some distance from the horizontal intermediate focus, which is needed to transport the beam over the distribution mirror to the branch beamlines.

The VLS parameter of the plane grating is chosen such that it focuses also the first diffraction order onto the exit slit. In this way, the VLS parameter becomes almost independent of the photon energy, and tunability over a large energy range becomes possible. The tuning of the energy is achieved by rotating the grating only.

### Time and energy resolution

The stretching of pulses through a grating can be described by [14]:

$$\Delta\tau = \frac{1}{c}\frac{\lambda^2}{\Delta\lambda}$$

The relative energy resolution is given by the number of illuminated lines on the FWHM of the grating (see Figure 31):

$$\frac{\lambda}{\delta\lambda} = \frac{\delta x_{\text{fwhm}}}{d_0\ \sin\alpha} = \frac{500\ \text{mm}\frac{2.354}{4}}{d_0} = 294.3\ \text{mm}\ \times \frac{\text{lines}}{\text{mm}}$$

$$\Delta\tau = \frac{1.234\ \text{nm} * 294.3\ \text{mm} * \text{lines/mm}}{E[\text{keV}] *\ 3e8\ \text{m/s}} = \frac{1.21\ \text{fs} * \text{lines/mm}}{E[\text{keV}]}$$

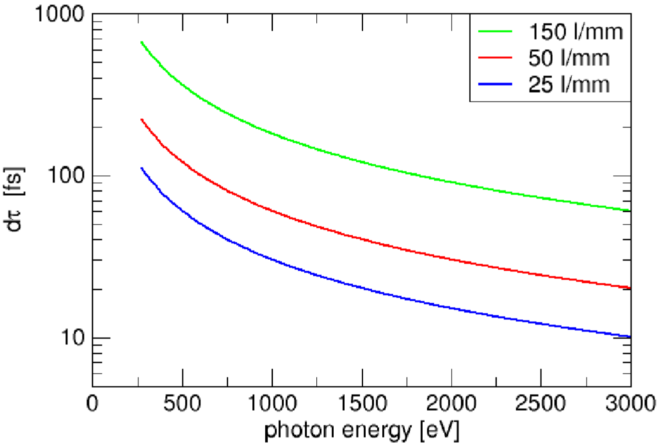

***Figure 31:*** *Pulse stretching for a 4σ illuminated grating of 500 mm length*

To achieve < 100 fs pulse length at around 1 keV, 50 l/mm are necessary, if the full 500 mm long grating is illuminated. With 25 l/mm, ultrafast experiments with 30 fs would be possible. For higher energies, 150 l/mm lead to about 100 fs pulse length. If the full grating is illuminated at every photon energy, the relative resolution is constant and shown in Table 3.

***Table 3:*** Theoretical grating resolution, if the grating is illuminated by $4\sigma$

| | **25 l/mm** | **50 l/mm** | **100 l/mm** | **150 l/mm** |
|---|---|---|---|---|
| $\lambda/\delta\lambda$ | 7300 | 14 700 | 29 400 | 44 100 |

From this condition of constant (diffraction-limited) illumination of the grating of a certain length follows the grazing-incidence angle $\alpha$, from the grating equation the grazing exit angle $\beta$. The angle $\theta$ then follows from the condition of constant exit angle (see Table 4 and Table 5). A monochromator designed like this satisfies the condition of maximum pulse energy tolerance for FEL beams because the beam footprint is always ideally distributed over the grating.

***Table 4:*** *Angle setting for an optimum $4\sigma$ illumination of a 500 mm grating. Beam points 0.194 mrad down (25 mm vertical offset). 50 l/mm.*

| **Photon energy [keV]** | **Beam size $4\sigma$ at 301 m [mm]** | **$\alpha$ ($L_1$ = 500 mm) [mrad]** | **$\beta$ (50 l/mm) [mrad]** | **cff** | **$\theta$ M3 [mrad]** | **$R$ M3 [km]** | **$4\sigma$ length M3 [mm]** |
|---|---|---|---|---|---|---|---|
| 0.27 | 19.25 | 38.51 | 44.05 | 1.14 | 41.18 | 3.64 | 467 |
| 0.5 | 12.12 | 24.25 | 28.90 | 1.19 | 26.48 | 5.67 | 458 |
| 0.8 | 8.52 | 17.05 | 21.09 | 1.23 | 18.97 | 7.91 | 449 |
| 1.0 | 7.21 | 14.42 | 18.20 | 1.26 | 16.21 | 9.25 | 445 |
| 1.5 | 5.32 | 10.64 | 13.98 | 1.31 | 12.21 | 12.3 | 435 |
| 1.7 | 4.84 | 9.688 | 12.90 | 1.33 | 11.20 | 13.4 | 433 |
| 2.0 | 4.28 | 8.576 | 11.62 | 1.35 | 10.01 | 15.0 | 429 |
| 2.5 | 3.62 | 7.254 | 10.09 | 1.39 | 8.580 | 17.5 | 423 |
| 3.0 | 3.16 | 6.327 | 9.009 | 1.42 | 7.757 | 19.8 | 418 |

One difficulty of this design is that the angle of the pre-mirror has to be scanned together with the grating: its position and its bending radius as well. Due to the high demands on the surface quality of the mirrors (around 50 nrad rms), a bendable mirror of sufficient quality seems at this time not feasible. Therefore, the monochromator is designed around two working points with fixed-radius pre-mirrors.

***Table 5:*** *Angle setting for an optimum 4σ illumination of a 500 mm grating. Beam points 0.194 mrad down (25 mm vertical offset). 150 l/mm.*

| **Photon energy [keV]** | **Beam size 4σ at 301 m [mm]** | **$\alpha$ ($L_1$ = 500 mm) [mrad]** | **$\beta$ (150 l/mm) [mrad]** | **cff** | **$\theta$ M3 [mrad]** | **$R$ M3 [km]** | **4σ length M3 [mm]** |
|---|---|---|---|---|---|---|---|
| 0.27 | 19.25 | 38.51 | 53.34 | 1.38 | 45.87 | 3.27 | 419 |
| 0.5 | 12.12 | 24.25 | 36.45 | 1.50 | 30.26 | 4.96 | 400 |
| 0.8 | 8.52 | 17.05 | 27.45 | 1.61 | 22.15 | 6.77 | 384 |
| 1.0 | 7.21 | 14.42 | 24.04 | 1.66 | 19.13 | 7.84 | 376 |
| 1.5 | 5.32 | 10.64 | 18.97 | 1.78 | 14.71 | 10.2 | 361 |
| 1.7 | 4.84 | 9.688 | 17.65 | 1.82 | 13.57 | 11.0 | 356 |
| 2.0 | 4.28 | 8.576 | 16.08 | 1.87 | 12.23 | 12.2 | 350 |
| 2.5 | 3.62 | 7.254 | 14.16 | 1.95 | 10.61 | 14.1 | 341 |
| 3.0 | 3.16 | 6.327 | 12.78 | 2.02 | 9.45 | 15.8 | 334 |

## Fixed-radius pre-mirrors

The monochromator is optimized around two working points: the low-energy (LE) point around 742 eV and a high-energy (HE) point around 2.3 keV (Table 6). At these photon energies, the grating is filled with a 4σ beam as discussed above.

***Table 6:*** *Parameters for the two target energies, 50 l/mm*

| **Target photon energy [keV]** | **Photon energy range [keV]** | **$\theta$ M3 [mrad]** | **$\alpha_{target}$ [mrad]** | **$\beta_{target}$ (50 l/mm) [mrad]** | **Dist. M3–G1 [mm]** | **$R$ M3 [km]** |
|---|---|---|---|---|---|---|
| 0.7426 | 0.27–1.2 | 20.0 | 18.0313 | 22.166 | 625 | 7.5 |
| 2.332 | 1.2–3.0 | 9.00 | 7.6432 | 10.552 | 1389 | 16.7 |

The angle and radius of the two pre-mirrors M3 are now fixed, and $\alpha$ and $\beta$ follow from the grating equation (Table 7 to Table 10).

***Table 7:*** *Parameters for the target energy 0.74 keV, 500 mm grating, 50 l/mm*

| **Photon energy [keV]** | **Grating aperture in sigma** | **$\theta$ M3b [mrad]** | **$\alpha$ ($L_1$ = 500 mm) [mrad]** | **$\beta$ (50 l/mm) [mrad]** | **cff** |
|---|---|---|---|---|---|
| 0.27 | 1.50 | 20.00 | 14.411 | 25.783 | 1.79 |
| 0.4 | 2.26 | 20.00 | 16.259 | 23.935 | 1.47 |
| 0.5 | 2.81 | 20.00 | 17.026 | 23.167 | 1.36 |
| 0.6 | 3.31 | 20.00 | 17.538 | 22.656 | 1.29 |
| 0.7 | 3.80 | 20.00 | 17.904 | 22.290 | 1.25 |
| 0.8 | 4.26 | 20.00 | 18.178 | 22.016 | 1.21 |
| 1.0 | 5.14 | 20.00 | 18.562 | 21.632 | 1.16 |
| 1.2 | 5.98 | 20.00 | 18.818 | 21.376 | 1.14 |
| 1.4 | 6.78 | 20.00 | 19.000 | 21.193 | 1.11 |
| 1.5 | 7.17 | 20.00 | 19.073 | 21.120 | 1.10 |

***Table 8:*** *Parameters for the target energy 2.33 keV, 500 mm grating, 50 l/mm*

| **Photon energy [keV]** | **Grating aperture in sigma** | **$\theta$ M3a [mrad]** | **$\alpha$ ($L_1$ = 500 mm) [mrad]** | **$\beta$ (50 l/mm) [mrad]** | **cff** |
|---|---|---|---|---|---|
| 1.0 | 1.58 | 9.00 | 5.7055 | 12.488 | 2.18 |
| 1.2 | 1.99 | 9.00 | 6.2708 | 11.923 | 1.90 |
| 1.4 | 2.38 | 9.00 | 6.6745 | 11.519 | 1.72 |
| 1.6 | 2.75 | 9.00 | 6.9773 | 11.216 | 1.60 |
| 1.8 | 3.10 | 9.00 | 7.2128 | 10.981 | 1.52 |
| 2.0 | 3.45 | 9.00 | 7.4012 | 10.793 | 1.45 |
| 2.3 | 3.94 | 9.00 | 7.6224 | 10.571 | 1.38 |
| 2.6 | 4.42 | 9.00 | 7.7925 | 10.401 | 1.33 |
| 3.0 | 5.03 | 9.00 | 7.9664 | 10.227 | 1.28 |

***Table 9:*** *Parameters for $\theta$ = 20 mrad, 500 mm grating, 150 l/mm*

| **Photon energy [keV]** | **Grating aperture in sigma** | **$\theta$ M3b [mrad]** | **$\alpha$ ($L_1$ = 500 mm) [mrad]** | **$\beta$ (150 l/mm) [mrad]** | **cff** |
|---|---|---|---|---|---|
| 0.27 | 0.31 | 20.00 | 3.0386 | 37.155 | 12.2 |
| 0.4 | 1.20 | 20.00 | 8.5828 | 31.611 | 3.68 |
| 0.5 | 1.80 | 20.00 | 10.885 | 29.308 | 2.69 |
| 0.6 | 2.35 | 20.00 | 12.421 | 27.777 | 2.23 |
| 0.7 | 2.87 | 20.00 | 13.517 | 26.676 | 1.97 |
| 0.8 | 3.36 | 20.00 | 14.340 | 25.854 | 1.80 |
| 1.0 | 4.30 | 20.00 | 15.491 | 24.702 | 1.59 |
| 1.2 | 5.17 | 20.00 | 16.259 | 23.935 | 1.47 |
| 1.4 | 6.00 | 20.00 | 16.807 | 23.387 | 1.39 |
| 1.5 | 6.40 | 20.00 | 17.026 | 23.167 | 1.36 |

***Table 10:*** *Parameters for $\theta$ = 9 mrad, 500 mm grating, 150 l/mm*

| **Photon energy [keV]** | **Grating aperture in sigma** | **$\theta$ M3a [mrad]** | **$\alpha$ ($L_1$ = 500 mm) [mrad]** | **$\beta$ (150 l/mm) [mrad]** | **cff** |
|---|---|---|---|---|---|
| 1.4 | 0.65 | 9.00 | 1.8297 | 16.364 | 8.94 |
| 1.6 | 1.08 | 9.00 | 2.7381 | 15.456 | 5.64 |
| 1.8 | 1.48 | 9.00 | 3.4446 | 14.749 | 4.28 |
| 2.0 | 1.87 | 9.00 | 4.0099 | 14.184 | 3.53 |
| 2.3 | 2.42 | 9.00 | 4.6734 | 13.520 | 2.89 |
| 2.6 | 2.94 | 9.00 | 5.1838 | 13.010 | 2.50 |
| 3.0 | 3.60 | 9.00 | 5.7055 | 12.488 | 2.18 |

The spectral efficiency and the resolution, including an approximation for diffraction effects, were approximated for a laminar grating [15] (see Figure 32 and Figure 33). Calculations done by ray tracing are shown in Figure 34. By using a blazed grating, the efficiency can be increased by almost a factor of two.

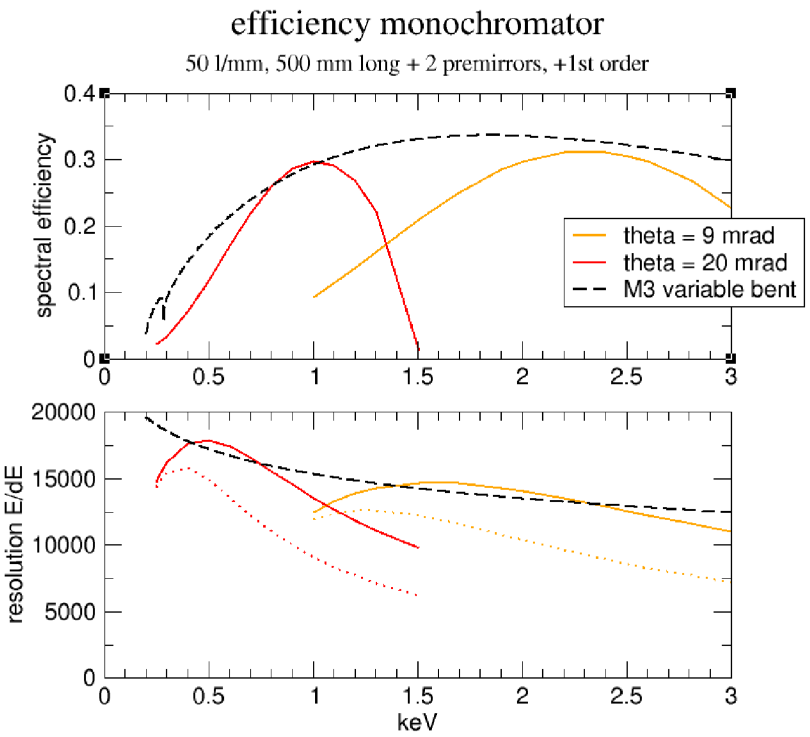

***Figure 32:*** Top: *Spectral efficiency according to scalar approximation.* Bottom: *Estimation of resolution (source size is assumed to be 60 μm (dotted line:100 μm) FWHM). The grating depth is 15 nm.*

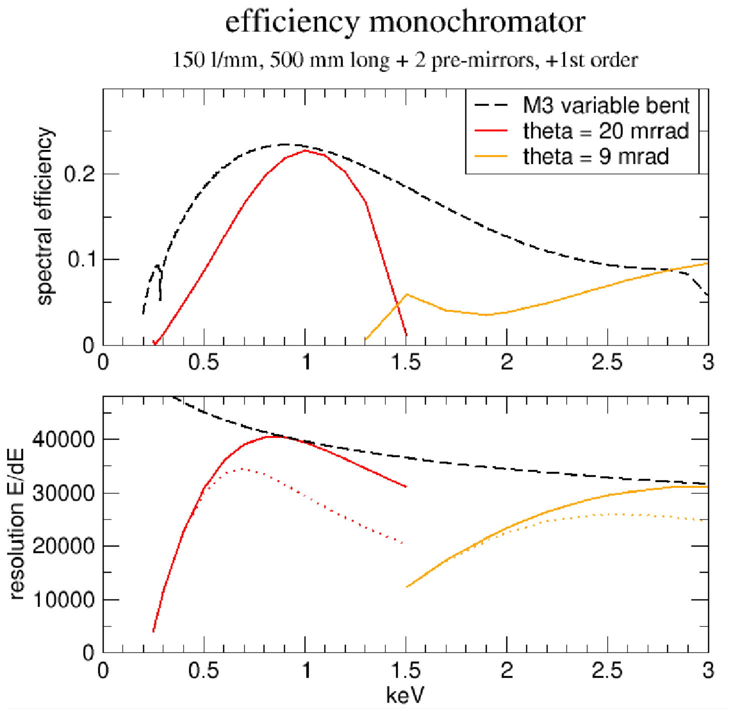

***Figure 33:*** *As Figure 32 with 150 l/mm*

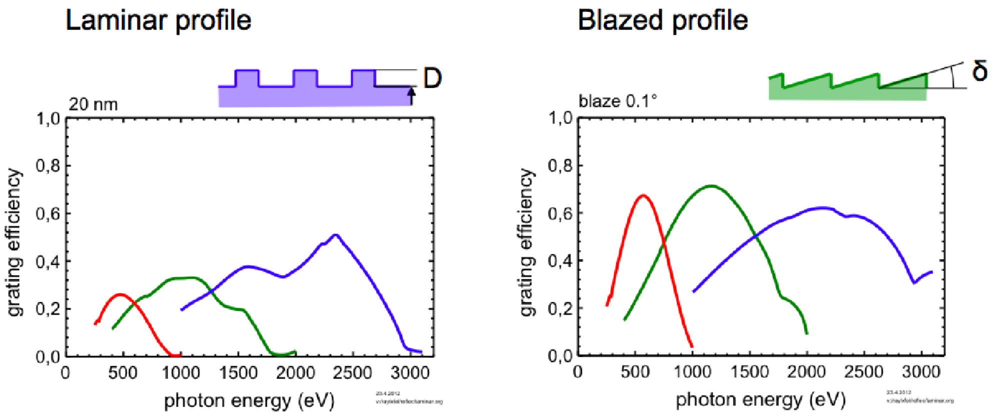

***Figure 34***: *Grating efficiency for laminar and blazed grating in comparison. The calculation was done here for three pre-mirrors (by Rolf Follath, HZB).*

## VLS parameter

The VLS grating parameter $v_1$ in

$$d(w) = d_0(1 + v_1 w + v_2 w^2 + \ldots)$$

for a plane grating is [15]:

$$v_1 = \frac{d}{n\lambda}\left(\frac{\sin^2\alpha}{f} - \frac{\sin^2\beta}{g}\right)$$

with *d* being the grating pitch and $v_1$ the linear ruling parameter.

In the actual grating setting, the beam is converging; therefore, the source at distance *f* becomes virtual on the other side. The idea of an energy-independent focus can be realized if *f* = *g*:

$$v_1 = \frac{d}{n\lambda}\left(\frac{\sin^2\alpha}{g} - \frac{\sin^2\beta}{g}\right)$$

$$v_1 = \frac{2d}{n\lambda g}(\cos\alpha - \cos\beta), \qquad \left(\text{with } (1 - \frac{1}{2}\sin^2 x) \sim \cos x\right)$$

By using the grating equation

$$\frac{n\lambda}{d} = \cos\alpha - \cos\beta$$

one obtains

$$\nu_1 \approx \frac{2}{g} = \frac{2}{99\ \mathrm{m}} = 0.02020\ \mathrm{m}^{-1}$$

for a grating-to-exit-slit distance of 99 m.

Due to the large distance of the exit slit, the error of the above approximation with only one linear VLS parameter is small and can be expressed as

$$\left(\frac{d(w)}{d_0} - 1\right) - \nu_1 w = \nu_2 w^2 + \cdots$$

as shown in Figure 35. Here, *d*(*w*) is calculated locally on the grating with the grating equation and the corresponding angles *α*(*w*) and *β*(*w*). The deviations are small and almost energy-independent, except for the lowest energy of 270 eV. For energies > 500 eV, the deviations can be approximated by $\nu_2 \approx 0.6 \cdot 10^{-5}/(0.25\ \mathrm{m})^2 = 1 \cdot 10^{-4}\ \mathrm{m}^{-2}$. However, one should consider that the change of ruling pitch according to $\nu_2$ at the edge of the grating is only about 0.1 nm, and therefore the linear term $\nu_1$ might be sufficient.

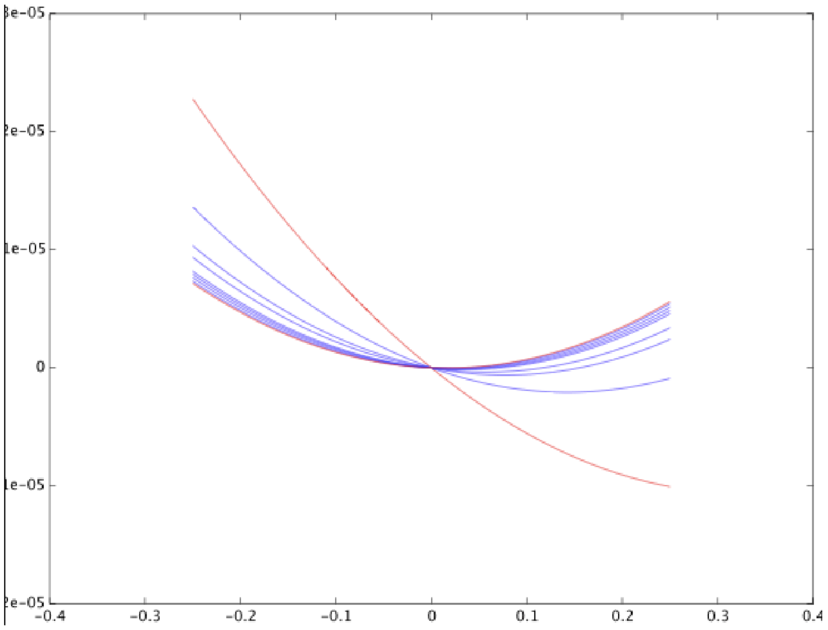

***Figure 35**: Deviations of the VLS parameter from the linear approximation along the grating (x-axis in m). The different curves are calculated for different energies from 0.27 keV (red curve with strong linear term) to 3 keV (other red curve) and intermediate energies (blue curves) as used in Table 4.*

## Optical layout

The monochromator is designed to cover the energy range from 270 to 3000 eV, and it also allows operation with the non-monochromatized beam (pink beam). As an alternative, remote-controlled manipulators allow the two cylindrically shaped pre-mirrors to be inserted face up into the beam. Each pre-mirror has been optimized for a specific energy range, and both mirrors focus the beam vertically on the exit slit. The pre-mirror deflects the beam upwards on the plane VLS grating. Two gratings with different line density are comprised in the design in order to reach the required resolution on the whole energy range. In an empty third slot, a blank mirror (without ruling) can be mounted together with the gratings for calibration purposes, and it could also reflect the vertically focused pink beam. Both pre-mirror and grating have to be properly cooled to ensure achievement of the final performance.

Figure 36 shows an overview of the monochromator optical layout. The vertical dimension has been magnified by a factor 10 for clarity.

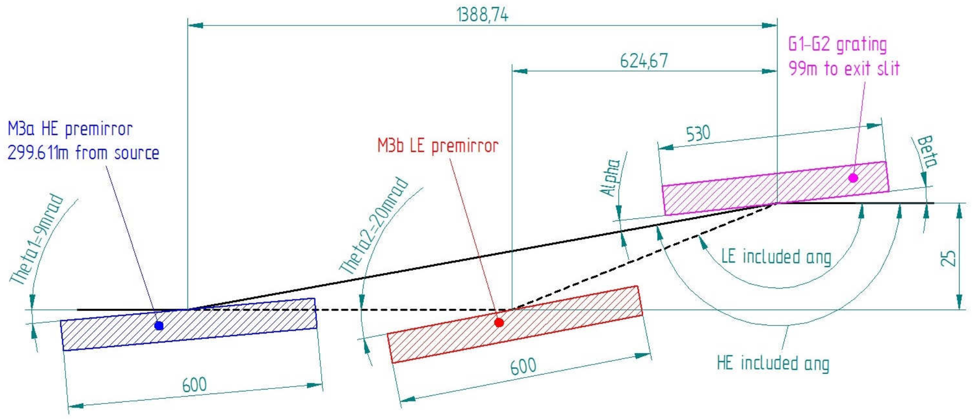

***Figure 36****: Side view of the monochromator optical layout. The beam is propagating from left to right. Vertical dimension has been magnified by a factor 10. Indicated mirror length refers to the substrate length.*

# Optics requirements

## High-energy (HE) and low-energy (LE) pre-mirrors

The HE (LE) pre-mirror works at a fixed incidence angle of 9 mrad (20 mrad) and deflects the beam upwards onto the gratings. It focuses the beam vertically on the exit slit. $B_4C$ masks protect the substrate edges and other mechanical features from the photon beam. Table 11 summarizes the main mechanical and optical characteristics of the two pre-mirrors.

***Table 11:*** *HE and LE pre-mirror main parameters*

| | **M3a HE pre-mirror** | **M3b LE pre-mirror** |
|---|---|---|
| Substrate material | Single-crystalline Si | Single-crystalline Si |
| Substrate size (L x W x H) | 600 x 100 x 70 $mm^3$ | 600 x 100 x 70 $mm^3$ |
| Optical surface (mer x sag) | 580 x 25 $mm^2$ | 580 x 30 $mm^2$ |
| Surface coating | $B_4C$ | $B_4C$ |
| Figure | Cylindrical | Cylindrical |
| Orientation | Facing up | Facing up |
| Nominal incidence angle | 9 mrad | 20 mrad |
| Object distance | 299 611 mm | 30 0375 mm |
| Image distance | 100 389 mm | 99 625 mm |
| Radius of curvature | 16 710m ± 100 m | 7482 m ± 50m |
| RMS slope error (meridional) | 50 nrad | 50 nrad |
| Residual PV height error | 3 nm | 3 nm |
| RMS HSFRoughness* | 0.2 nm | 0.2 nm |
| RMS MSFRoughness* | 0.2 nm | 0.2 nm |
| Cooling system | InGa eutectic bath | InGa eutectic bath |
| *High and Middle Spatial Frequency Roughness are defined as follows: MSFR from $10^{-6}$ $nm^{-1}$ to $5 \cdot 10^{-4}$ $nm^{-1}$ and HSFR from $5 \cdot 10^{-4}$ $nm^{-1}$ to $5 \cdot 10^{-2}$ $nm^{-1}$ [16] | | |

Figure 37 shows the HE and LE mirror and the internally Ni-coated copper pool that contains the eutectic bath. The cooling system is discussed later in this section.

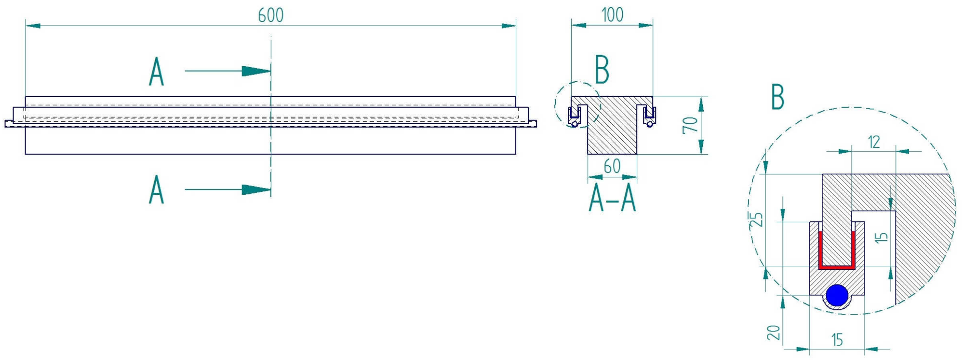

***Figure 37**:* Red: *HE and LE pre-mirror, eutectic bath.* Blue: *Water-cooled copper pool.*

## Low-resolution grating (G1) and high-resolution grating (G2)

Gratings are the dispersive optics in the VLS-PGM design. The groove density is varying (VLS gratings) along the grating surface in the beam propagation direction (*y* direction) according to the equation $d(y) = d_0(1 + v_1 y + v_2 y^2 + \ldots)$, where $d_0$ is the groove pitch (mm/lines) at the centre of the optical surface ($y = 0$) and the *y*-axis is oriented in the beam propagation direction. $B_4C$ masks protect the substrate edges and other mechanical features from the photon beam.

Table 12 summarizes the main mechanical and optical characteristics of the two gratings. Figure 38 and Figure 39 show the assembly of G1 and the cooling system at the maximum $\beta$ angle (37.2 mrad = 2.131°). The mirror is facing down and the cooling groves along the mirror are segmented in order to limit the eutectic flowing effect from one extremity to the other during grating rotation. Additional cooling system considerations are discussed below. Grating G2 follows the same mechanical design concept.

***Table 12:*** *G1 and G2 grating main mechanical, optical and operational parameters*

| | **G1 normal resolution** | **G2 high resolution** |
|---|---|---|
| Substrate material | Single-crystalline Si | Single-crystalline Si |
| Substrate size (L x W x H) | 530 x 100 x 70 $mm^3$ | 530 x 100 x 70 $mm^3$ |
| Optical surface (mer x sag) | 500 x 30 $mm^2$ | 500 x 30 $mm^2$ |
| Surface coating | $B_4C$ | $B_4C$ |
| Figure | Plane | Plane |
| Orientation | Facing down | Facing down |
| Included angle for M3a (HE) | 178.96° | 178.96° |
| Included angle for M3b (LE) | 177.7° | 177.7° |
| Max / min $\beta$ (see Figure 47) | 25.8 mrad at 0.27 keV<br>10.2 mrad at 3 keV | 37.2 mrad at 0.27 keV<br>12.5 mrad at 3 keV |
| Groove parameter $1/d_0$ | 50 l/mm | 150 l/mm |
| Groove parameter $v_1$ | 0.020202 $m^{-1}$ | 0.020202 $m^{-1}$ |
| Groove profile | Blazed | Blazed |
| Blaze angle | 0.1° | 0.1° |
| RMS slope error (meridional) | 50 nrad | 50 nrad |
| Residual PV height error | 3 nm | 3 nm |
| RMS HSFRoughness * | 0.2 nm | 0.2 nm |
| RMS MSFRoughness * | 0.2 nm | 0.2 nm |
| Cooling system | InGa eutectic bath | InGa eutectic bath |
| *High and Middle Spatial Frequency Roughness are defined as follows: MSFR from $10^{-6}$ $nm^{-1}$ to $5 \cdot 10^{-4}$ $nm^{-1}$ and HSFR from $5 \cdot 10^{-4}$ $nm^{-1}$ to $5 \cdot 10^{-2}$ $nm^{-1}$ [16] | | |

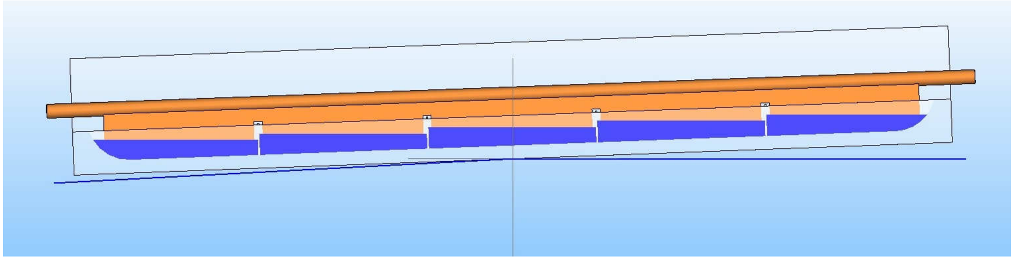

***Figure 38**: Grating, eutectic bath, and copper blade at max β angle (2.131°)*

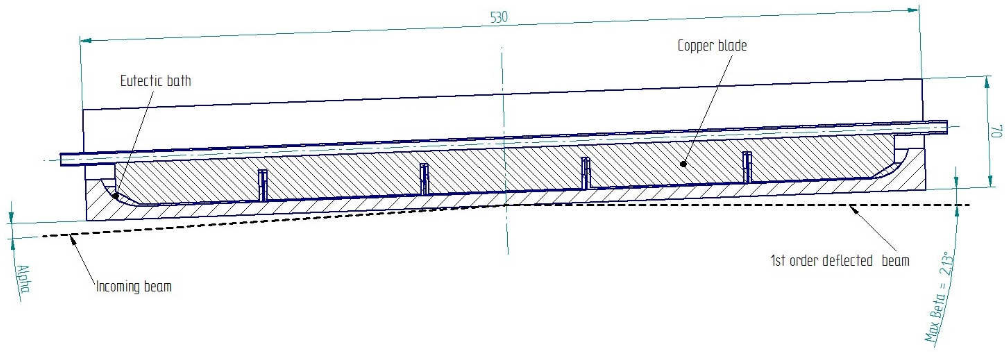

***Figure 39**: Cross section of the grating that is positioned at the centre of the copper blade*

The gratings are vertically supported on four points. The supporting points act on the mirror-reflecting surface, they are longitudinally located in the Bessel point position, and they are transversally far enough from the clear aperture to avoid sensible sagittal deformation of the latter. Additional longitudinal and transversal locking points fix the remaining degree of freedom of the mirror. To avoid deformations during the grating rotation, the longitudinal locking point has to be located on the vertical neutral axis of the mirror. Figure 40 shows the location of the supports.

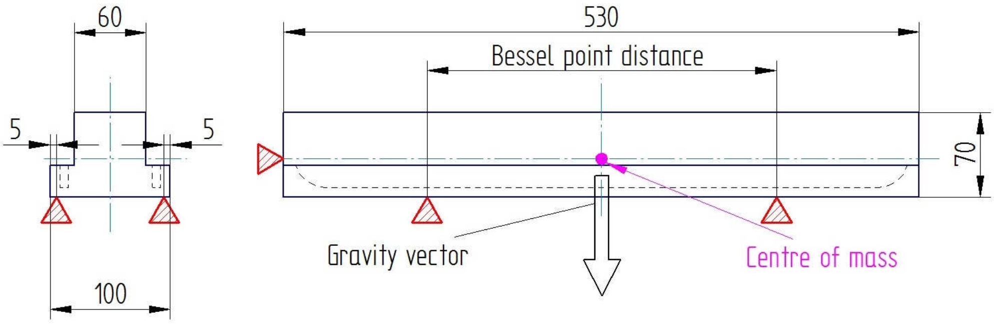

***Figure 40**: Grating vertical and longitudinal support location*

FEA calculations have been carried out to evaluate the effect of the four vertical supporting points on the mirror's optical surface. Longitudinal (meridional) and sagittal deformations are shown in the following pictures.

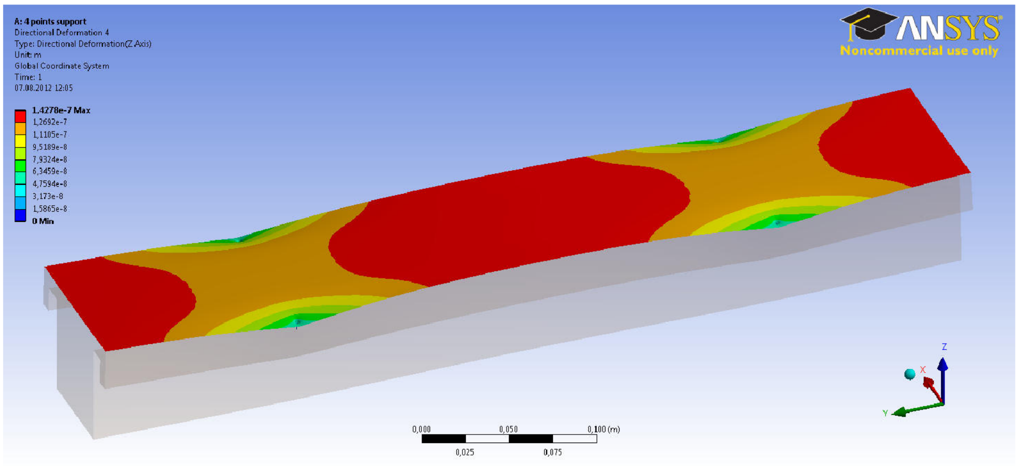

***Figure 41***: *Vertical deformation [m] of the optical surface due to mirror mass under gravitational force*

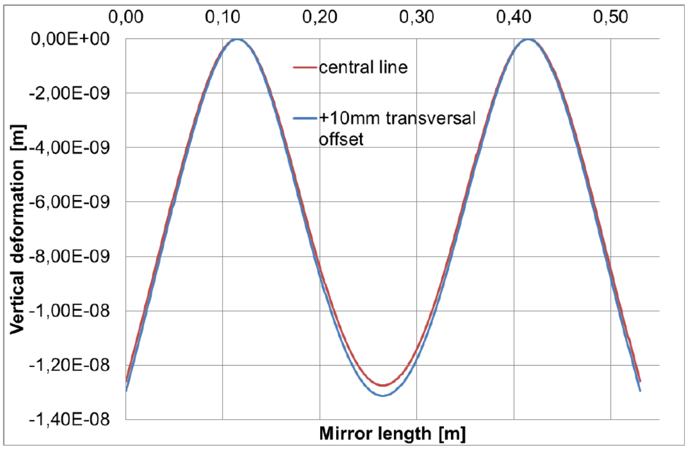

***Figure 42***: *Vertical deformation [m] along the mirror.* Red: *For the central line.* Blue: *For a line that is parallel to the central line and 10 mm transversally offset.*

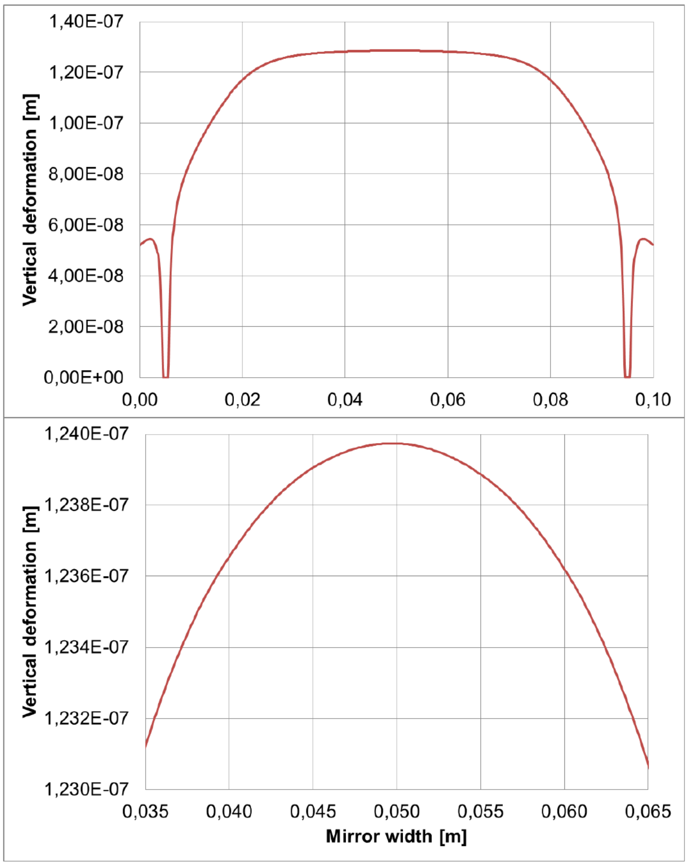

***Figure 43**: Top: Vertical deformation [m] across the mirror for the line that connects two supporting points.* Bottom: *A zoom of the top graph highlights the 1 nm sagittal clear aperture deformation.*

## Mirror cooling system

To reduce as much as possible the effect of the thermal bump that affects the mirror figure, a high-efficiency cooling system has to be implemented. Different cooling schemes have been taken into account, among them:

- Eutectic bath in contact with the mirror and water-cooled Ni-coated copper bars
- Side cooling with copper pads pressed on the silicon mirror

The present design implements mirrors that are cooled with an eutectic bath because the eutectic bath:

- Is highly efficient in terms of achievable film coefficient ($h$ > 50 000 W/m$^2$K)
- Guarantees constant film coefficient along the wet surface

- Allows fast thermal transient phase
- Does not introduce deformation on the mirror substrate
- Does not transfer to the substrate all the vibration produced by the water primary cooling system

The eutectic bath presents evident strengths, but at the same time we are well aware of the weaknesses of this choice:

- The rotation of the gratings causes a variation of the liquid height that could modify the system's thermal properties
- It could be considered as a limit for the vacuum performance: limited maximum baking temperature, possible air bubbles snared between the eutectic bath and the mirror wall
- Long and complicated wetting procedure

Table 13 reports integrated thermal power, integrated peak power density, pulse train thermal power, and pulse train power density in the case of 10 mJ photon pulse energy and 2700 pulses per train at 10 Hz. The above-mentioned thermal power should be considered as absorbed power and, for the power's density evaluation, the low divergence case has been taken into account (see CDR2011 pp. 25–31).

The following figures report the mechanical deformation due to the static thermal load on the HE pre-mirror at 2.5 keV. The beam shape is Gaussian, and the low-divergence case has been taken into account in the simulations. Considering the case of 10 mJ photon pulse energy, 2700 pulses per train and 10 Hz, the beam integrated thermal power is 270 W. Taking into account the mirror coating reflectivity, the thermal power absorbed by the mirror is 6.6 W. At this relative low photon energy, the penetration of the beam into the substrate could be considered negligible in the first approximation, and the thermal load could be applied as surface thermal load. The 4σ footprint is about 220 x 2 $mm^2$ and the power density is 38 $mW/mm^2$. A convection film coefficient equal to $10^4$ $W/m^2K$ has been applied on a 10 mm high strip along the mirror and close to the hot surface. According to the symmetry only one quarter of the mirror has been simulated.

***Table 13:*** *Thermal power and thermal power density absorbed by the monochromator mirrors and gratings at different energies. Photon beams with low divergence and 10 mJ pulse energy were considered.*

| | | **Integrated** | | **Per pulse train** | |
|---|---|---|---|---|---|
| | **Energy [keV]** | **Thermal power [W]** | **Peak power density [W/mm$^2$]** | **Thermal power [W]** | **Peak power density [W/mm$^2$]** |
| High-energy pre-mirror | 3 | 8.00 | 0.060 | 1333.94 | 10.02 |
| | 2 | 6.88 | 0.026 | 1147.41 | 4.32 |
| | 1.2 | 9.40 | 0.015 | 1566.86 | 2.47 |
| Low-energy pre-mirror | 1 | 28.62 | 0.074 | 4770.32 | 12.31 |
| | 0.7 | 31.41 | 0.044 | 5235.39 | 7.37 |
| | 0.4 | 41.02 | 0.022 | 6836.18 | 3.71 |
| G1 / G2 at $\alpha$ = 5 mrad | 1.6 | 4.00 | 0.006 | 666.76 | 0.95 |
| | 1.3 | 4.73 | 0.005 | 789.17 | 0.79 |
| | 1 | 5.81 | 0.004 | 969.12 | 0.62 |
| G1 / G2 at $\alpha$ = 10 mrad | 2 | 8.13 | 0.034 | 1354.28 | 5.62 |
| | 1.2 | 10.58 | 0.018 | 1763.55 | 3.07 |
| | 0.7 | 15.01 | 0.010 | 2502.00 | 1.74 |
| G1 / G2 at $\alpha$ = 15 mrad | 1.2 | 17.55 | 0.046 | 2925.41 | 7.64 |
| | 0.8 | 21.27 | 0.028 | 3544.25 | 4.65 |
| | 0.4 | 30.99 | 0.013 | 5165.96 | 2.09 |

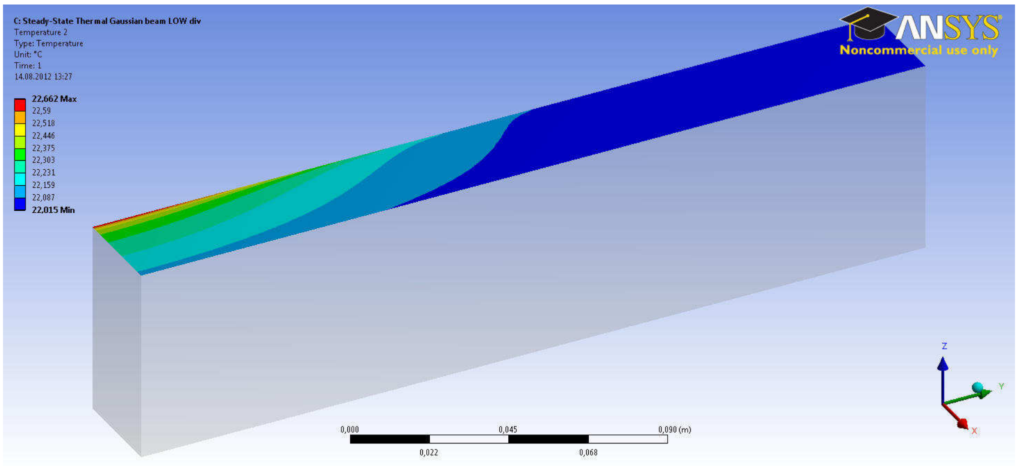

***Figure 44****: Temperature distribution on the optical surface. The temperature variation is 0.65°C.*

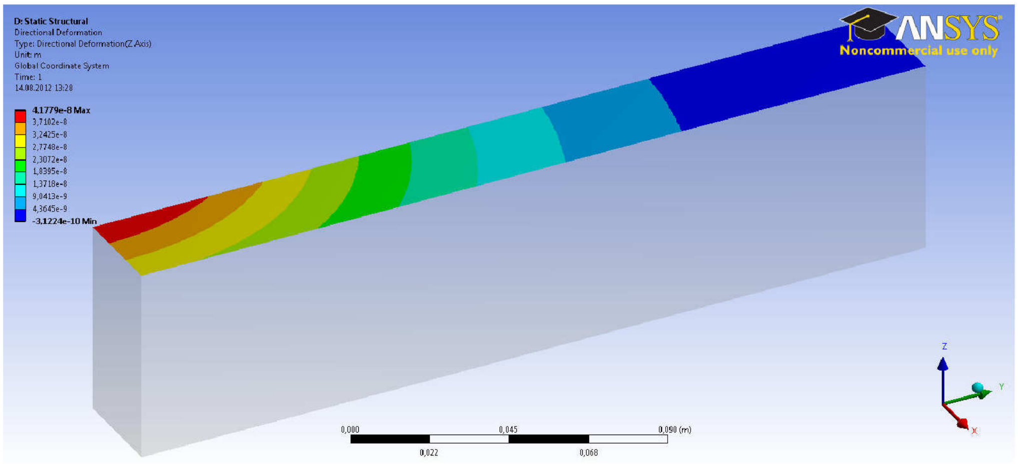

***Figure 45****: Vertical deformation [m] on the optical surface. The peak-to-valley deformation along the central meridian line is 42 nm.*

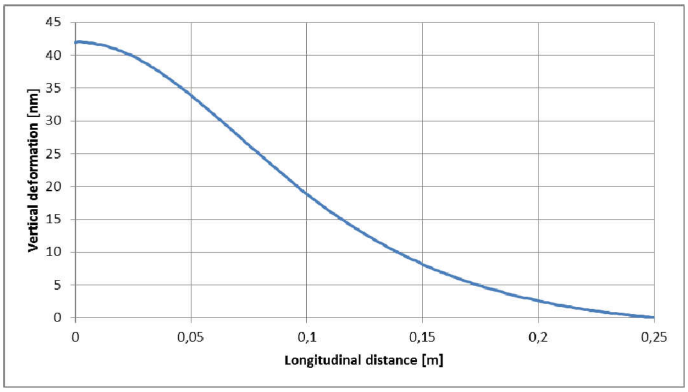

***Figure 46****: Vertical profile of the thermal bump along the mirror (in longitudinal direction) starting from the mirror centre.*

If we approximate the thermal bump as a pre-mirror tangential radius variation, we can correct the shift of the focal point position by an angle re-tuning. However, it has to be remarked that this approach takes only the static thermal effect into account; the thermal bump pulses constantly during the pulse trains, however with much smaller amplitude, and cannot be corrected. Table 14 reports the focus shift and the incidence angle variation needed to compensate for this effect in the case of the HE pre-mirror for different thermal-bump heights.

***Table 14:*** *HE pre-mirror: Focal point position shift and relative pre-mirror incidence angle correction for different PV thermal-bump heights.*

| PV thermal-bump height [nm] | Longitudinal focus shift [m] | Incidence angle variation to correct [mrad] |
|---|---|---|
| 20 | 1.005 | 0.067 |
| 50 | 2.552 | 0.166 |
| 100 | 5.236 | 0.333 |

# Technical design

Figure 47 and Figure 48 show the side and top view of the monochromator optical layout.

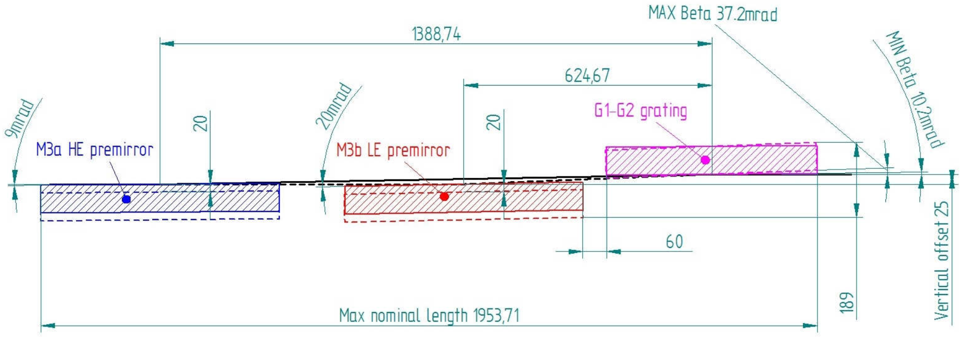

***Figure 47****: Monochromator optical design, side view*

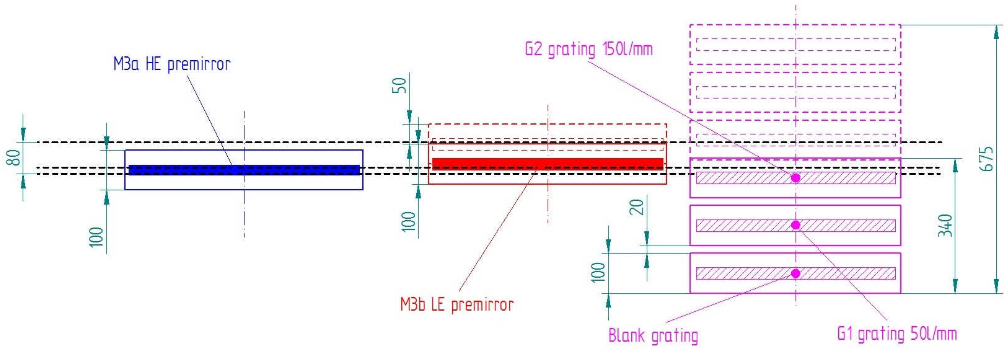

***Figure 48****: Monochromator optical design, top view*

With a vertical movement, the pre-mirrors can be inserted and extracted from the beam. This feature allows the choice of the pre-mirror that will be illuminated. When both pre-mirrors are lowered, it also makes it possible to deliver the non-monochromatic beam to the users (pink-beam operation mode). The dotted lines in Figure 47 show the position of the pre-mirrors when they are moved out of the beam.

The transversal position of the beam is not fixed; it is a function of the setting of the two upstream offset mirrors. Their incidence angle during the operation mode could be optimized to achieve the maximum reflectivity at different energies and, at the same time, to reflect the widest portion of the beam, at least 4σ. Therefore, a pre-mirror transversal motion has been implemented in order to follow the beam transversal movement. The 25 mm transversal clear aperture of the HE pre-mirror could cover the energy range from 1.2 to 3 keV without transversal motion while the 30 mm width clear aperture of the LE pre-mirror has to shift about 50 mm to cover the remaining energy range (from 1.3 to 0.270 keV). Even if the transversal motion is not strictly required in the case of the HE pre-mirror, the implementation of this feature makes it possible to use different mirror areas across the optical surface.

Two gratings with different ruling density and a blank mirror or a third grating can be mounted on a structure that can rotate to scan the energy and translate. The rotational range is 1.55° (from 10.2 to 37.2 mrad) and the mirror support transversal travel is 270 mm.

### Pre-mirror manipulator specification

During monochromator operation, the pre-mirror is kept at a fixed angle and position, but some remotely controlled adjustments have to be implemented to allow:

- Correction of the thermal effects
- Possibility to withdraw the mirrors
- Alignment of the mirror with respect to the beam transversal offset due to the setup of the upstream offset mirrors
- Beam-based alignment of the optics

With respect to Figure 49, in which coordinate axes and angles are defined, Table 15 summarizes the required range, resolution, and reproducibility of the pre-mirror degrees of freedom. Both LE and HE pre-mirror present the same movement specifications.

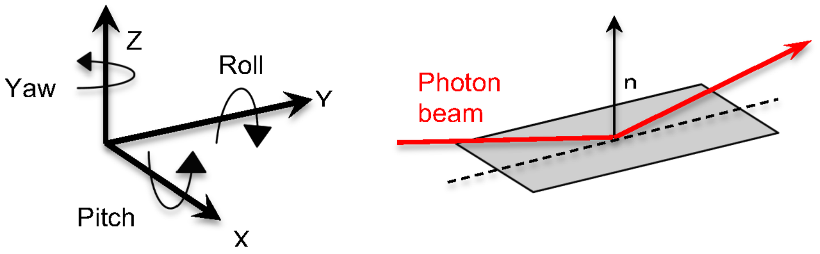

*Figure 49: Reference system for the M3a and M3b pre-mirror*

*Table 15: Mechanical specification for the pre-mirror in-vacuum manipulators*

| | Type of actuator / Use | Resolution | Reproducibility and stability | Range |
|---|---|---|---|---|
| X | Remotely controlled /<br>For operation | 1 µm | 2 µm | 50 mm |
| Y | Manual /<br>For alignment | 5 µm | 20 µm | 2 mm |
| Z | Remotely controlled /<br>For operation | 0.5 µm | 1 µm | 5 mm |
| Pitch | Remotely controlled /<br>For alignment | 0.1 µrad | 0.5 µrad | 1 mrad |
| Roll | Remotely controlled /<br>For alignment | 0.1 µrad | 0.5 µrad | 1 mrad |
| Yaw | Manual /<br>For alignment | 1 µrad | 2 µrad | 1 mrad |
| Pitch | Remotely controlled /<br>For operation | 10 nrad | 20 nrad | 0.5 mrad |

## Grating mechanics specification

With respect to Figure 50, in which coordinate axes and angles are defined, Table 16 summarizes the required range, resolution, and reproducibility of the grating degrees of freedom.

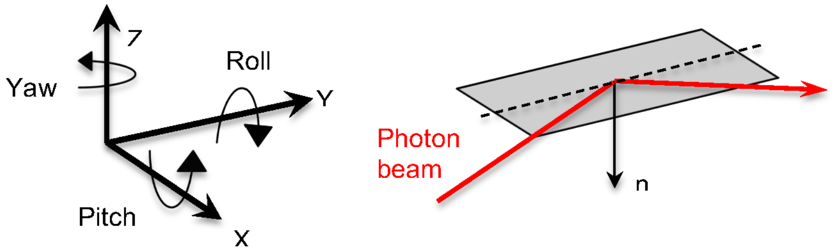

***Figure 50**: Reference system for the grating*

***Table 16:** Mechanical specification for the grating in-vacuum mechanics*

| | **Type of actuator / Use** | **Resolution** | **Reproducibility and stability** | **Range** |
|---|---|---|---|---|
| X | Remotely controlled /<br>For operation | 1 µm | 2 µm | 335 mm |
| X | Manual /<br>For alignment | 5 µm | 20 µm | 500 µm |
| Y | Manual /<br>For alignment | 5 µm | 20 µm | 500 µm |
| Z | Manual /<br>For alignment | 1 µm | 2 µm | 500 µm |
| Pitch | Manual /<br>For alignment | 0.02 mrad | 0.05 mrad | 1 mrad |
| Roll | Manual /<br>For alignment | 0.02 mrad | 0.05 mrad | 1 mrad |
| Yaw | Manual /<br>For alignment | 0.2 mrad | 0.5 mrad | 1 mrad |
| Pitch | Remotely controlled /<br>For operation | 10 nrad | 20 nrad | 30 mrad |

### Technical design considerations

A granite block will be connected to the tunnel floor through manually adjustable feet. Through remotely adjustable feet, the granite block will support a baseplate, on which the pre-mirror stands and the grating support will be mounted. The base plate and the mirrors will be inside a vacuum vessel that is mechanically decoupled from the baseplate and supported separately. Except for the motors that are dedicated to the adjustment of the base plate feet, the other remaining motors will be in-vacuum motors. Linear and rotary encoders for motor and position control and feedback will be in-vacuum devices as well.

The main aim of the granite block is to give a structural stable support and to dump the vibrations coming from the floor. During the final design phase, the component masses, material, and geometries have to be carefully chosen in order to minimize the vibrational effect.

All the monochromator component material, as well as the design and manufacture process, will be compliant with the European XFEL vacuum specification [17]. To avoid beam scattering and absorption effects, and simultaneously limit hydrocarbon contamination of the optics, the vacuum level inside the monochromator vessel will be < $10^{-9}$ mbar.

## Wavefront propagation results

To model the impact of wavefront distortions on the monochromator resolution, a Gaussian beam of corresponding photon energy and angular divergence is calculated in accordance with the empirical formula from CDR2011. As a simulation tool, an improved version of the PHASE code was used [18]. The results on the widths were in good agreement with an analytical expression for slit diffraction used in Figure 32 and Figure 33**,** and also with the ray-tracing program “Ray”. The impact on the shape of the resolution functions is shown in Figure 51 for a photon energy of 0.8 keV and in Figure 52 for a photon energy of 0.27 keV. At 0.8 keV, the grating is covering about 4$\sigma$ of the beam, and the resolution function is essentially of

Gaussian shape. At 0.27 keV, noticeable side maxima are present, which originate from the cutoff effects at pre-mirror and grating.

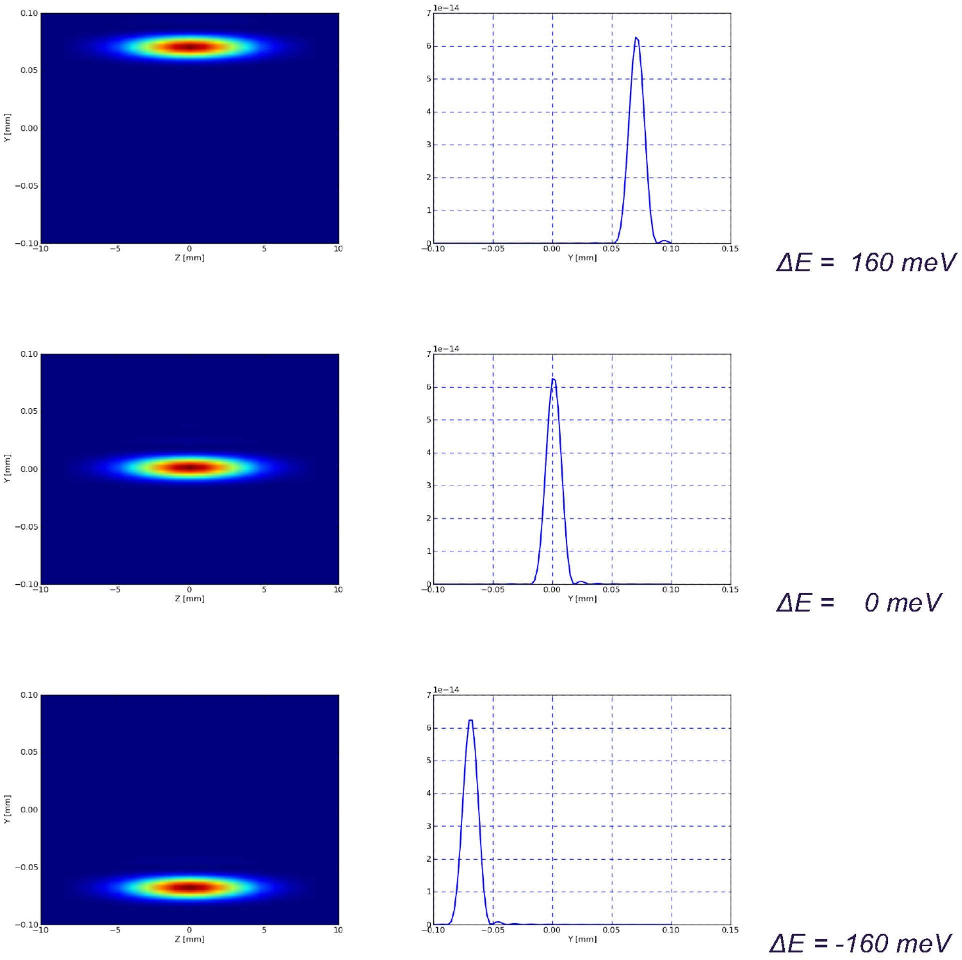

***Figure 51**:* Left: *Results of wavefront propagation through the monochromator for 0.8 keV.* Right: *Central vertical cuts.*

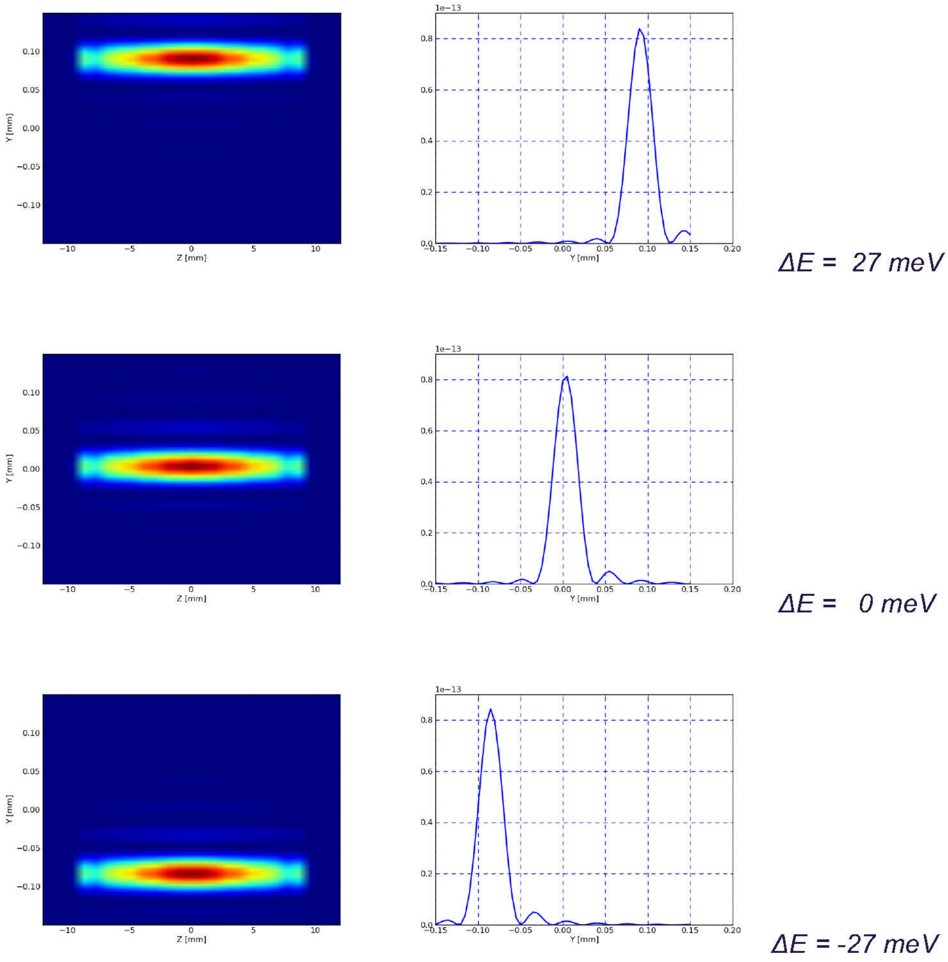

***Figure 52****:* Left: *Results of wavefront propagation through the monochromator for 0.27 keV.* Right: *Central vertical cuts.*

The impact of slope error effects [19] is demonstrated in Figure 53. The profiles used are shown in Figure 54 [20]. For profiles measured on optics with shape errors on the order of 4.5 nm and 12 nm, the achievable resolution is significantly reduced by about a factor of two.

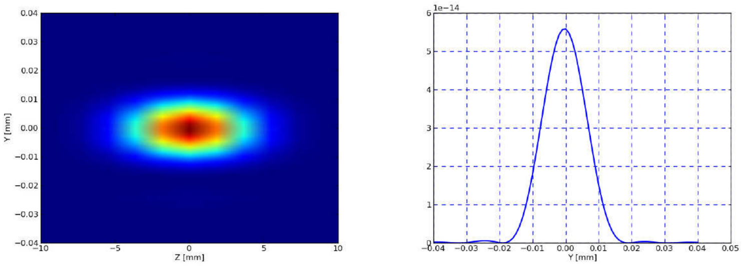

*FWHM 17 µm*

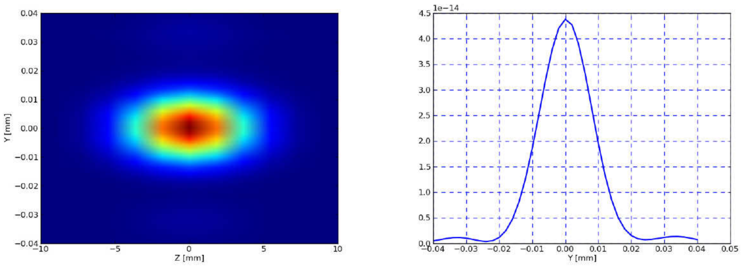

*FWHM 20 µm*

*PV: 1 nm (M3)+2.5 nm (G1)*

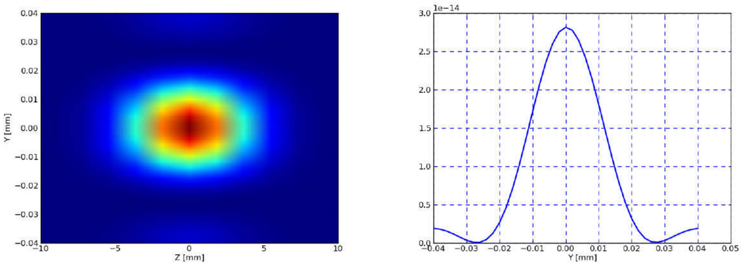

*FWHM 30 µm*

*PV: 4.5 nm (M3)+12 nm (G1)*

***Figure 53**: Top: Impact of pre-mirror and grating residual height errors on the resolution of the soft X-ray monochromator for target energy 0.7426 keV.* Middle: *Results calculated for "smoothed" surfaces, with slopes reduced 5 times.* Bottom: *Simulations for surface profile data shown in Figure 54.*

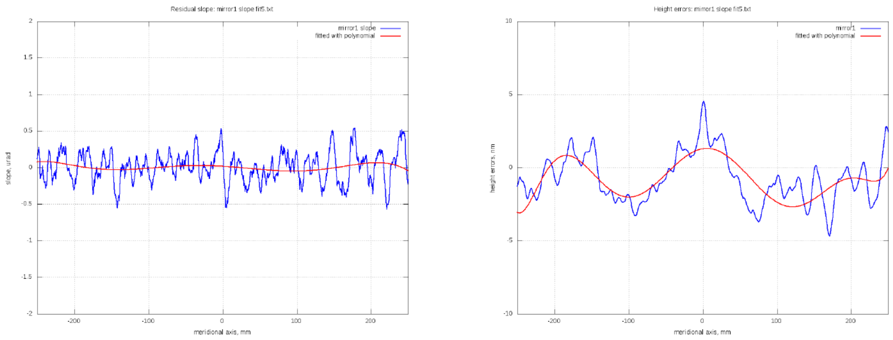

*Height error PV: 4.5 nm (M3)*

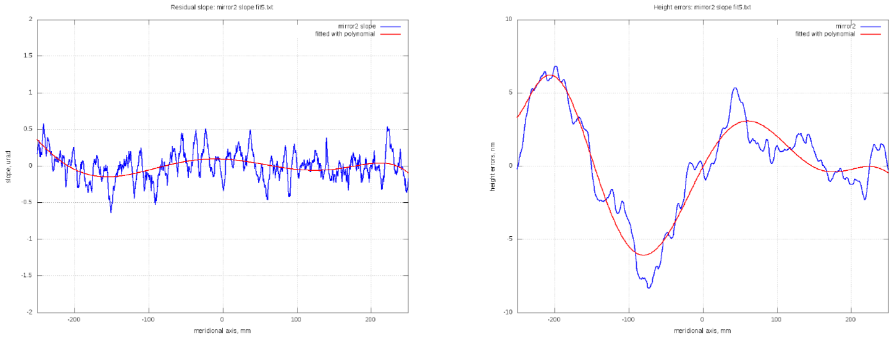

*PV: 12 nm (G1)*

***Figure 54**: Top: Pre-mirror surface residual slope (left) and height errors (right) used in wavefront propagation model. The blue curves correspond to measured data; red is the result of interpolation by the 8<sup>th</sup> order polynomial.* Bottom: *The same surface profile data for the grating.*

The influence on pulse stretching was investigated by propagating an ultrashort pulse of the same duration as the SASE3 radiation coherence time for the corresponding photon energy. Slices in frequency domain are propagated through the monochromator up to the exit slit downstream; then, for every slice, only the central area corresponding to the vertical slit width is used to get the propagated pulse in the time domain using inverse Fourier transformation. The result is shown in Figure 55. The top row shows intensity maps on the slit plane. A delta-like pulse of duration 1 fs FWHM at 800 eV is broadened by the monochromator to about 70 fs FWHM. This is very close to the value obtained by the approximation in Figure 31 of 75 fs (the ideal relative band pass is $7 \cdot 10^{-5}$).

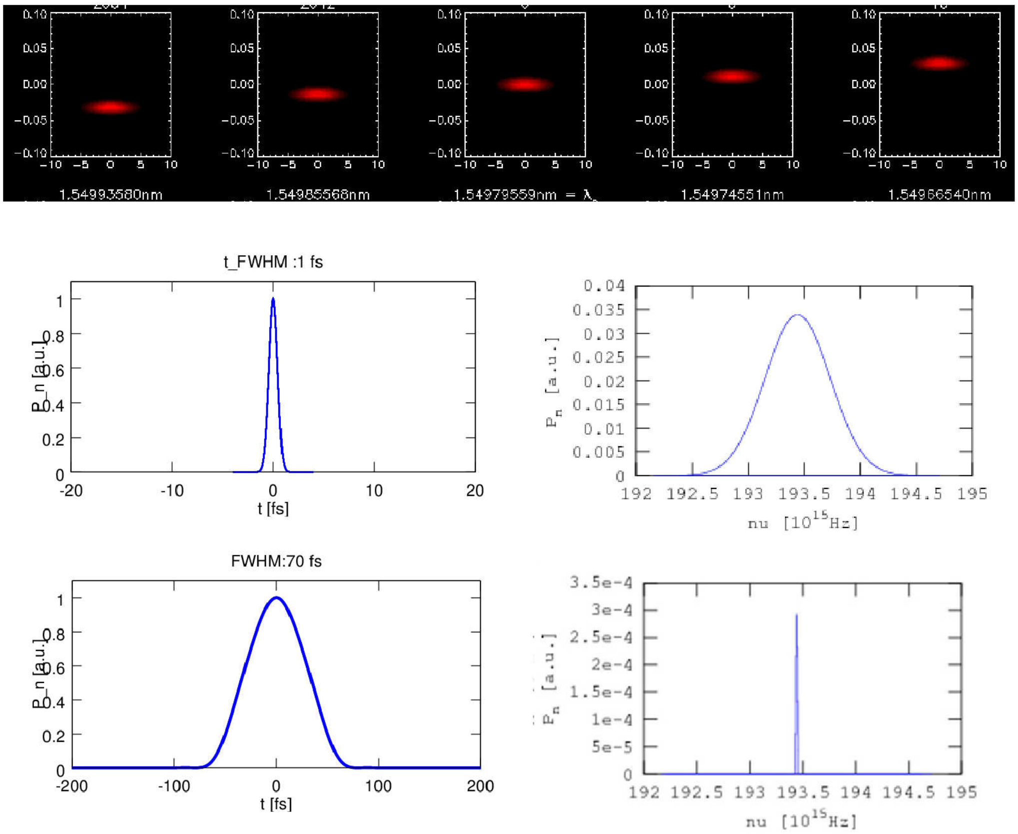

***Figure 55**: Wave optics propagation of an ultrashort pulse, 0.8 keV averaged photon energy, 1 fs FWHM pulse duration, through the soft X-ray monochromator.* Top: *Maps of intensity distribution in focus for slices in frequency domain after propagating through the monochromator.* Middle: *Pulse and its spectrum before monochromator.* Bottom: *Pulse and its spectrum after propagation through the monochromator with 50 l/mm at the exit slit of 30 µm width.*

# 5 Hard X-ray monochromator

For the hard X-ray beamlines at the European XFEL, silicon monochromators are required to cut down the relative band pass to $10^{-4}$ and $10^{-5}$ [1], [23], [24]. For this purpose, the reflections Si(111), Si(311), Si(511), or Si(333) are proposed to be used. The intrinsic energy resolution of single-crystal diffraction as a function of photon energy for different Si crystal reflections is shown in Figure 56**.**

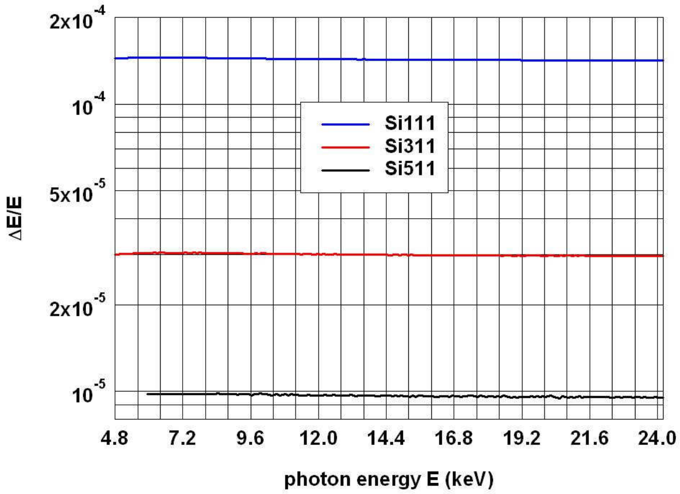

***Figure 56****: Intrinsic Darwin width of Si crystal reflections (calculated with X.R.Vision 2.0 program [25]).*

To enable high-quality polishing for minimizing wavefront distortions and to minimize vibrations, an artificial (pseudo) channel-cut monochromator type (non-monolithic) was chosen. It is similar to the design developed by Argonne National Laboratory (ANL) [26], [27], and is currently being further developed to enable cryogenic cooling in a collaboration between European XFEL and Deming Shu from ANL.

As described in CDR2011, cryogenic cooling will increase the throughput by about a factor of two. A pulse tube cooler is foreseen since the monochromator will be installed in the European XFEL tunnels, where there is no $LN_2$ supply available.

## Si crystal Bragg reflection performances

For the SASE1 and SASE2 beamlines, the Si monochromators will be used to cover an energy range of 4.8–24 keV. Figure 57 shows the Bragg angle as a function of energy for different reflections. A Bragg angle in the range of 4.5–45° covers the required energy range for the mentioned reflections.

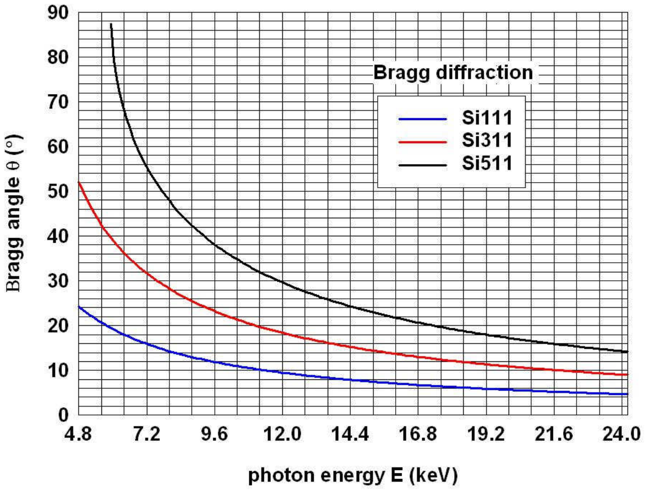

***Figure 57**: Bragg angle versus photon energy for different crystal reflections (calculated with the X.R.Vision 2.0 program).*

Figure 58 gives the bandwidth (FWHM, in μrad) as a function of energy for Bragg reflections for different reflections. “Diffraction curve” means a one-crystal rocking curve, or Darwin curve. “Rocking curve” means a two-crystal rocking curve but with only one crystal rocking.

Based on the parameters of the X-ray FEL beam from CDR2011 and the performance of the Si crystals, the critical points of designing the monochromator, such as geometry and motion, are discussed in the following paragraphs.

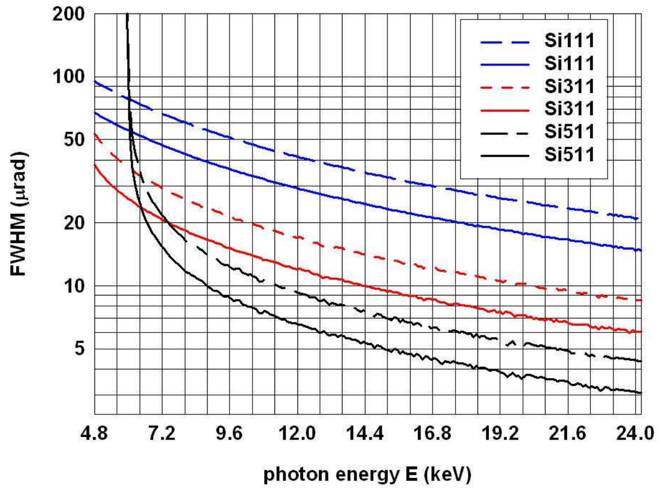

***Figure 58****: Diffraction and rocking curves as a function of photon energy for different reflections. Solid lines = “diffraction curve”, dashed lines = “rocking curve” (calculated with the X.R.Vision 2.0 program).*

## Geometry and dimensions

The nearly diffraction-limited X-ray beam changes its divergence proportional to its wavelength, leading to a variation of spot sizes with energy of about a factor of 10. This leads to challenges in optimizing geometry, gap, and length of the crystal optics.

The rotation centre of the monochromator was considered to be in between the two crystal surfaces or on the surface in the centre of the first crystal.

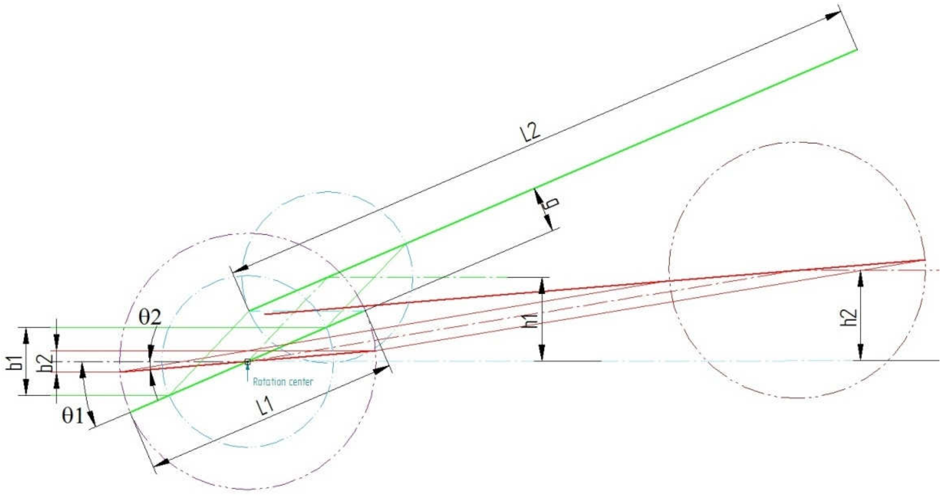

***Figure 59****: Scheme of the rotation axis on the centre of the first crystal surface*

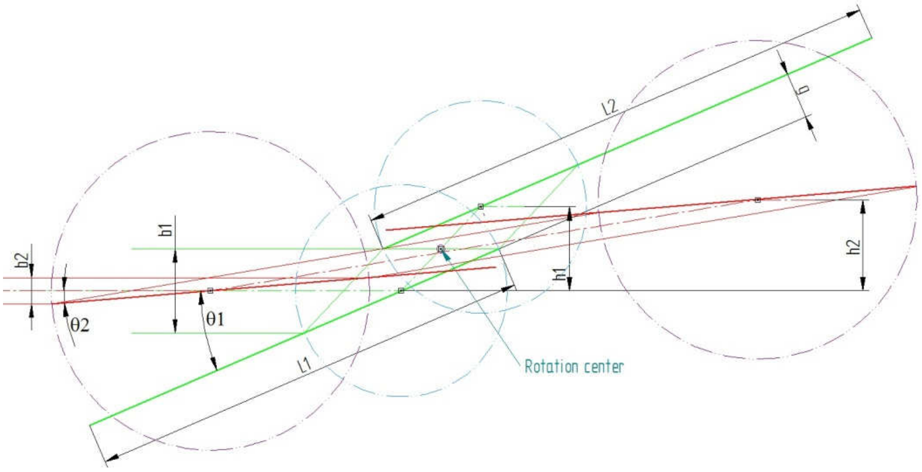

*__Figure 60__: Scheme of the rotation axis in the middle of crystal surfaces.*
*g = gap between two crystals; L = length of the crystal; b = beam size, b1 for lower energy (4.8 keV) and b2 for higher energy (24 keV); $\theta 1$ and $\theta 2$ = corresponding Bragg angle; h1 and h2 = beam offsets.*

With the rotation axis on the centre of the first crystal surface, as shown in Figure 59, one obtains the minimum length of the first crystal (footprint of the higher energy with the smaller grazing angle), but needs a long second crystal and an increased minimum gap in order to avoid shadowing the beam with the crystal ends.

The centre of rotation (COR) in the middle between the two crystal surfaces, as shown in Figure 60, leads to almost identical lengths of the two crystals and a more compact design with a small gap. This avoids a too-long length of the second crystal, especially in the Si(111) case.

One disadvantage of channel-cut monochromators is that the exit beam offset varies according to different energies and results in an offset of

$$h = 2g\cos\theta$$

$$\theta = \sin^{-1}(\frac{12.4}{2d \times E})$$

where $\theta$ is the Bragg angle, *d* is the lattice spacing of crystals in Å, and *E* is the photon energy in keV. Figure 61 shows the beam offset as a function of energies, with a gap of 5, 6.5, and 8 mm, for instance.

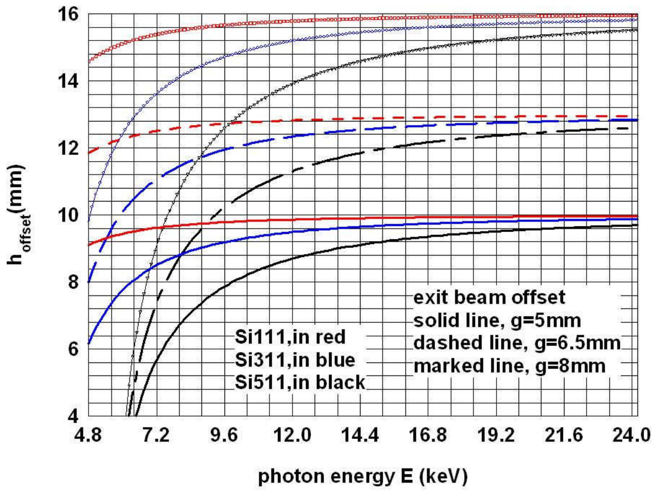

*Figure 61: Exit beam offset versus photon energy for different gaps*

The minimum gap and length for the crystals need to be optimized to cover a certain energy range. According to the two geometries, we can obtain the following equations for the dimension evaluation, respectively.

The rotation axis on the centre of the first crystal surface yields:

Gap:

$$gmin = \frac{1}{4}\left({}^{b2}/_{\sin\theta 2} - {}^{b1}/_{\sin\theta 1}\right) * \tan\theta 1 + {}^{b1}/_{2\,\cos\theta 1}$$

Length of the first crystal:

$$l1min = {}^{b2}/_{\sin\theta 2}$$

Length of the second crystal:

$$l2min = g\left({}^{1}/_{\tan\theta 2} - {}^{1}/_{\tan\theta 1}\right) + {}^{b1}/_{2\,\sin\theta 1} + {}^{b2}/_{2\,\sin\theta 2}$$

Total length:

$$lmin = g\left({}^{1}/_{\tan\theta 2} - {}^{1}/_{\tan\theta 1}\right) + {}^{b1}/_{2\,\sin\theta 1} + {}^{3b2}/_{2\,\sin\theta 2}$$

Table 17, Table 18, and Table 19 summarize the beam size on the Si(111), Si(311), and Si(511) or Si(333) monochromators, respectively, at an 850 m source distance as well as parameters of footprint, gap, and length of the crystal with the COR on the centre of the first crystal surface.

***Table 17:*** *Parameters for Si(111), COR on the centre of the first crystal*

| **Beam size** | | | | **Footprint** | | **Crystal gap** | | **Second crystal length (appr.)** | |
|---|---|---|---|---|---|---|---|---|---|
| ***E*** **(keV)** | **4σ (mm)** | **6σ (mm)** | ***θ*** **(°)** | **$l_0$(4σ) (mm)** | **$l_0$(6σ) (mm)** | **$g_{min}$(4σ) (mm)** | **$g_{min}$(6σ) (mm)** | **$L_{min}$(4σ) (mm)** | **$L_{min}$(6σ) (mm)** |
| 3 | 9.72 | 14.6 | 41.2 | 14.8 | 22.1 | 8.44 – | 15.41 – | 112 – | 198 – |
| 5 | 6.28 | 9.42 | 23.3 | 15.9 | 23.9 | 4.28 | 6.41 | 62 | 92.5 |
| 24 | 1.96 | 2.94 | 4.72 | 23.8 | 35.7 | | | | |

***Table 18:*** *Parameters for Si(311), COR on the centre of the first crystal*

| **Beam size** | | | | **Footprint** | | **Crystal gap** | | **Second crystal length (appr.)** | |
|---|---|---|---|---|---|---|---|---|---|
| ***E*** **(keV)** | **4σ (mm)** | **6σ (mm)** | ***θ*** **(°)** | **$l_0$(4σ) (mm)** | **$l_0$(6σ) (mm)** | **$g_{min}$(4σ) (mm)** | **$g_{min}$(6σ) (mm)** | **$L_{min}$(4σ) (mm)** | **$L_{min}$(6σ) (mm)** |
| 5 | 6.28 | 9.42 | 49.2 | 8.3 | 12.4 | 6.00 | 9.01 | 42.6 | 64 |
| 24 | 1.96 | 2.94 | 9.1 | 12.4 | 18.6 | | | | |

***Table 19:*** *Parameters for Si(511) or Si(333), COR on the centre of the first crystal*

| **Beam size** | | | | **Footprint** | | **Crystal gap** | | **Second crystal length (appr.)** | |
|---|---|---|---|---|---|---|---|---|---|
| ***E*** **(keV)** | **4σ (mm)** | **6σ (mm)** | ***θ*** **(°)** | **$l_0$(4σ) (mm)** | **$l_0$(6σ) (mm)** | **$g_{min}$(4σ) (mm)** | **$g_{min}$(6σ) (mm)** | **$L_{min}$(4σ) (mm)** | **$L_{min}$(6σ) (mm)** |
| 8 | 4.63 | 6.95 | 47.9 | 6.24 | 9.36 | 3.92 | 5.88 | 18.9 | 28.4 |
| 24 | 1.96 | 2.94 | 14.3 | 7.94 | 11.9 | | | | |

The rotation centre in the middle between crystal surfaces yields:

Gap:

$$gmin = {}^{b1}/_{2\,\cos\theta 1}$$

Length of the first or second crystal:

$$l1{,}2min \approx \frac{g}{2}\left({}^{1}/_{\tan\theta 2} + {}^{1}/_{\tan\theta 1}\right) + {}^{b2}/_{2\,\sin\theta 2}$$

Total length:

$$lmin = g\left({}^{1}/_{\tan\theta 2} + {}^{1}/_{\tan\theta 1}\right) + {}^{b2}/_{2\,\sin\theta 2}$$

Table 20, Table 21, and Table 22 summarize the beam size on the Si(111), Si(311), and Si(511) or Si(333) monochromators at 850 m as well as parameters of footprint, gap, and length of crystal with the COR in between the crystal surfaces.

***Table 20:** Parameters for Si(111), COR in between crystals*

| **Beam size** | | | | **Footprint** | | **Crystal gap** | | | | **Crystal length (appr.)** | | | |
|---|---|---|---|---|---|---|---|---|---|---|---|---|---|
| **$E$ (keV)** | **$4\sigma$ (mm)** | **$6\sigma$ (mm)** | **$\theta$ (°)** | **$l_0(4\sigma)$ (mm)** | **$l_0(6\sigma)$ (mm)** | **$g_{min}(4\sigma)$ (mm)** | | **$g_{min}(6\sigma)$ (mm)** | | **$L_{min}(4\sigma)$ (mm)** | | **$L_{min}(6\sigma)$ (mm)** | |
| 3 | 9.72 | 14.6 | 41.2 | 14.8 | 22.1 | 6.46 | – | 9.69 | – | 59 | – | 89 | – |
| 5 | 6.28 | 9.42 | 23.3 | 15.9 | 23.9 | | 3.42 | | 5.12 | | 41 | | 62 |
| 24 | 1.96 | 2.94 | 4.72 | 23.8 | 35.7 | | | | | | | | |

***Table 21:** Parameters for Si(311), COR in between crystals*

| **Beam size** | | | | **Footprint** | | **Crystal gap** | | **Crystal length (appr.)** | |
|---|---|---|---|---|---|---|---|---|---|
| **$E$ (keV)** | **$4\sigma$ (mm)** | **$6\sigma$ (mm)** | **$\theta$ (°)** | **$l_0(4\sigma)$ (mm)** | **$l_0(6\sigma)$ (mm)** | **$g_{min}(4\sigma)$ (mm)** | **$g_{min}(6\sigma)$ (mm)** | **$L_{min}(4\sigma)$ (mm)** | **$L_{min}(6\sigma)$ (mm)** |
| 5 | 6.28 | 9.42 | 49.2 | 8.3 | 12.4 | 4.81 | 7.21 | 23.3 | 34.9 |
| 24 | 1.96 | 2.94 | 9.1 | 12.4 | 18.6 | | | | |

***Table 22:** Parameters for Si(511) or Si(333), COR in between crystals*

| **Beam size** | | | | **Footprint** | | **Crystal gap** | | **Crystal length (appr.)** | |
|---|---|---|---|---|---|---|---|---|---|
| **$E$ (keV)** | **$4\sigma$ (mm)** | **$6\sigma$ (mm)** | **$\theta$ (°)** | **$l_0(4\sigma)$ (mm)** | **$l_0(6\sigma)$ (mm)** | **$g_{min}(4\sigma)$ (mm)** | **$g_{min}(6\sigma)$ (mm)** | **$L_{min}(4\sigma)$ (mm)** | **$L_{min}(6\sigma)$ (mm)** |
| 8 | 4.63 | 6.95 | 47.9 | 6.24 | 9.36 | 3.45 | 5.18 | 13.1 | 19.6 |
| 24 | 1.96 | 2.94 | 14.3 | 7.94 | 11.9 | | | | |

In conclusion, the COR on the centre of the first crystal leads to a longer second crystal and a larger gap. In order to accept 6σ for Si(111), a 92.5 mm second crystal is required. We consider this as too long to be compatible with the artificial channel-cut concept, without risking mechanical instability. In contrast, a COR in between the crystals leads to a significantly shorter second crystal. This concept was refined and led to a COR that is on the downstream end of the first crystal surface. This design has the advantage that both crystals are of equal (minimal) length and that the rotation can be better monitored using an autocollimator.

The dimensions of Si(111) crystals are defined as shown in Figure 62. They include some extra length as a safety factor and extend the energy range down to 4.84 keV ($\theta = 24.1°$) to include the Ti edge. With the similar consideration, Si(511) crystal dimensions are defined as shown in Figure 63**.**

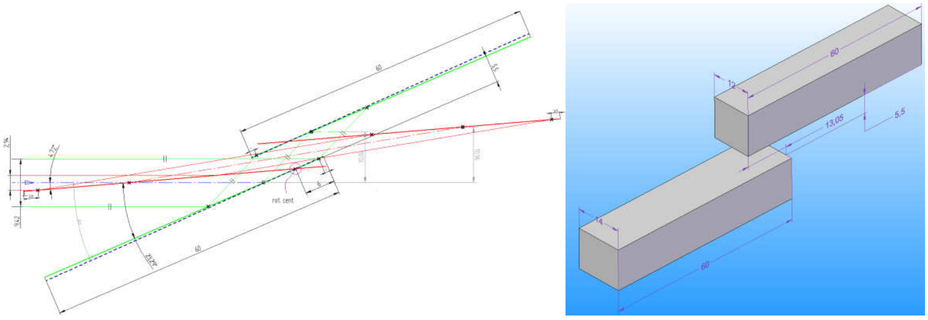

***Figure 62****: Si(111) crystal dimensions with gap = 5.5 mm for 4.8–24 keV of 4$\sigma$ beam size, L1 = L2 = 60 mm, h1 = 10.1 mm, and h2 = 10.96 mm. A range of 19.5$^{o}$ for rotation is required for the mechanics.*

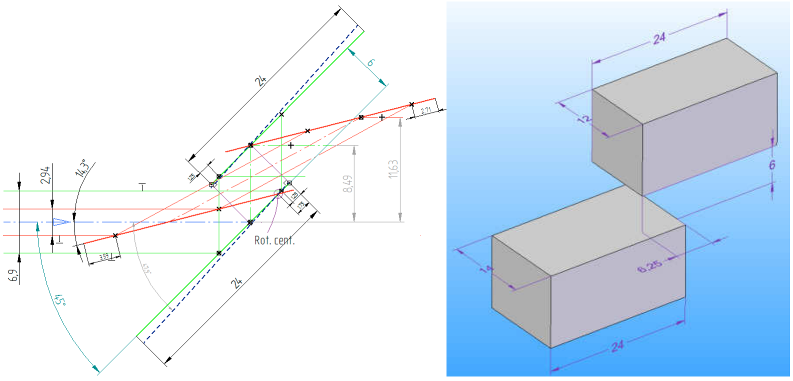

***Figure 63****: Si(511) crystal dimensions with gap = 6 mm for 8–24 keV of 4$\sigma$ beam size, L1 = L2 = 24 mm, h1 = 8.49 mm, h2 = 11.63 mm. A range of 34.1$^{o}$ for rotation is required for the mechanics.*

As shown in Figure 62 and Figure 63, the first crystal is designed to be 2 mm wider than the second one for the initial alignment using only one reflection.

## Motion requirement

As discussed above, a combined pitch of both crystals for Bragg angle rotation and adjustments of the second crystal related to the first one are foreseen. Movements of both crystals, to allow adjustment of the monochromator according to the X-ray beam and to enable pink-beam mode of the beamlines, are taken into account as well.

The motions needed are summarized and the ranges are shown in Figure 64.

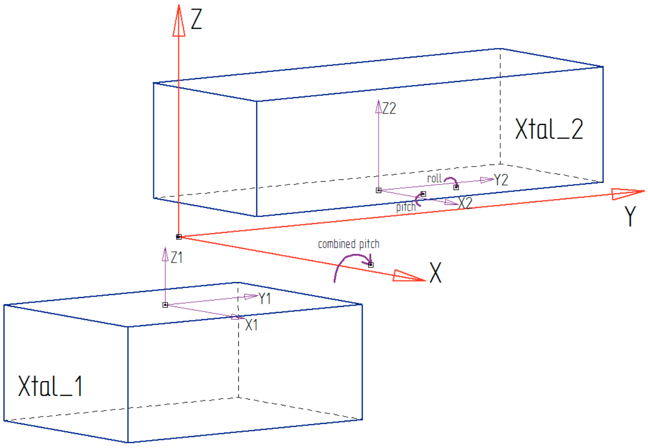

***Figure 64**: Coordinates of the crystals*

For the channel-cut, the required motions are:

- $R_X$ (pitch), Bragg angle for Si(111) of 20° (from 4.5–24.5°), Bragg angle for Si(511)/Si(333) of 35°(from 13–48°).
- Tx, ± 15 mm, retract from the beam axis for other application modes;
- Tz, ± 15 mm, height adjustment to the beam axis.

For the second crystal:

- $R_{X2}$, adjustment of pitch between first and second crystal, of ± 0.5° and also fine adjustment (piezo);
- $R_{Y2,}$ adjustment of roll of second crystal, of ± 0.5°.

Based on the geometrical ray tracing of the beam position, effects of tolerance or misalignment of the pitch and roll movement on the beam at the sample are considered:

$$\Delta z_0 = 2 \times \Delta\theta \times q$$

$$\Delta x_0 = 2 \times \Delta\varphi \times q \times \sin\theta$$

where $q$ is the distance from the monochromator to the sample. The effect on the beam spot centre position is shown in Figure 65.

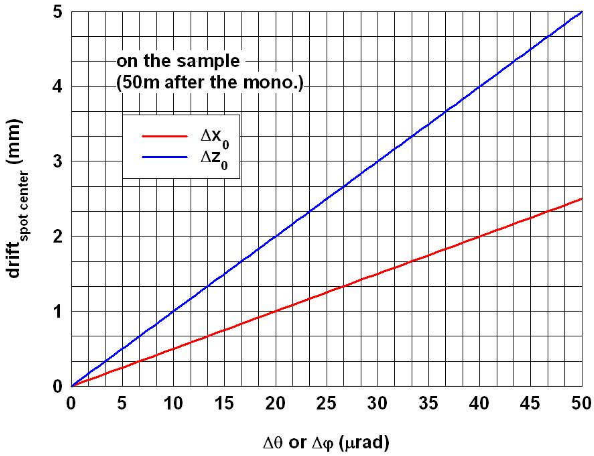

***Figure 65****: Pitch and roll tolerance effects on spot drift at a Bragg angle of 24.5°*

The effects of vibrations and thermal drifts are sensitive to the distance between the monochromator and sample position. Therefore, putting the monochromator closer to the experiment station will improve the stability of the beam position.

## Pre-monochromator and high-resolution monochromator application

Si(111) will be used as a pre-monochromator and a second monochromator (e.g. Si(311) and Si(511) or Si(333)) will be used in series, which will further improve the energy resolution according to the instrument scientific requests. This may also compensate part of the vertical offset and brings the beam back toward the optical axis as shown in Figure 66.

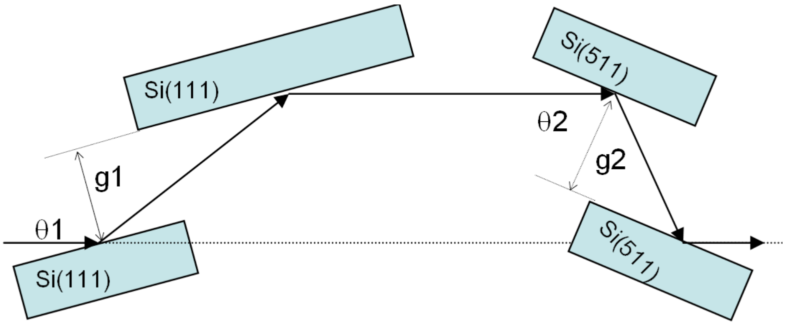

***Figure 66****: Scheme of a series of monochromators (Si(111) + Si(511), for example)*

To keep the monochromatic beam at the same exit position as the pink beam, we need to adjust the gaps between crystals according to the energy,

$$h = 2g_1 \cos\theta_1 = 2g_2 \cos\theta_2$$

$$\frac{g_1}{g_2} = \frac{\cos\theta_2}{\cos\theta_1}$$

Another option to get the same exit beam is to tilt an upstream mirror (e.g. distribution mirror or offset mirror before the monochromator) on the beamline by an angle of a few mrad ($\Delta\varphi$) around the beam axis (Figure 67).

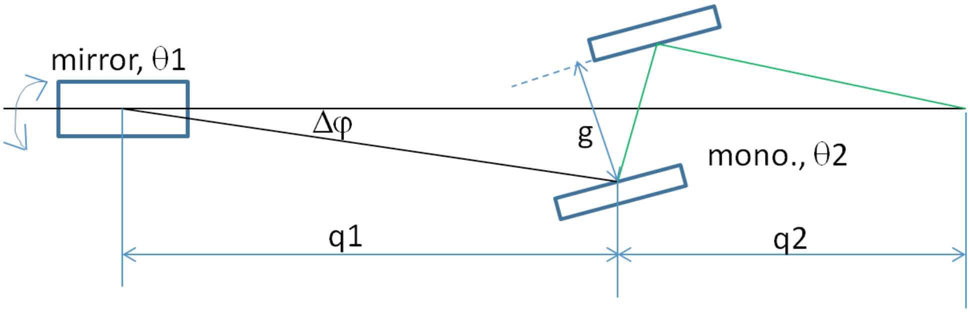

***Figure 67**: Scheme of fixed exit beam with upstream mirror adjustment*

According to the equations above,

$$2\Delta\varphi \times (q1 + q2) \times \sin\theta 1 = 2g \times \cos\theta 2$$

$$\Delta\varphi = \frac{g \times \cos\theta 2}{(q1 + q2) \times \sin(2\,\theta 1)}$$

where $\theta 1$ is the grazing angle at the upstream mirror, $\theta 2$ is the Bragg angle of the monochromator, and *g* is the gap between the crystal surfaces.

# Cryo-cooling consideration

As also discussed in CDR2011, thermal load is a critical problem for the Si monochromator at the European XFEL and cryogenic cooling of the Si crystal is foreseen. Si crystal thermal properties (thermal conductivity and expansion coefficient) are shown in Figure 68, as a function of temperature.

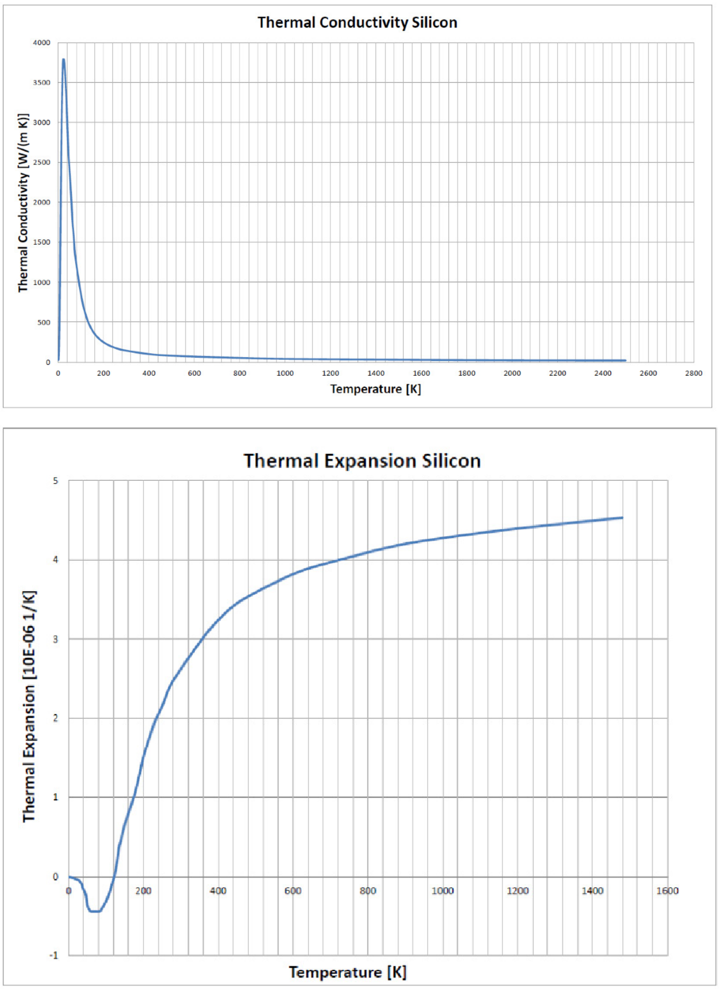

***Figure 68**: Temperature-dependent thermal properties for silicon*

At 100 K, the thermal expansion of silicon is becoming minimal with a relatively high thermal conductivity coefficient. Apart from the analytical approximation of the thermal transfer to evaluate the maximum pulses transmitted and one-dimensional FEA of the peak temperature calculation, which are presented in CDR2011, three-dimensional FEA simulations of the crystal temperature gradient and thermal-bump effects under the thermal load of the FEL beam were now performed using the ANSYS software. Table 23 indicates the parameters for the FEA simulations input: a charge of 250 pC and 2700 pulses per train are taken into account for the power and the train length of the FEL beam, based on the numbers from CDR2011.

***Table 23:*** *Parameters for simulations*

| ***E*** **(photon) (keV)** | **Power, *W* (pulse train)** | **Power, *W* (steady state)** | **Train length ($10^{-3}$ s)** | **Bragg angle *θ* (Si111)** | **Abs. length (µm)** |
|---|---|---|---|---|---|
| 12.3 | 1740 | 5 | 0.6 | 9 | 221 |

A Gaussian distribution of the thermal load and exponential decay through the crystal have been implemented in the model as shown in Figure 69**.** A quarter of the crystal size was taken into account because of the symmetrical geometry.

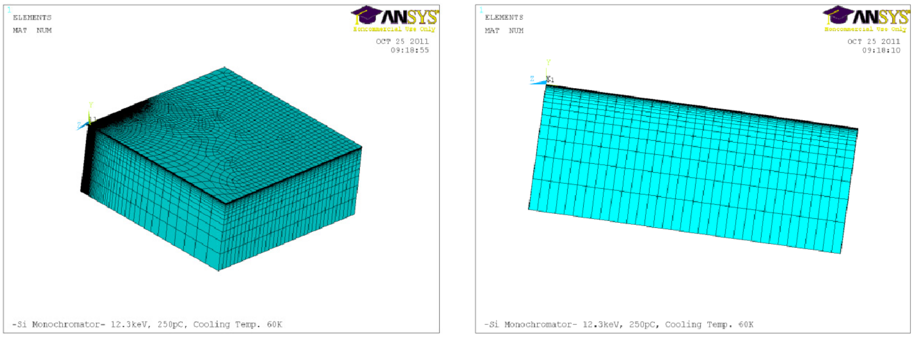

***Figure 69****: 3D model for FEA simulations*

Figure 70 indicates the temperature distribution and thermal deformation at the end of a full pulse train at 80 K cooling.

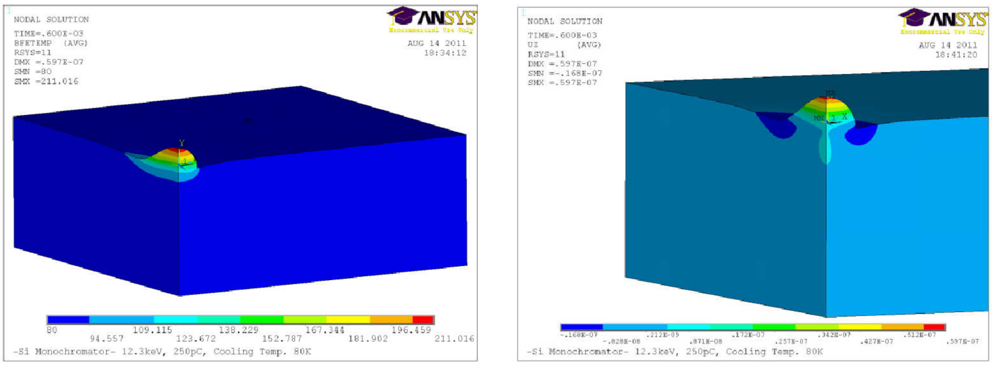

***Figure 70**:* Left: *Temperature distribution [K].* Right: *Displacement perpendicular to the incident surface [m] at the end of a full pulse train.*

Figure 71 shows the thermal-bump effect as a function of time during a full pulse train. The PV displacement is 30 nm at 60 K for the cooler.

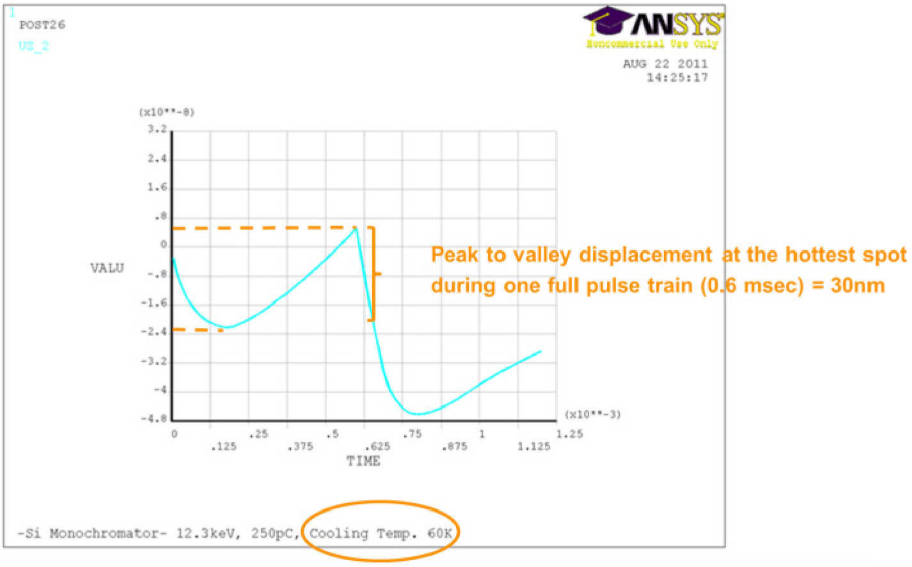

***Figure 71:** Thermal-bump effect as a function of time*

The maximum thermal-bump deformation has been investigated for a full pulse train (2700 pulses) for different cooling temperatures between 40 K and 120 K, as shown in Figure 72. For this particular heat load case, 60 K seems to be the optimum temperature for the first crystal. With a smaller heat load, this ideal temperature will be higher.

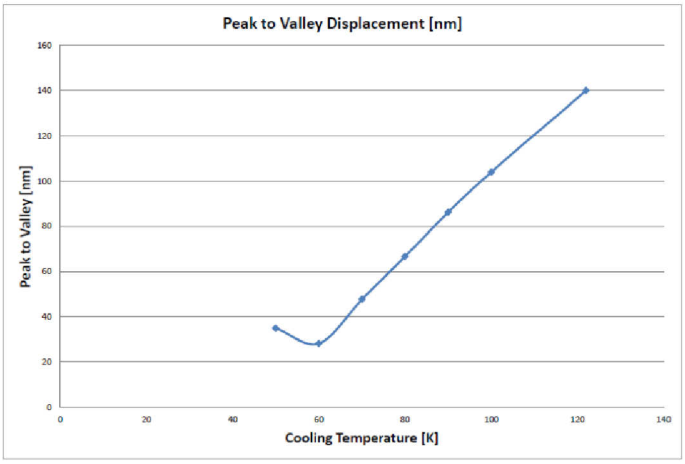

***Figure 72**: Thermal-bump effect as a function of cooling temperature*

In order to investigate the feasibility of the cooling, tests on a dummy crystal with a commercial pulse tube cooler (Transmit PTS 8030) were performed. The experiment facility is shown in Figure 73, including the pulse tube cooler and a small vacuum chamber.

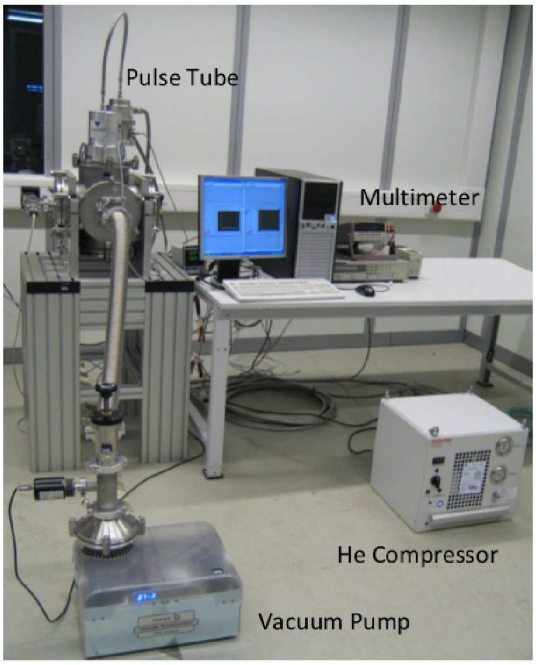

***Figure 73**: Test experiment setup*

The dummy crystal (aluminium block) is mounted on a copper plate (Figure 74), which is insulated by ceramic supports and connected to the cold finger of the cooler. A 50 Ω resistor is installed on the dummy crystal as a heater to generate a thermal load. A PT100 sensor is used to measure the temperature.

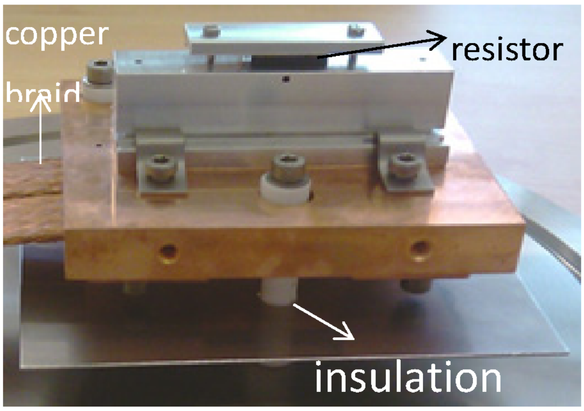

*__Figure 74__: Dummy crystal for test*

The dimensions of the copper braid and how it connects to the crystal support and the cooler are important for the cooling performance. According to thermal conduction equations, the heat flow with respect to temperature difference can be estimated as:

$$Q = k(T)A\frac{dT}{dx}$$

where *Q* is the power on the crystal, *k* is the thermal conductivity, *A* is the cross section area, and *dx* is the length of copper braid.

Two configurations of connections, one with longer length but smaller cross section, the other vice versa, were tested as shown in Figure 75 and Figure 76**.** The measured results are shown on the right panels.

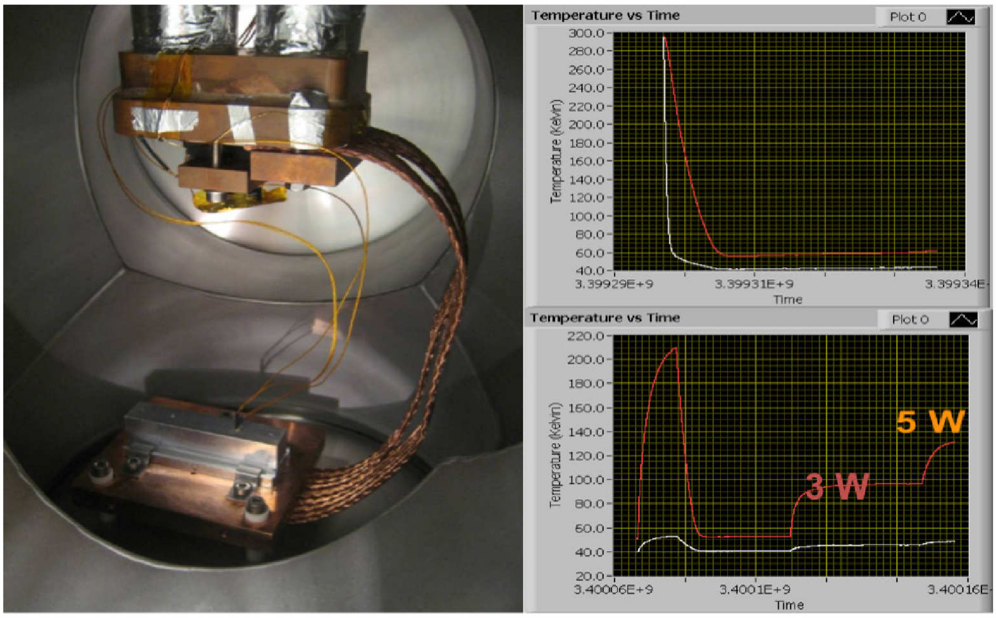

*Figure 75: Connection 1 and results (250 mm length, 2 x 20 mm$^2$)*

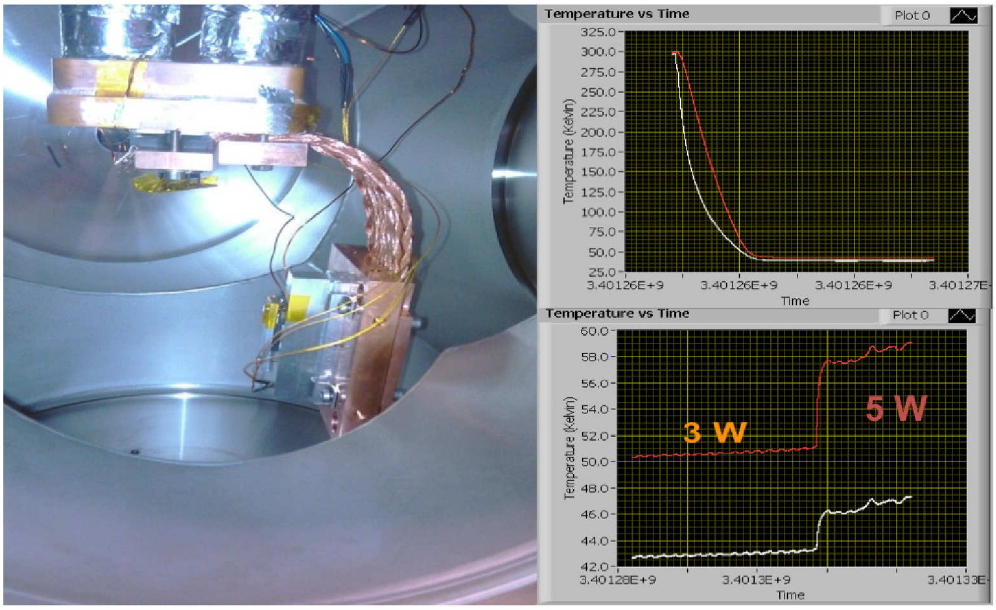

*Figure 76: Connection 2 and results (90 mm length, 1 x 100 mm$^2$)*

***Table 24:** Summary of different connections*

| | **Experiment measurement** | | | | | | **Calculation estimation** | | | | | |
|---|---|---|---|---|---|---|---|---|---|---|---|---|
| | | | **$Q$ = 3 W** | | **$Q$ = 5 W** | | **$Q$ = 3 W** | | | **$Q$ = 5 W** | | |
| | **dx (mm)** | **$A$ (mm$^2$)** | **$T1$ (K)** | **$T2$ (K)** | **$T1$ (K)** | **$T2$ (K)** | **$\Delta T$ (K)** | **dx (mm)** | **$A$ (mm$^2$)** | **$\Delta T$ (K)** | **dx (mm)** | **$A$ (mm$^2$)** |
| Case 1 | 250 | 2×20 | 45 | 90 | 55 | 125 | 45 | 240 | 42 | 70 | 224 | 45 |
| Case 2 | 90 | 1×100 | 40 | 50 | 45 | 58.5 | 10 | 133 | 68 | 13.5 | 108 | 83 |

The measurements are summarized in Table 24. They are in agreement with expectations (copper thermal conductivity $k$ = 400 W/(m·K)). Therefore, an optimization can be performed according to the equations given above.

Next, the length of the copper braids to cover the rotation range is considered in Figure 77.

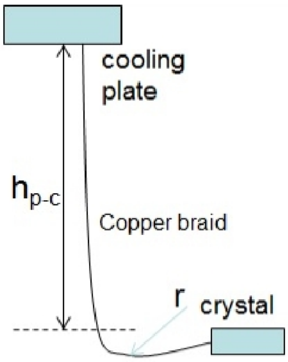

***Figure 77**: Scheme of copper braid connection*

The minimum length of the copper braid is

$$l_{braid} = h_{p-c} + \frac{\alpha}{360}(\pi \times 2 \times r)$$

With $h_{p\text{-}c}$ = 100 mm, $r$ = 50 mm (distance of braid connection to centre of rotation) and $\alpha$ = 35°:

$$l_{braid} = 100 + \frac{35}{360}(\pi \times 2 \times 50) = 130.5mm$$

The moment needed to bend the copper braid (anti-force on the crystal rotation) is

$$M_{braid} = E \times I \times r^{-1} = E \times \frac{At^2}{12} \times r^{-1}$$

Where $A$ (= $w \cdot t$) and $w$ and $t$ are the width and thickness, respectively, of the cross section of the copper braid. With $E$ = 110 GPa for the Young modulus of the copper braid, and assuming $A$ = 40 x 1 mm$^2$, one obtains

$$M_{braid} = 110 \times 10^9 \times \frac{40 \times 10^{-6} \times (1 \times 10^{-3})^2}{12} \times (50 \times 10^{-3})^{-1} = 7.3 N \cdot m$$

The moment $M_{\text{braid}}$ and its fatigue lifetime will be also verified by a sample braid test.

One important question is whether the second crystal needs to be cryo-cooled as well or if a cooling at room temperature is sufficient. If the first crystal is cryo-cooled (e.g. 100 K) and second is at room temperature (e.g. 300 K), the silicon thermal expansion coefficient changes almost linearly between 100 K and 300 K, and

$$\frac{\Delta d}{d} = 2.55 \times 10^{-4}$$

where $d$ is the spacing between the planes in the atomic lattice.

Assuming $\theta$ as the Bragg angle at 100 K, and $\delta$ is the angle change at 300 K for the same photon energy, then

$$(d + \Delta d) \sin(\theta - \delta) = d \sin\theta$$

$$\delta \approx \tan\theta \times \frac{\Delta d}{d} = 2.55 \times 10^{-4} \tan\theta$$

The Bragg angle variation for working at different temperatures as a function of photon energy is shown in Figure 78.

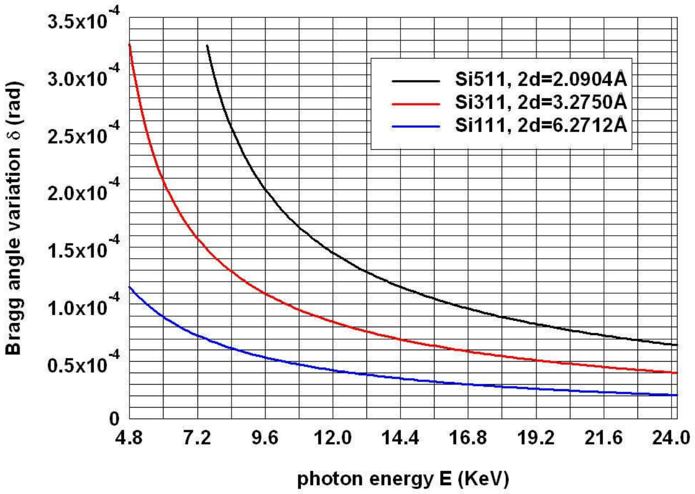

***Figure 78**: Angle variation due to temperature difference*

For Si(111) crystals, if the first crystal works at 45° at 100 K, for example, then the second one (at 300 K) gets an angle variation of about 0.25 mrad. This will amount to many mm of beam displacement in addition to the offset in the experiment hall. Therefore, cooling of the second crystal is required. The connection of the second crystal, either to the cooling plate of the first crystal or to the cryostat directly, has to be evaluated.

Heaters on both crystals are also foreseen to adjust temperatures during operation and to control the process of temperature equilibration as well.

# Mechanical design

## Artificial channel-cut mechanisms (ACCM)

The ACCM [26], [27], [28] developed by Deming Shu et al. at the Advanced Photon Source (APS), is a stable mechanism that facilitates the alignment of an assembly of two crystals to achieve the same mechanical performance as a single channel-cut crystal. The high-stiffness weak-link mechanism, as shown in Figure 79, consists of three sub-assemblies: one compact sine-bar driving mechanism and two crystal holders.

The first crystal is mounted on a cooled crystal holder fixed to the base plate. The over-constrained, flexure-based weak-link structure for fine tuning the pitch of the second crystal relative to the first crystal is driven via a compact sine-bar by a combination of an in-vacuum piezo-motor (for example, New Focus Picomotor 8301-UHV) and a piezoelectric transducer (PZT) (for example, Physik Instrumente P-841-15 mm travel). Since both drives have a ball tip, an interface plate coupled using a pair of high-stiffness linear weak-link modules is used to create a stable interface between the two ball tip stages. A rough pitch adjustment is done with the open-loop piezo-motor providing 40 nm (300 nrad) resolution and a fine pitch adjustment with the closed loop–controlled PZT with a strain gauge sensor providing 4 nm (30 nrad) resolution.

A pair of flexure bearings (e.g. C-flex pivot, G20) is driven by an in-vacuum piezo-motor for the roll of the second crystal relative to the first crystal, with the combination of a yoke assembly. An angular drift of the two crystals of less than 25 nrad/h was measured by APS for such a mechanism [27].

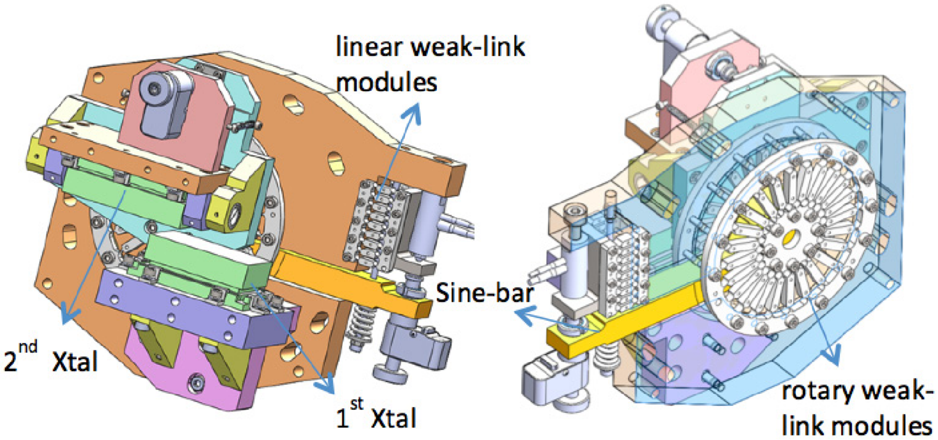

*Figure 79: Front and back view of an artificial channel-cut mechanism (ACCM)*

Two sets of stacked thin-metal weak-link modules are used in the driving mechanism: one acting as a pair of rotary bearings for a planar rotary shaft (as shown in Figure 80), the other as a linear stage to support a coupling plate between piezo-motor and PZT translator as mentioned above. Both weak-link mechanisms have two modules mounted on each side of the base plate.

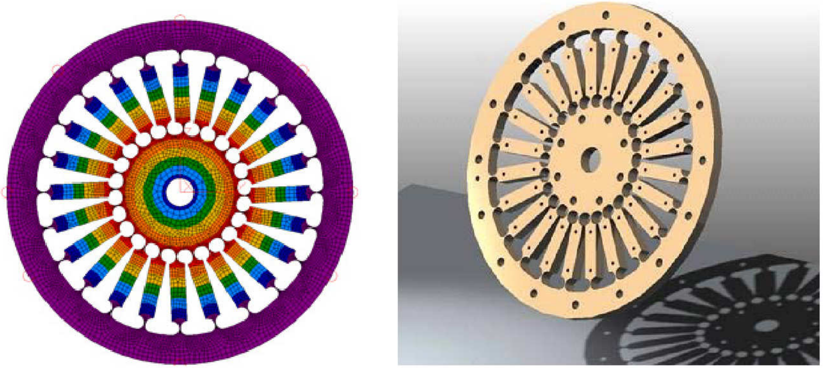

***Figure 80:*** *Over-constrained rotary weak-link module [28].* Left: *FEA simulation, showing the displacement distribution under a 0.89 Nm torsion load on the centre part while the outer ring is fixed on the base (maximum displacement 94 µm with maximum von Mises stress 175 MPa).* Right: *Model manufactured by AJR Industries. It consists of 16 layers of stainless-steel weak-link sheets bonded together with a total thickness of 4 mm (pictures from Deming Shu, APS).*

Unlike traditional kinematic linear spring mechanisms, the over-constrained weak-link mechanism provides much higher structure stiffness and stability. The laminar structure was manufactured by chemical etching and lithography techniques. Special care was taken to minimize any virtual leaks during the bonding process. The modules were tested for UHV after a bake-out at 373 K for 24 h by APS [26], [27], and a base pressure of $2\cdot10^{-10}$ mbar was attained after pumping for 24 h. A residual-gas analysis showed no detectable traces of hydrocarbon contamination.

## Sine-bar mechanism for the Bragg angle rotation

A precision hollow shaft supported by three sets of ceramic bearings, inside a precisely machined rigid housing, permits stable angular rotation of the two-crystal assembly by means of a sine-bar mechanism. The sine-bar is rigidly mounted to the shaft and has a 20° or 35° rotation range (e.g. 4.5–24.5° or 13–48°) that corresponds to an energy range of 4.8–24 keV using Si(111) or 8–24 keV using Si(511) crystals. It is also suitable for Si(311) with a certain energy range.

The long shaft supported at the ends by high-precision bearings provides exceptional stiffness and rigidity to the sine-bar. The sine-bar is driven by an UHV-compatible high-resolution linear stage. For example, a ~10 nm closed-loop linear-resolution stage from ALIO Industries with a Nanomotion nanomotor based on an UHV-compatible linear grating encoder was used by APS [27]. In this way, vacuum forces arising from motion transmitted through the bellows are eliminated and a more compact design becomes possible.

In the previous APS design, as shown on the left side of Figure 81, the sine-bar arm is coupled to the driving mechanism with a set of anti-backlash springs. The springs provide the restoring force to ensure that the sine bar always stays in contact with a ruby ball when the stage is moved. However, it will be difficult to cover a larger angle range of more than 25° with a good reproducibility. To reach such a larger angular range, a new design with flexure bearing (e.g. C-Flex pivot) joints is proposed, as shown on the right side of Figure 81.

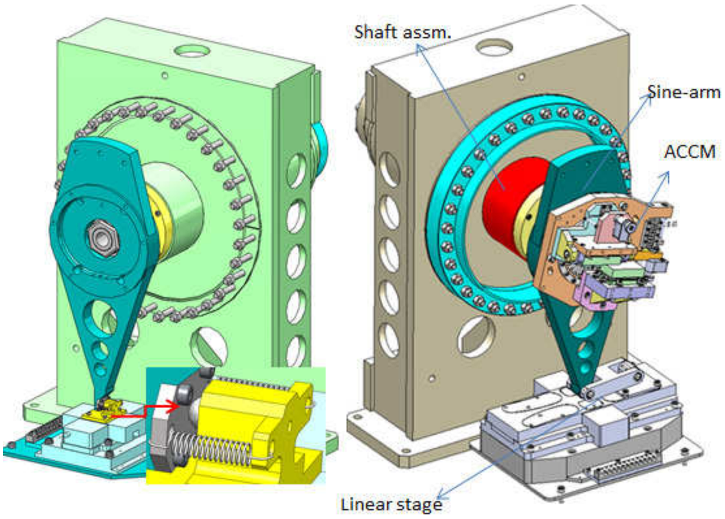

***Figure 81**: Left: Ruby ball interface. Right: Linkage with flexure bearing joints.*

One concern regarding the new design is that the flexure joints will add some low eigenfrequencies to the system. The sine-bar mechanism for the combined pitch motion of the two crystals is sketched in Figure 82.

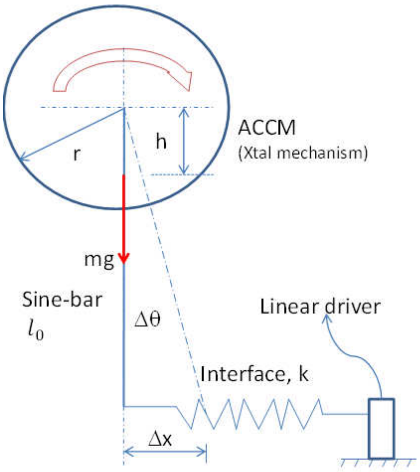

***Figure 82**: Scheme of sine-bar driven mechanism with $l_0 = 215\ mm, h = 72\ mm$, $r = 100\ mm, m = 5\ kg$*

The motion of the linear driver *x* is then

$$x = 2 \times l_0 \times \sin(\frac{\alpha}{2}) \quad (\alpha = 35°)$$

$$x = 2 \times 215 \times \sin(\frac{35°}{2}) = 2 \times 65.5 = 131\ \text{mm}$$

To cover the rotation angle range of 35°, a minimum stroke of the linear stage of 131 mm is required. The angular resolution is

$$\Delta\theta \sim \frac{\Delta x}{l_0} = \frac{1}{215 \times 10^{-3}} \Delta x = 4.7\ \Delta x[\mathrm{m}]$$

Therefore, if the linear stage has a resolution of 10 nm, the ACCM get an angular resolution of about 50 nrad.

Assuming a simple harmonic motion of the spring–mass system, and taking into account the rotational motion of the ACCM, one gets

$$F = m\frac{d^2x}{d^2t} = -kx$$

The equivalent spring constant is

$$\mu = \frac{kx * l_0}{\Delta\theta} = \frac{kx * l_0}{\frac{\Delta x}{l_0}} = k{l_0}^2$$

The moment of inertia of the ACCM is

$$I = \frac{1}{2}mr^2 + mh^2$$

Then the assumed spring dynamic motion frequency is

$$f = \frac{1}{2\pi}\sqrt{\frac{\mu}{I}} = \frac{1}{2\pi}\sqrt{\frac{k{l_0}^2}{m\left(\frac{1}{2}r^2 + h^2\right)}}$$

Taking the *k* value of 1.8·$10^6$ N/m (C-Flex webpage, G10, radial stiffness in compression condition = 0.00010, in inches of deflection per pound of load), then

$$f = \frac{1}{2\pi}\sqrt{\frac{1.8 \times 10^6 \times (0.215)^2}{\frac{1}{2} \times 5 \times (0.1)^2 + 5 \times (0.072)^2}} = 203.5\ \mathrm{Hz}$$

Here we considered the system without damping. If damped motion is taking into account, the frequency should be a bit lower.

The influence of the driver was neglected, but could be important, especially when energy scans are performed, for example with 1 eV per 0.1 second.

With the preliminary calculation described above, the proposed design looks feasible, provided that the oscillations of the real system dampen out in the 100 ms between two pulse trains. Further simulations, taking into account the real condition of the linkage and distribution of the mass of the mechanism with a 3D model, will be done for final verification.

### Vacuum tank and support table

The complete chamber with the design of all the in-vacuum motion for the crystals is shown in Figure 83. The vacuum chamber consists of two major sub-assemblies: a main chamber (including an interface port to a pulse tube cooler and an assembly access with view port) and a sine-bar support shaft chamber. The big gasket has some (tight) tolerance for the mounting of the shaft, which holds the main sine-bar mechanisms.

The main chamber has a base mounting plate for the monochromator's vertical diffraction operation configuration. On the sine-bar chamber, there is another mounting platform, which is perpendicular to the main chamber base plate, for the monochromator's horizontal diffraction operation configuration. Even though it is currently not used in the conceptual design, the vertical and horizontal reflection geometry can be accommodated without changing the height of the beam on the first crystal.

An alignment port (on the beam exit side) is added asymmetrically to the view port on the beam entrance side, which is defined by the diffracted beam from the first crystal at a certain of energy. Since the first crystal is 2 mm wider than the second, one can perform an initial alignment of the first crystal by moving the entire chamber sideways.

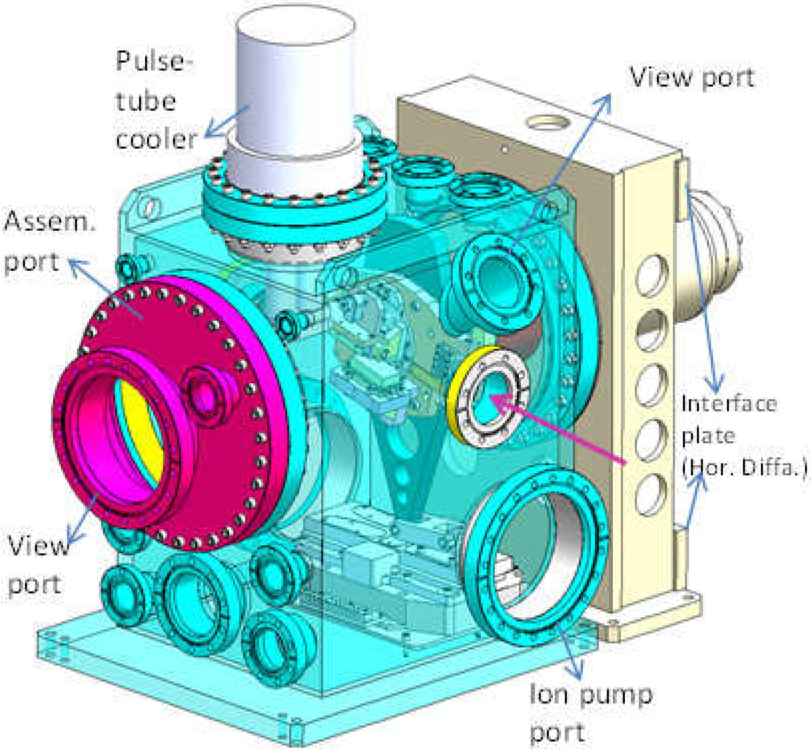

***Figure 83**: Overview of the proposed design*

The interface with the pulse tube cooler will be a CF160 flange (using a Transmit PTS8030 cooler). The rotary valve (vibration source) associated with the pulse tube cooler would be connected to the support table with a simple damping design or to the tunnel wall.

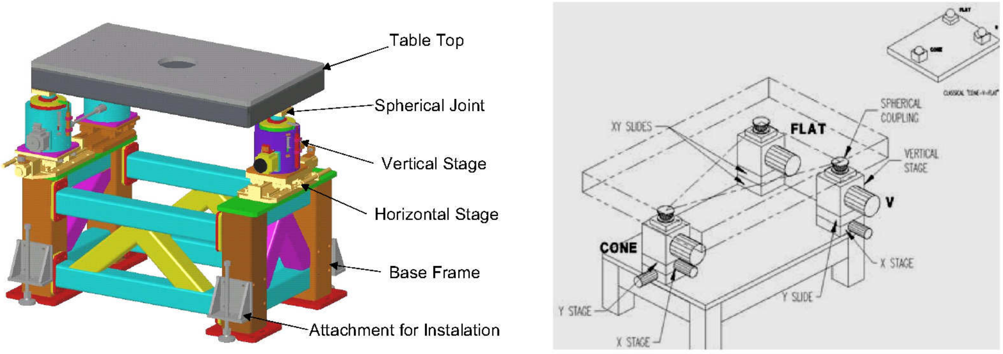

***Figure 84**: Left: 3D model of the support table.* Right: *Working concept [27].*

The APS-designed standard kinematic mounting table (Figure 84) will be used as the base of the monochromator to provide five degrees of freedom for alignment with respect to the beam. The table’s basic precision motion design uses the three-point “cone-flat-V” kinematic mount concept obtained through the use of stepping motor–driven modular linear stages with spring-loaded linear potentiometer encoder and ball-bearing spherical joints as shown in the right side of Figure 84. The cone-flat-V kinematic mount concept has the advantages of three-point stability, free and unconstrained thermal expansion, and good positioning repeatability.

# 6 Vacuum system

## General

In this section, the layout and design of the vacuum beam transport systems are explained.

The vacuum flight tube will be designed to guarantee an average pressure in the overall system of less than $1 \cdot 10^{-6}$ mbar. For constantly evacuating the beamlines, we use ion pumps of the triode type. One advantage of this pump type is that it is also able to pump a small amount of noble gas, which is used for the gas attenuator and some diagnostic elements. The pressure at the ion pumps will be much better than $1 \cdot 10^{-6}$ mbar to ensure their targeted lifetime of 80 000 h. At some locations at the beamline, near mirrors and gratings, we require even better vacuum pressure. Here we use non-evaporable getter (NEG) pumps in addition to the ion pumps. All parts are made of vacuum-compatible materials, mostly stainless steel 304L or 316L; applicable materials are listed in [17]. All the used components pass through a cleaning procedure before installation to eliminate any contamination with hydrocarbons, so that the sum of the partial pressures of masses from mass 45 on to at least mass 100 has to be less than $10^{-3}$ of the total pressure of the cleaned item. More details can be found in the “UHV Guidelines for X-Ray Beam Transport Systems” [17].

The following three figures show an overview of the individual items of the photon vacuum system for each SASE beamline.

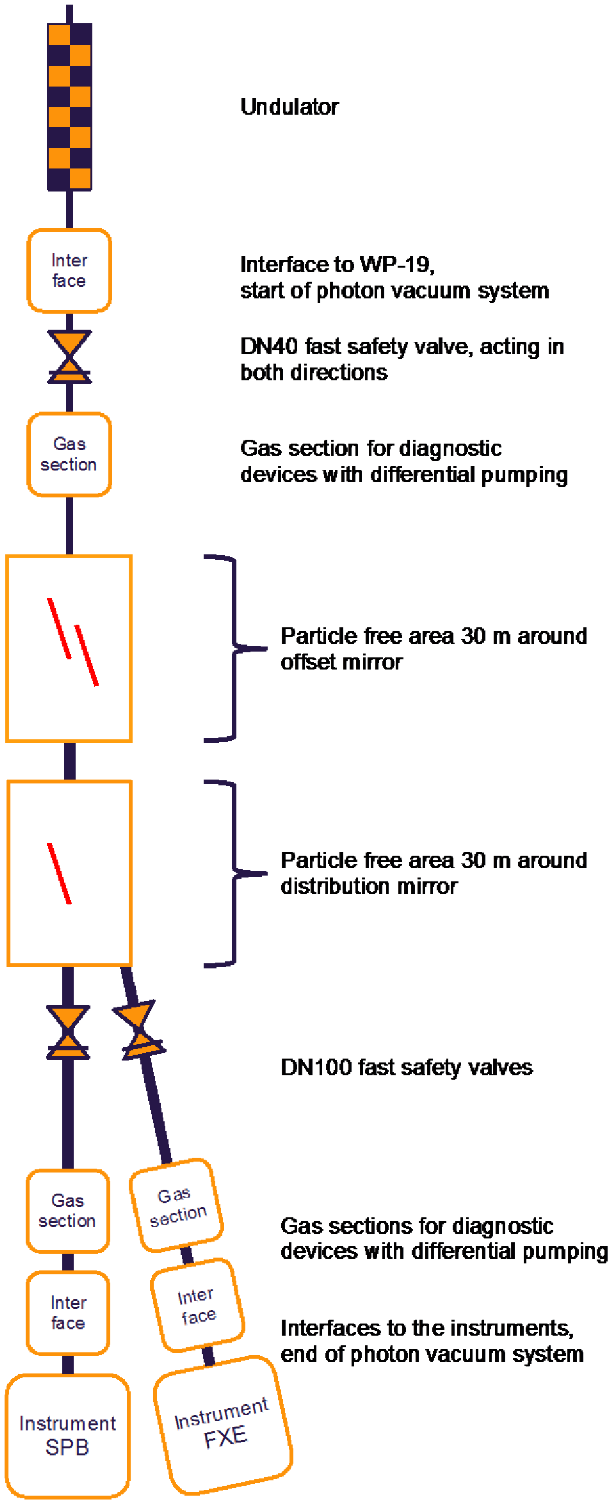

***Figure 85**: SASE1 photon vacuum system*

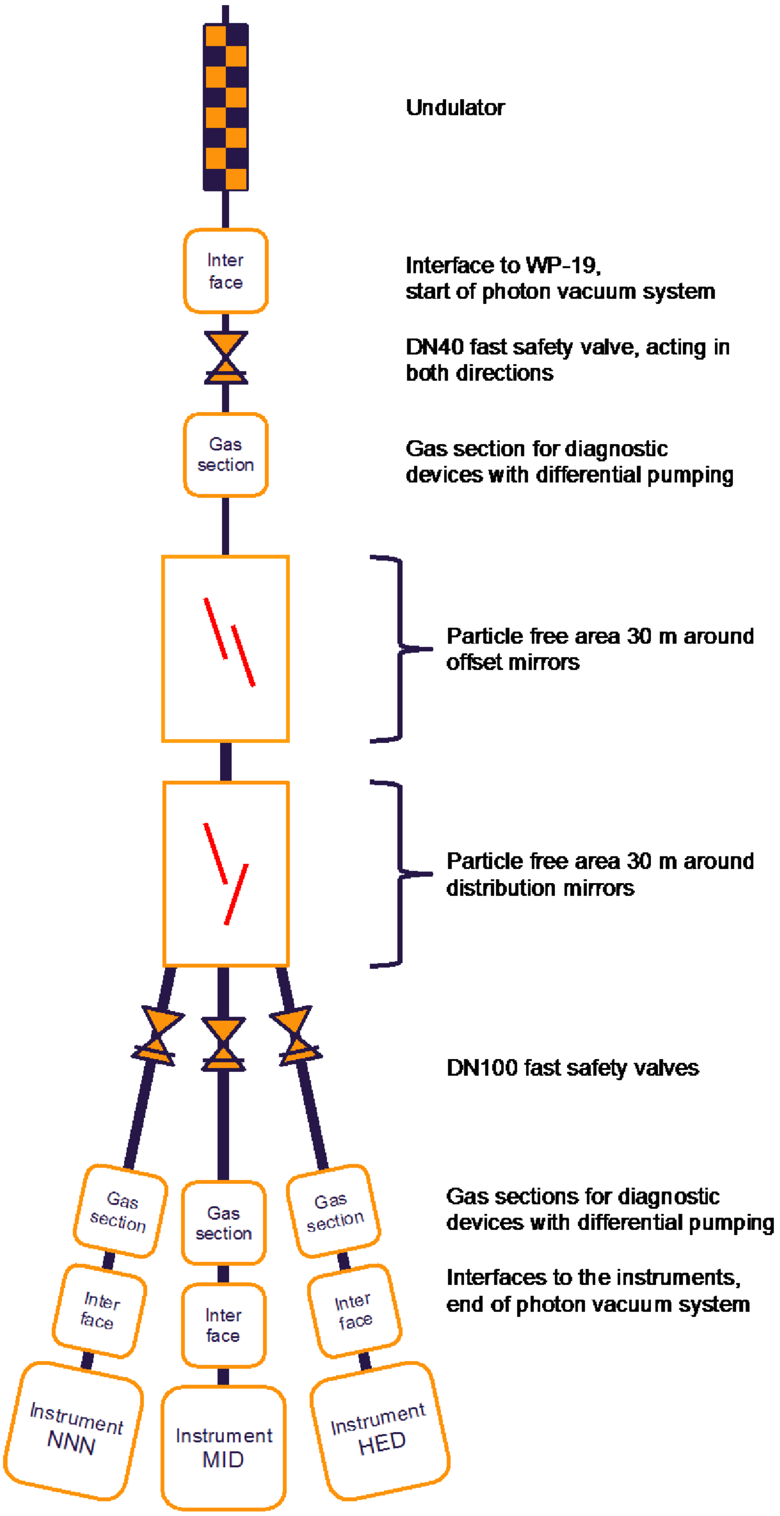

Undulator

Interface to WP-19,
start of photon vacuum system

DN40 fast safety valve, acting in
both directions

Gas section for diagnostic
devices with differential pumping

Particle free area 30 m around
offset mirrors

Particle free area 30 m around
distribution mirrors

DN100 fast safety valves

Gas sections for diagnostic
devices with differential pumping

Interfaces to the instruments,
end of photon vacuum system

***Figure 86**: SASE2 photon vacuum system*

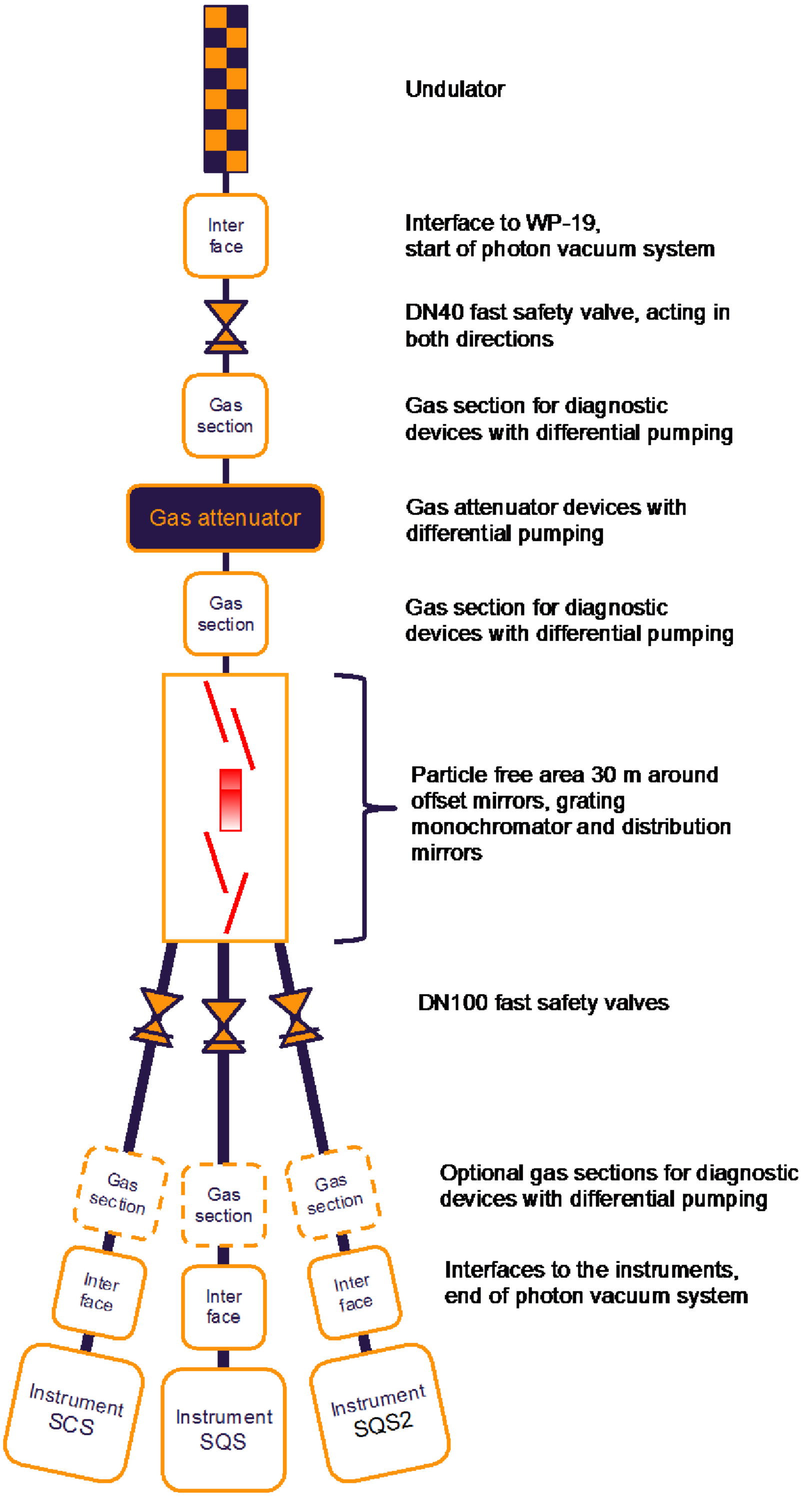

***Figure 87***: *SASE3 photon vacuum system*

# Pump-down

The initial pump-down is carried out by mobile oil-free pump stations, as shown in Figure 88 and Figure 89. These stations consist of a 80 l/s turbomolecular pump and a 10 $m^3$/h scroll pump.

Via a bypass with higher conductance, the scroll pump is pumping down from atmospheric pressure to $10^{-2}$ mbar, where the turbomolecular pump can be switched on to pump down to a pressure level where the ion pumps can be started. The scroll pump run time is reduced using a buffer volume. The pump station has additional ports to attach an optional leak search unit or a residual gas analyser (RGA) for quality acceptance tests.

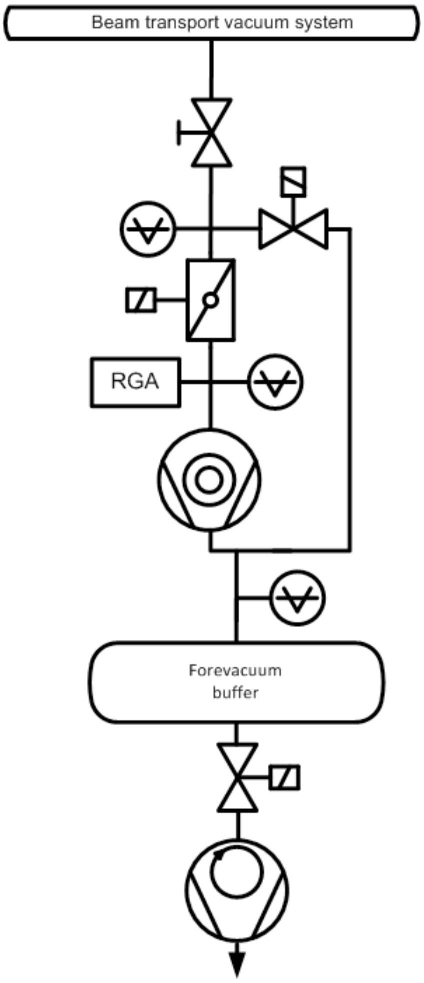

***Figure 88**: Scheme of mobile pump station*

The control software for the pump station runs on a Beckhoff PLC with touch panel. The whole system can be remotely controlled via Ethernet interface.

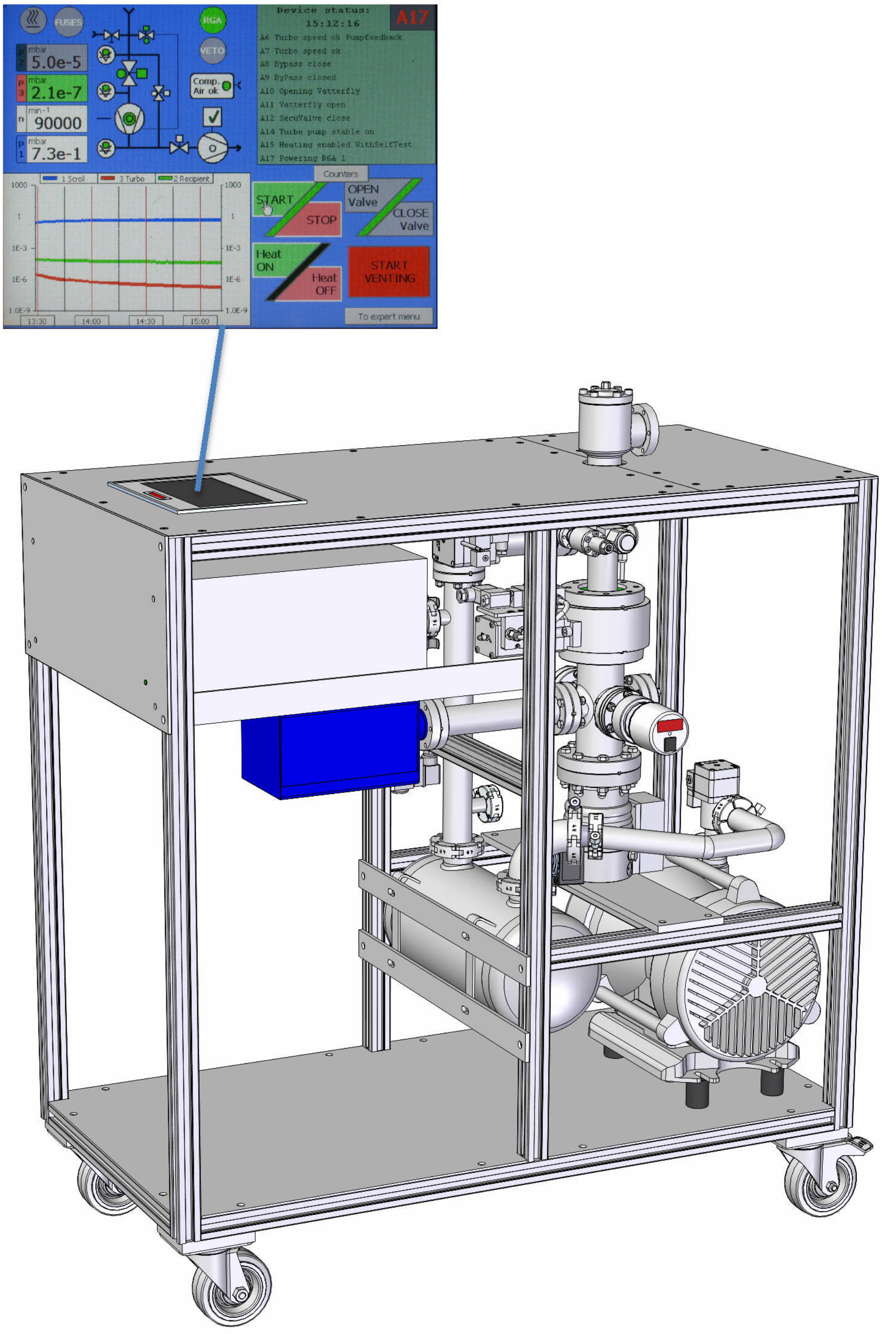

```
Device status:
15:12:16
A6 Turbo speed ok Pumpfeedback
A7 Turbo speed ok
A8 Bypass close
A9 ByPass closed
A10 Opening Vatterfly
A11 Vatterfly open
A12 SecuValve close
A14 Turbo pump stable on
A15 Heating enabled WithSelfTest
A17 Powering RGA 1
```

***Figure 89**: Mobile pump station and control screen*

The operation and control of the rough pumping process are done manually. The exhaust gas from the mobile pump stations will be vented into the tunnels.

Figure 90 shows the timing sequence of the initial pump-down procedure using a mobile pump station connected to a 67 m long DN100 beampipe with an outgassing rate of $10^{-10}$ mbar l $s^{-1}$ $cm^{-2}$. The timing sequence is calculated for the position of highest pressure and relates to the first time the beamline is pumped down. Further pump-downs will be faster, depending on how the vacuum system is vented and handled during maintenance. The pump downtime after a maintenance break can also be reduced by linking more pump stations to the system. Venting the vacuum system will be done using dry nitrogen supplied by 100 l liquid nitrogen dewars and a venting system with overpressure safety valve. The DN16 venting valves that are installed at all beamline vacuum segments are equipped with particle filters to avoid contamination of the vacuum.

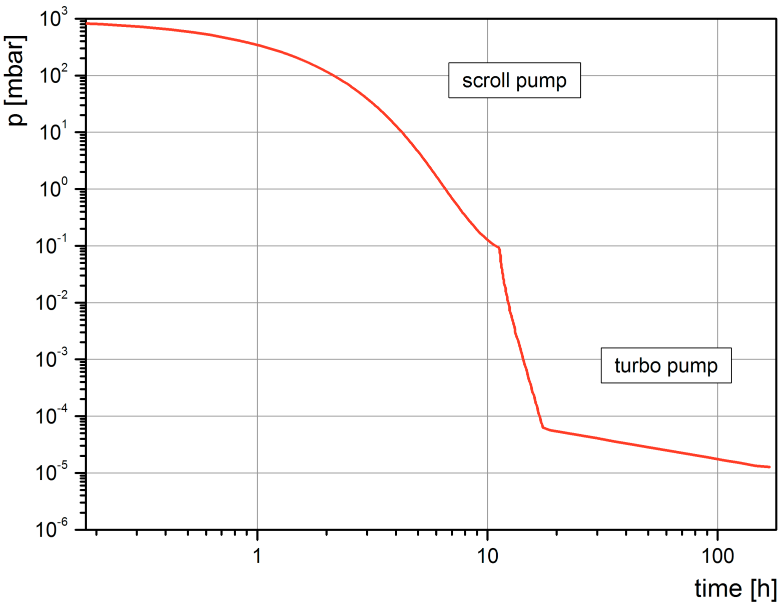

*Figure 90: Pump-down time estimation*

# Layout

The vacuum beamline is divided into segments of maximum 250 m length, which can be separated from the rest of the beamline by gate valves. Each of these segments has a manually operated all-metal DN16 venting valve and at least one manually operated all-metal DN40 rough pumping valve to connect the mobile pump station.

To protect the mirrors and gratings from particle contamination, we introduce a particle-free area 30 m around the sensitive items. For maintenance, this segment can be separated by gate valves. All vacuum parts in the particle-free area will only be handled or assembled in local cleanrooms class ISO 5 [21].

To protect the mirrors and gratings from particle contamination caused by dust that could be present in the rest of the beamline, DN100 fast safety flap valves (VAT, series 75) will be installed upstream the distribution mirrors. In the unlikely event of an air inrush due to a massive leak or a broken vacuum window, these valves close within milliseconds, followed by the closure of the gate valves in the affected branch. This procedure ensures that the mirrors are protected and that only one instrument of the individual beamline is affected, while the other instrument remains operational.

# Mechanical design

The vacuum beam transport system will be designed using all-metal sealed flange connections of knife-edge type (according to ISO/TS 3669-2). All materials used must be UHV-compatible [17].

Valves used to separate vacuum from atmosphere, like rough pumping valves and venting valves, will be all-metal sealed gate valves; valves separating different vacuum segments can be Viton-sealed.

Due to the limited access to the tunnel, the length of a single vacuum pipe is limited to 6 m. In long segments without optical elements, for example downstream of the distribution mirrors, we will apply on-site orbital welding for up to 18 m long pipes to reduce cost, installation work, and the number of potential leaks. The pipe dimensions generally used for the beam transport system are 40 x 1.5 mm for DN40, 63.5 x 2 mm for DN63, and 104 x 2 mm for DN100 pipes. In particular cases, like the beam separation after the distribution mirrors, other pipe diameters or other shapes than round will be used.

To minimize outgassing from drives, motor cabling, etc., and to increase the system reliability, the drives will be placed outside the vacuum wherever it is possible. The motion will be transferred into the vacuum chamber using bellows and magnetically linked or magnetofluid-sealed feedthroughs.

The vacuum pipe supports are a flexible design consisting of a support head holding the pipe, an 80 x 80 mm aluminium profile of variable length to allow different distances between floor and beam axis, and a clamp which will be bolted to the concrete floor, as shown in Figure 91. The supports are adjustable in horizontal and vertical direction to allow easy alignment of the beamline vacuum pipes. Matching the diameters of the different pipes used in the beamline, they are available as loose bearing, fixed bearing, and a combination of both.

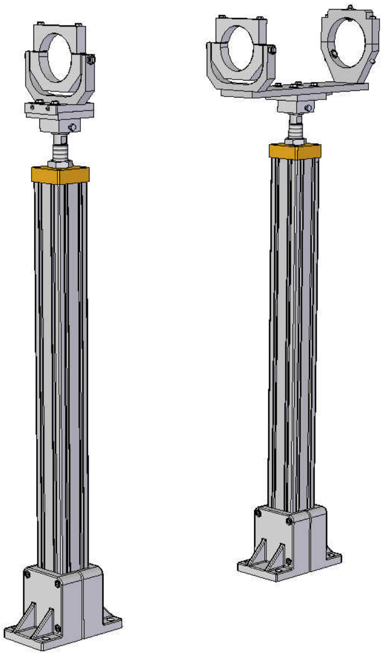

***Figure 91:*** *Different pipe supports*

## Interfaces

The design of the interface to the linear accelerator was specified together with WP19. The interface point will be a DN40 all-metal valve provided by WP19 and controlled by WP73. It will have two sets of limit switches to be read by both control systems. Further downstream, an ion pump and a vacuum gauge from WP19 will be installed, followed by a fast safety valve with one pair of sensors on each side, which closes within milliseconds in case of an air inrush from either side.

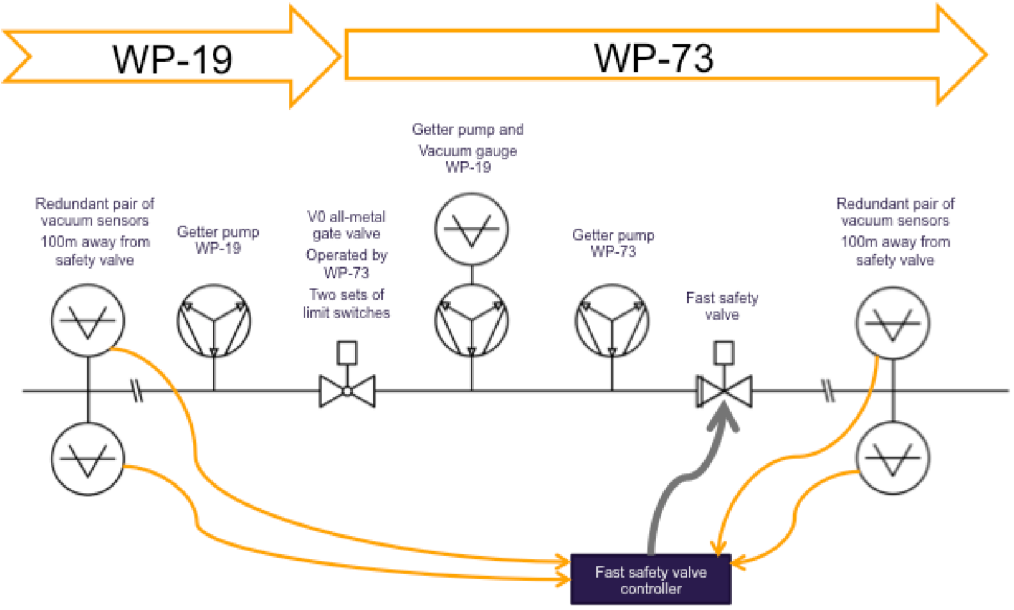

***Figure 92****: Vacuum interface to the linear accelerator*

The interface point to the instruments, as shown in Figure 93, will be a DN40 all-metal valve provided by WP73. Further downstream to the instruments, an ion pump and a full-range vacuum gauge from WP73 will be installed to gather information about the vacuum condition on the instrument side. An aperture surrounded by two ion pumps, acting as a differential pump and an optional RGA, will be mounted upstream the all-metal valve to observe whether the vacuum conditions are impaired by the instruments.

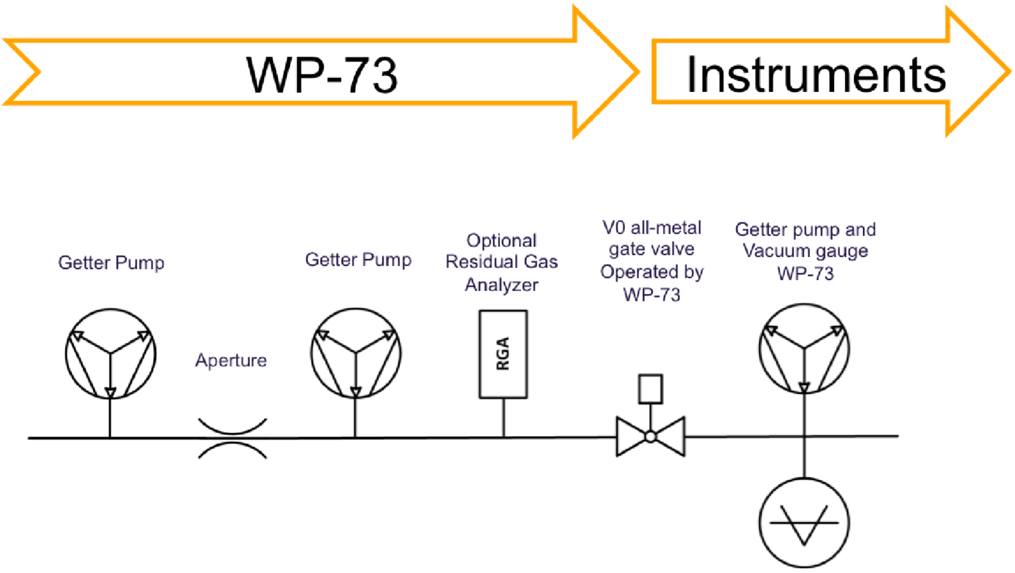

***Figure 93**: Vacuum interface to the instruments*

## Pressure profiles and pump failure analysis

A typical pressure profile for a 240 m long DN100 vacuum segment is shown in Figure 94. The model assumes that the outgassing rate is $10^{-10}$ mbar l $s^{-1}$ $cm^{-2}$ and that both valves at the ends are closed. Every 30 m, a 75 l/s ion pump is connected. The pressure dips at $1.4 \cdot 10^{-7}$ mbar between the parabolically shaped pressure profiles indicate the positions of the ion pumps.

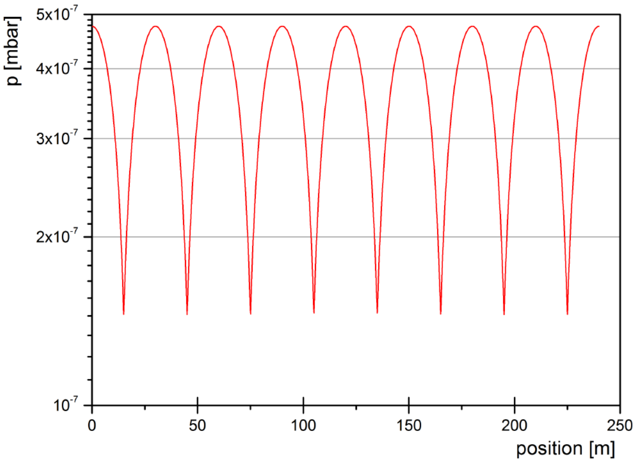

***Figure 94**: Pressure profile along a 240 m DN100 vacuum section*

Studies were carried out about the behaviour of the vacuum system in which one or more ion pumps or ion pump controllers fail. A 240 m long vacuum section, equipped with 75 l/s ion pumps every 30 m, was simulated. The section is made of DN100 stainless-steel pipes with CF flanges and copper gaskets; the assumed outgassing rate from the steel surface is $1 \cdot 10^{-10}$ mbar l $s^{-1}$ $cm^{-2}$. The failure of one to four ion pumps was simulated; the results are shown in Figure 95.

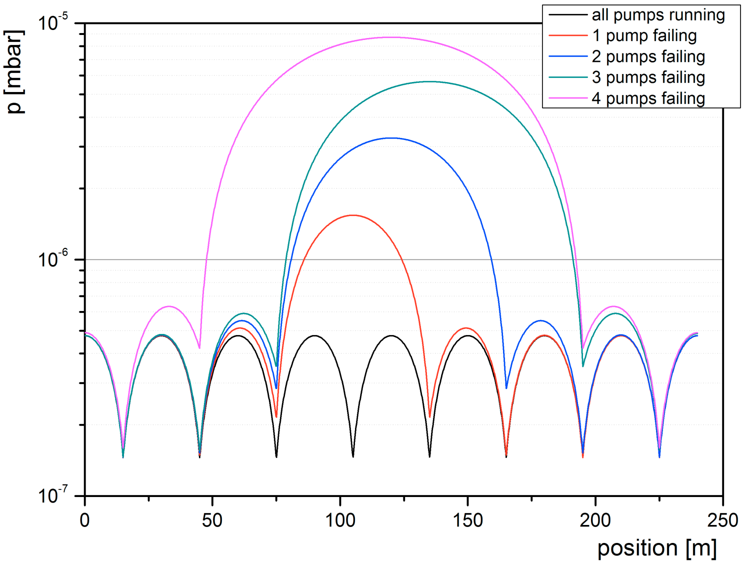

*Figure 95: Failure analysis of ion pumps in a 240 m long section*

The graphs of the pressure profiles show that, in the worst case (four adjacent pumps failing), there is a significant rise in pressure, but that the maximum pressure is still in the $10^{-6}$ mbar range. However, only the pumps adjacent to the failed pumps experience an increase in pressure; their base pressure is still in the $10^{-7}$ mbar range, and the pumps are still operational. The replacement of the affected pumps can be shifted a few months to the next service period. Meanwhile, mobile pump stations can be connected to the beamline to improve the vacuum conditions in the faulty section.

# Gas attenuator at SASE3

To provide for an accurate variation of the beam intensity without modifying the undulator configuration, a device for that purpose has been designed. To eliminate any X-ray optical aberration, a windowless solution is compulsory. This gas-cell attenuator (GCA) will be installed at the SASE3 beamline since it is in the range from 270 eV to 3.5 keV where non-linear experiments of particular interest result.

A reduction of the beam intensity is achieved by introducing a certain pressure of gas into the cell. The attenuation is caused mainly by photoabsortion phenomena, where the Lambert–Beer law is a reasonably good approximation:

$$I = I_0 e^{-\mu\rho d}$$

where $I_0$ is the initial intensity, $I$ is the intensity after the absorption process, $\mu$ is the mass absorption coefficient, $\rho$ is the material density, and $d$ is the considered attenuation path length. Since the system is directly connected to the beamline, two symmetric differential pumping stages are included.

## Design requirements

For the development of the GCA, some important constraints have been taken into account. The maximum attenuation factor for the complete range of energies has been set to $10^3$. Since the pressure inside the active gas cell is directly related to the capabilities of the differential pumping stages, a maximum pressure of 15 mbar has been considered to fulfil the attenuation requirements. The working gas is nitrogen for several reasons: Though it has a relatively small photoabsorption cross section (especially at the higher end of the considered energy range), a relatively high pressure is achievable by the system. In addition, it is an inexpensive gas, so it does not need to be recirculated or recovered.

However, to expand the range of applications of the GCA (i.e. avoiding the “discontinuity” produced by the absorption peak of nitrogen around 400 eV or being able to achieve higher levels of attenuation), some alternative noble gases have also been included in the design process and could be used, provided the infrastructure will be built: Xe, Ne, Kr, and Ar. Table 25 summarizes the main features the GCA device must fulfil.

***Table 25:*** *Summary of GCA main features*

| **Parameter** | **Value** |
|---|---|
| Attenuation path | 15 m |
| Working gas | $N_2$ |
| Working gas pressure range | $10^{-4}$ to 15 mbar |
| Max. attenuation ($I/I_0$) | Up to 3 orders of magnitude |
| Admissible range of beam energy to achieve max. attenuation | 260 eV to 3.5 keV |

However, the use of expensive noble gases makes it desirable to implement a gas recirculation system, which is not planned in the current design.

Another important requirement is the size of the apertures in the differential pumping stages: given the existing relation between the maximum FWHM (mm) vs. $E$ (eV) of the calculated beam width at the experiment station, and including the $4\sigma$ condition plus some additional clearance to absorb possible misalignments, apertures with a diameter of 25 mm have been chosen. Such large apertures are a major challenge for the whole design of the GCA, increasing the cost of the equipment since higher pumping capabilities are required. Nevertheless, it has been foreseen that, in a future upgrade, a discrete variable-aperture system will be compatible with the current design. This is a very interesting option, especially when noble gases (Xe, Ne, etc.) are used, since both the consumption and the throughput of those gases to the rest of the beamline would be reduced dramatically.

For the dimensioning of the specific differential pumping stages used at the GCA, a boundary condition for the pressure of $1 \cdot 10^{-7}$ mbar after the last aperture has been set: the transition upwards and downwards is compliant with the average base pressure of the beamline, with the inclusion of two respective ion pumps after the turbomolecular pumped section.

Finally, one further goal of the design process was to keep the system as robust as possible, protecting from vacuum failures in the beamline and reducing the fabrication and operation costs as much as possible.

## Design and target performance

The mass absorption coefficient $\mu$ (cm$^2$/g) depends on the "impinging" photon energy, and, in the range of interest of the GCA device, it has been demonstrated [22] that the absorption phenomena are dominated mainly by photoabsorption. However, for some elements (H, Be, C, N, and O), Compton (inelastic) scattering is significant at higher energies (above 8 keV).

The mass absorption coefficient is related to the transmitted intensity through a material of density $\rho$ (g/cm$^3$) and thickness $d$ by:

$$I = I_0 e^{-\mu \rho d}$$

Thus, the linear absorption coefficient is $\mu_L$ (cm$^{-1}$) = $\mu\rho$. For a pure material, the mass absorption coefficient is directly related to the total atomic absorption cross section $\sigma_a$ (cm$^2$/atom) by the relation:

$$\mu = \frac{N_A}{A} \sigma_a,$$

where $N_A$ is the Avogadro number, and $A$ is the atomic weight.

Using the tabulated data from [22], one can see in Figure 96 the dependence of the mass absorption coefficient on the beam energy for gases of interest.

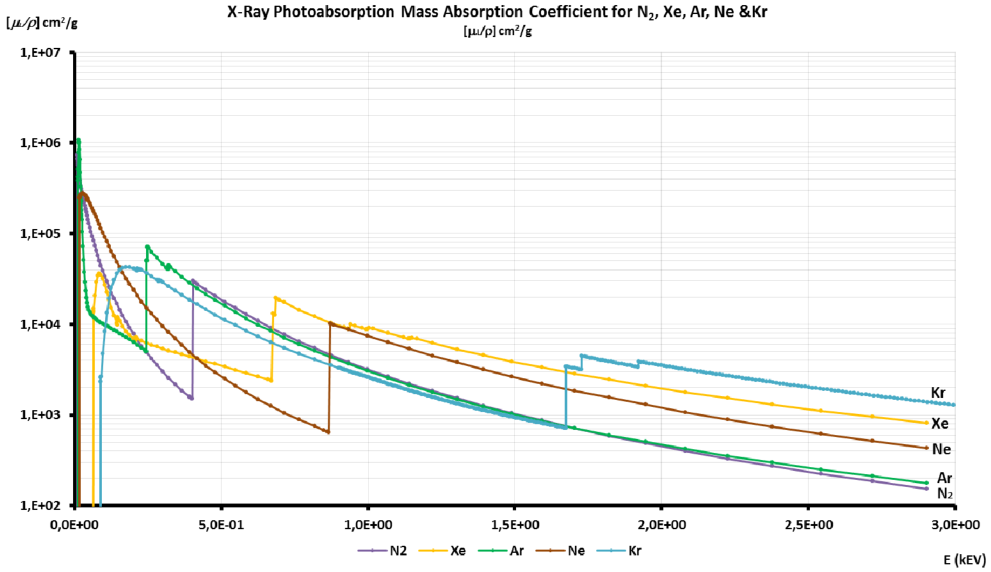

***Figure 96:** X-ray photoabsorption mass absorption coefficient ($\mu/\rho$ in cm$^2$/g) for selected gases*

The active attenuation path length was set to 15 m. This decision was based on the available space in the tunnel in addition to other considerations, such as conductance estimations, required amount of gas, gas flow stability and control, etc. Table 26 shows the range of pressures required to achieve the foreseen level of attenuation for a selected group of gases.

***Table 26:*** *Pressure ranges at different levels of attenuation for a selection of gases*

| | | $P_i(E)$ (mbar) | $I/I_0$ | | |
|---|---|---|---|---|---|
| | | | $1\cdot10^{-3}$ | $1\cdot10^{-2}$ | $1\cdot10^{-1}$ |
| **Gas** | **$N_2$** | $P_{max}$ (2.9 keV) | 26.2 | 17.7 | 8.7 |
| | | $P_{min}$ (0.2 keV) | $5.0\cdot10^{-1}$ | $3.3\cdot10^{-2}$ | $1.7\cdot10^{-2}$ |
| | **Xe** | $P_{max}$ (2.9 keV) | 1.0 | 0.7 | 0.3 |
| | | $P_{min}$ (0.2 keV) | $1.2\cdot10^{-1}$ | $8.2\cdot10^{-2}$ | $4.1\cdot10^{-2}$ |
| | **Ne** | $P_{max}$ (2.9 keV) | 12.8 | 8.5 | 4.3 |
| | | $P_{min}$ (0.2 keV) | $2.3\cdot10^{-1}$ | $1.5\cdot10^{-1}$ | $7.6\cdot10^{-2}$ |
| | **Kr** | $P_{max}$ (2.9 keV) | 3.1 | 2.1 | 1.0 |
| | | $P_{min}$ (0.2 keV) | $5.5\cdot10^{-2}$ | $3.7\cdot10^{-2}$ | $1.8\cdot10^{-2}$ |
| | **Ar** | $P_{max}$ (2.9 keV) | 15.8 | 10.5 | 5.3 |
| | | $P_{min}$ (0.2 keV) | $4.1\cdot10^{-1}$ | $2.9\cdot10^{-1}$ | $1.5\cdot10^{-1}$ |

The differential pumping (in a symmetric configuration) is achieved using a set of four circular apertures of fixed diameter with an initial value of 25 mm. This configuration defines three separate chambers or pumping stages, as shown in Figure 97.

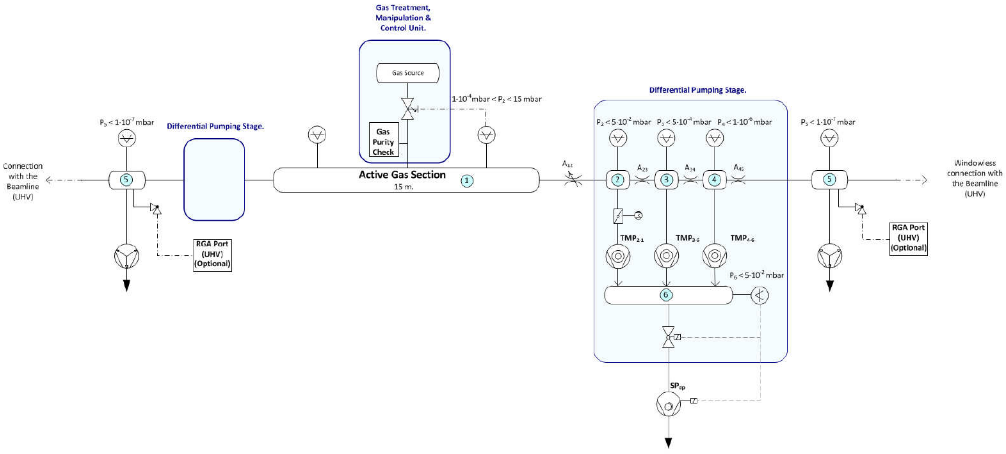

***Figure 97**: Schematic diagram of the GCA setup*

Each stage is connected to a turbomolecular pump with a nominal pumping speed for nitrogen of 1200 l/s at room temperature.

As the first stage can be exposed to an excessive throughput of gas from the gas cell, a throttle valve mechanism has been implemented. This feature has some advantages: It allows the first pump to work protected from any possible damage because of an excessive front pressure. Also, when using a high pressure on the gas cell (i.e. > $1 \cdot 10^{-1}$ mbar) and providing a choke flow condition in the first aperture, a better stabilization on the pressure reduction stages can be provided. Moreover, for those operating modes with molecular-flow condition in the gas cell, the actuation of this throttle mechanism enables a fine-tuning of the pressure in the active gas section.

After each differential pumping setup, an additional triode ion pump of medium size has been included to minimize the throughput of used gas to the rest of the beamline. As an example, it has been estimated that, in the case of using up to 10 mbar of nitrogen in the gas cell, the system can keep a base pressure at the ion pump below $8 \cdot 10^{-8}$ mbar with a gas throughput to the beamline inferior to $5 \cdot 10^{-8}$ mbar·l/s. This value can be dramatically reduced when using other gas alternatives: if a heavier gas, such as xenon, is used for the highest beam energy range, providing its higher mass absorption coefficient combined with a possible reduction in the first aperture size, the current system is theoretically able to reduce this throughput of gas to an almost negligible quantity without losing any feature and with a more-than-probable enhancement of its performance. For this reason, a movable aperture of 10 mm has been foreseen between the first stage and the active gas section. Figure 98 shows a pictorial view of the actual GCA prototype.

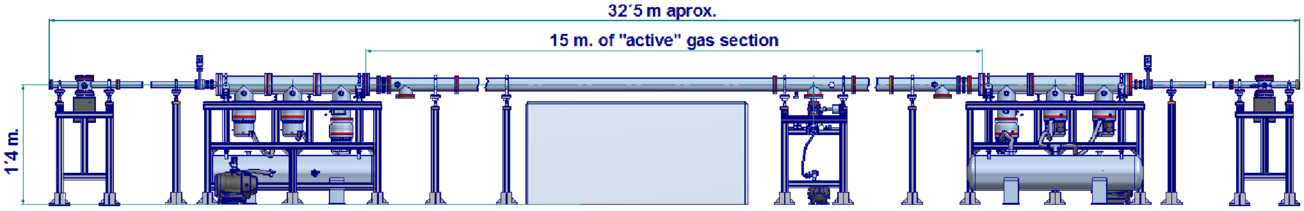

*Figure 98: Pictorial view of the GCA. The movable apertures are not shown here.*

In both cases (25 mm apertures or less), the system is to be protected by redundant safety measures, such as an upstream water-cooled $B_4C$ aperture with a smaller diameter than the ones used in the differential pumping setup. $B_4C$ static apertures in the differential pumping setup and in general are the appropriate safety measures to avoid any catastrophic event in case of misalignment of the beam.

Finally, for the introduction of the gas inside the GCA, a complete gas manipulation and control system has been deployed (see Figure 99). It allows precise control over a large range of throughput rates by means of the sequential operation of up to three mass flow controllers. The current design also makes available a purity check of the gas to be used before introducing it into the GCA, vacuum-assisted cycle purge when changing the working gas, and overpressure protection mechanisms in case of a general failure of the system.

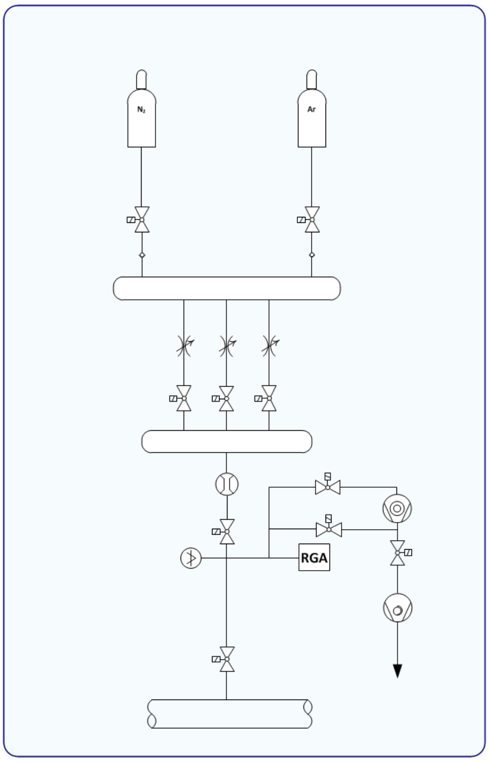

***Figure 99:*** *Schematic diagram of the gas entry, manipulation, and control module setup*

# Differential pumping

Because of the windowless gas-based beam diagnostic devices, a differential pumping before and after those elements is compulsory. Assuming a maximum pressure of noble gas (i.e. xenon) of $5{\cdot}10^{-4}$ mbar, an adaptive differential pumping scheme with up to three stages has been foreseen. In general, it can be compounded of up to two turbomolecular-pumped stages plus an additional triode ion pump stage for a final pressure reduction. Regarding the aperture size, its value will vary according to the biggest beam size in every beamline. In any case, for the above-mentioned maximum noble gas pressure, it is expected that the pressure after the last stage will be smaller than $5{\cdot}10^{-7}$ mbar to be compliant with the general base pressure of the vacuum systems at the European XFEL. However, an additional upstream cryopumping stage may be necessary (i.e. before the first gas-based diagnostic device) if excessive partial pressures of noble gases are found in the area surrounding the accelerator sector.

## Control system

The vacuum control system manages all vacuum-related devices at the beamlines. It operates and monitors the beamline components and protects them from being vented, it archives data, and it generates and sends alarm messages. The control system is connected to the machine protection system to disable linac operation if a vacuum component blocks the beam. A graphical user interface allows straightforward handling. The software is contributed by the DAQ and Control Systems group (WP76).

The following list shows the main components that are operated by the vacuum control system:

- Vacuum pumps (scroll, turbo, getter ion, NEG)
- Vacuum gauges
- Gate valves, fast safety valves
- SASE3 gas attenuator
- Differential pumping units
- Residual gas analysers (RGA)
- Other sensors (temperature, air pressure, cooling water flow)

The control system itself consists of a central industrial PC and several peripheral I/O terminals, distributed in the electronic racks in the tunnels, as shown in Figure 100. The hardware used is produced by the company Beckhoff Automation GmbH, Germany. The components in the individual racks are linked by the EtherCAT bus system via copper cables or fibre optical connections in a ring topology to obtain a redundant connection.

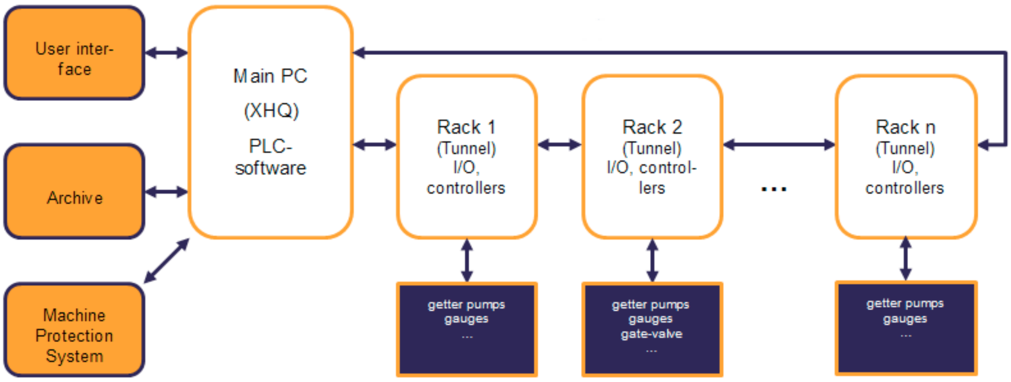

***Figure 100**: Concept of the vacuum control system*

# 7 Further beamline components

## Apertures

To separate the FEL beam from the non-lasing part of the undulator spectrum, spontaneous radiation apertures (SRAs) were presented conceptually in CDR2011. In the meantime, a prototype was developed (Figure 101) and produced (Figure 102). The blades consist of tungsten blocks, which are protected by $B_4C$ blocks. This assembly is water-cooled and held together by a spring mechanism (Figure 103). The technical specifications can be found in EDMS under D*2022671.

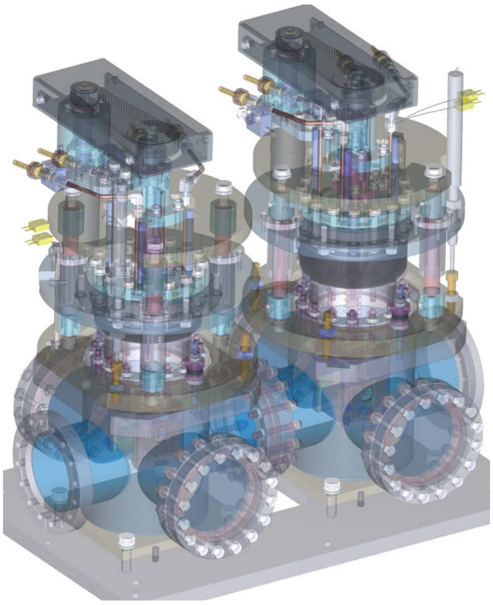

***Figure 101**: Design of SRA prototypes (by Alca Technology Srl)*

An in-vacuum test of the cooling efficiency of the SRAs was performed [29]. Using an aluminium dummy block with a heater installed, 250 W of heating power was applied for 30 min. At an inlet water temperature of 6.5°C and a water flow of 7 l/min, the water outlet temperature was 28.4°C. With a cooling water temperature in the European XFEL photon tunnels of 22°C, the exit water temperature should still remain below 50°C, even if the full beam load hits a single blade.

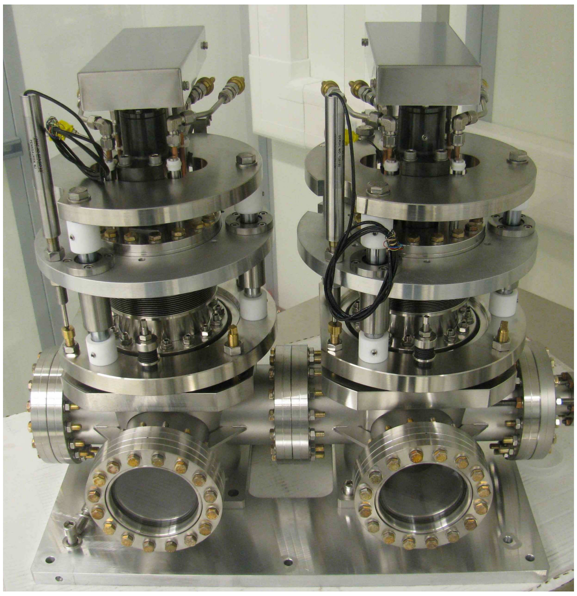

*Figure 102: SRA prototypes*

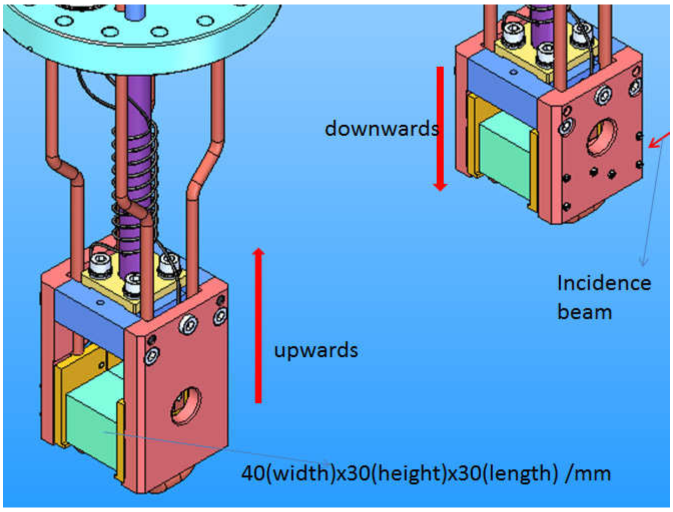

***Figure 103:** Clamping mechanism for $B_4C$ and tungsten blocks. The $B_4C$ block will be tilted by 4–8° where it touches the beam in order to increase the damage tolerance.*

A service stand was built that allows the testing of the SRAs in horizontal and vertical geometry and allows the changing of the $B_4C$ and tungsten blades (Figure 104).

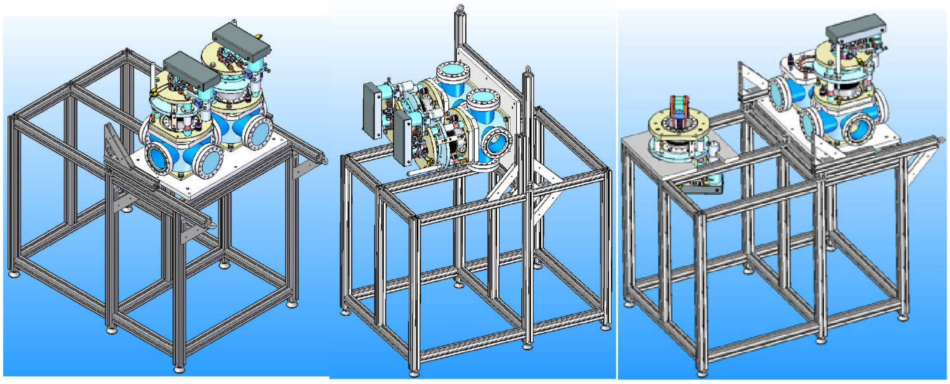

***Figure 104:*** *Test and service stand for SRAs*

The $B_4C$ blades are shown in Figure 105. They were polished to a roughness of 0.04 µm and a maximum PV height of 0.2 µm.

In order to use the SRAs also as beam loss monitors (operation principle similar to Figure 11), the surfaces exposed to the beam have to be coated with a diamond layer; an optical mirror inside the vacuum can direct the fluorescence light through the window flanges at the sides.

A design similar to that of the SRAs could be used as beam-defining slits and beam loss monitors in front of each mirror. In this case, the tungsten block is not needed and the $B_4C$ block could be made longer in order to allow a shallower incidence angle. As seen in the ray-tracing plots, the horizontal beam-defining slits need to have a larger stroke (60 mm) than the SRAs. For the vertical exit slits of the SASE3 grating monochromator, the SRA design could be used as well. In this case, the precision of the motion, reproducibility, and edge quality of 1 µm have to be achieved.

Further tests of the UHV conditions and the motion system of the SRA prototype are under way.

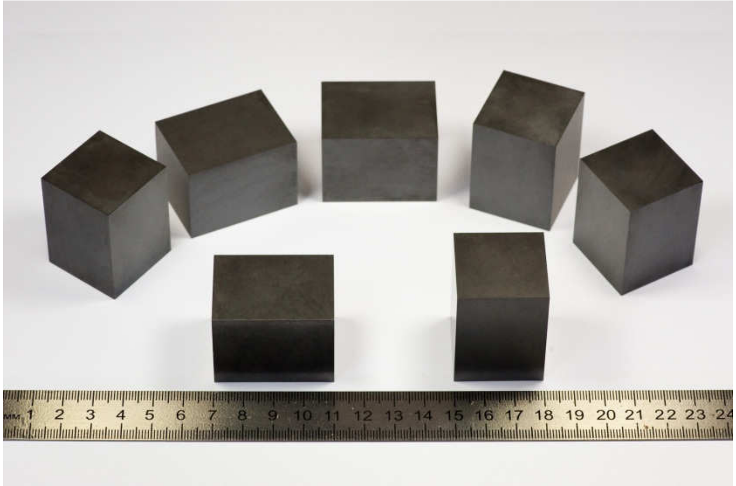

*Figure 105*: *$B_4C$ blades ($40 \times 30 \times 30$ mm$^3$) for the SRAs are produced by TISNCM [30] with hot-pressing method.*

# Front ends and shutters

Concerning the front ends, a design similar to the PETRA III design can be chosen since the radiation-shielding requirements for the spontaneous radiation lead to comparable thicknesses of tungsten and lead. Also the concept of burn-through absorbers will be applied. A schematic of a front end towards the experiment hall is shown in Figure 106. The differences to the PETRA III design are the $B_4C$ aperture and the power absorber (Figure 107), which is made to withstand the FEL power up to Mode 3 operation. In Mode 4 (full-beam) operation, the machine has to be switched back to Mode 3 before the shutter is closed (another option would be to open the undulator). Also, the $B_4C$ power absorber must always be closed before the tungsten shutter, which alone would not be able to withstand the FEL beam. This closing and opening sequence has to be implemented and controlled by the personnel interlock system (WP38).

The design of the tungsten shutter (Figure 108) will be identical to the PETRA III design, except that the thickness of the tungsten (in the figure, 200 mm) will be adapted to the equivalent tungsten thickness of the concrete labyrinth walls towards the experiment hall (around 80 mm) and the labyrinths in the shaft buildings (200 mm or less).

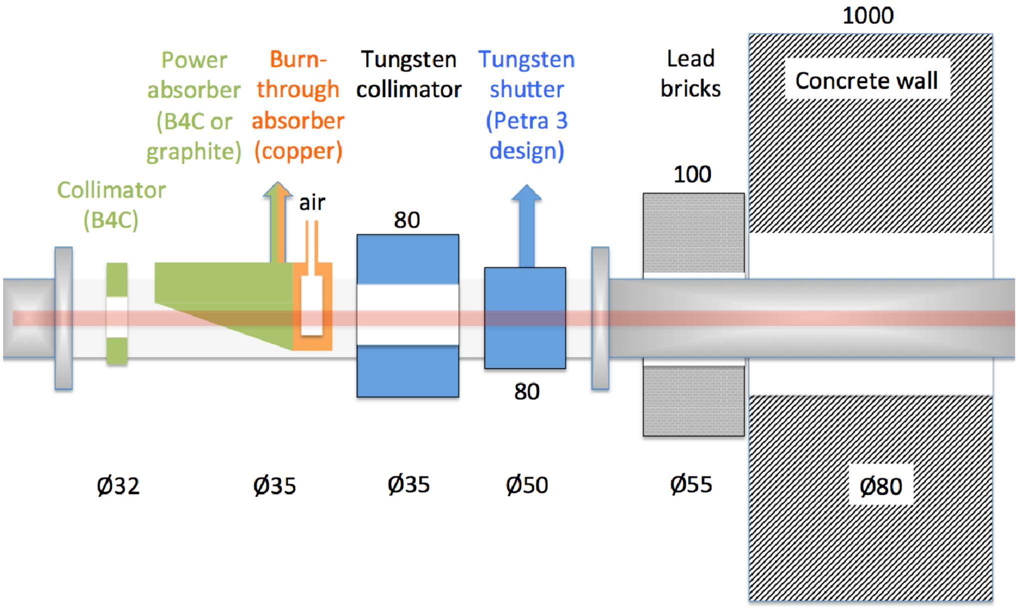

***Figure 106:*** *Schematic front-end design for transition from photon tunnels to experiment hall*

The horizontal aperture of the front end in the shaft building XS3 (SASE1 before photon tunnel) has to be wider than shown in Figure 106**.** Because the beam deflected after the two offset mirrors has a variable offset, a clear aperture of 60 mm is required (see ray-tracing plots for SASE1 in Appendix A).

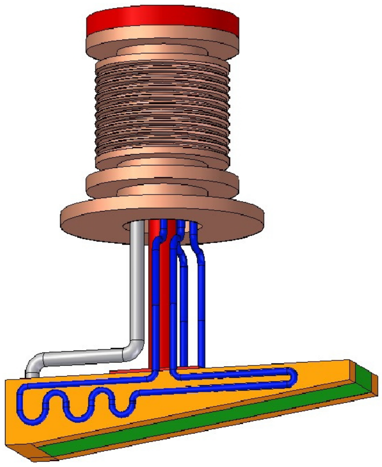

***Figure 107:*** *Conceptual sketch for a beam power absorber. The beam comes from the right and hits the $B_4C$ surface at 8° grazing incidence. The $B_4C$ is cooled from its sides with copper bars, which are either welded or clamped to the $B_4C$. At the back is a copper piece with an air volume connected to the outside air, which functions as a burn-through absorber.*

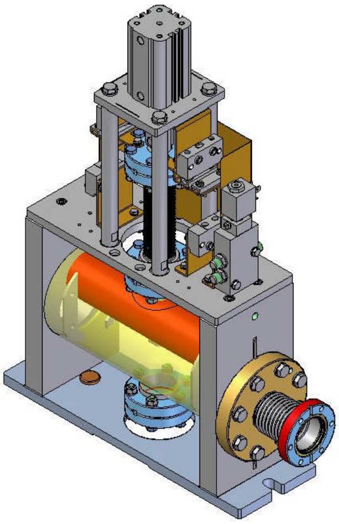

***Figure 108:*** *Tungsten (densimet) shutter design by DESY FS-BT*

## Solid attenuators, Be CRLs

In the hard X-ray beamlines SASE1 and SASE2, solid attenuators will be positioned in front of the offset mirrors. Their main purpose is for commissioning and alignment because it can be expected that the attenuators will create intensity distortions in the beam profile downstream in the experiment hall. The attenuators will consist of 8–10 insertable water-cooled carbon pieces of different thickness between 75 µm and 20 mm. A possible distribution of thicknesses and materials is shown in Table 27**.**

With such a selection of attenuators, one can realize attenuation steps of 10 and 100 for energies between 3 and 24 keV. The single-crystal diamonds, which typically have a size of only 5 mm, can be embedded into a CVD matrix as shown in Figure 109.

The mechanical design has to satisfy particle-free UHV conditions, since it is close to the offset mirrors. Also, an elevated radiation background from Compton scattering at the attenuators can be expected.

*Table 27: Thicknesses and materials of the solid attenuators*

| Thickness [mm] | Material | Diameter [mm] |
|---|---|---|
| 20 | Graphite | 30 |
| 10 | Graphite | 30 |
| 5 | CVD polycryst. diamond | 30 |
| 2.5 | CVD polycryst. diamond | 30 |
| 1.25 | CVD polycryst. diamond | 30 |
| 0.6 | CVD single cryst. | 5 + CVD matrix diam. 30 |
| 0.3 | CVD single cryst. | 5 + CVD matrix diam. 30 |
| 0.150 | CVD single cryst. | 30 |
| 0.075 | CVD single cryst. | 30 |

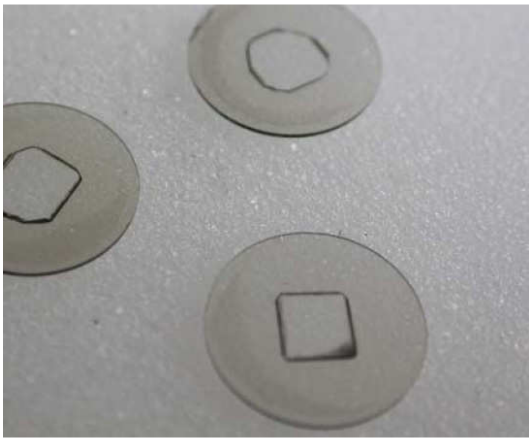

***Figure 109:*** *Single-crystal diamonds embedded in a polycrystalline matrix (produced by Diamond Materials GmbH, Freiburg, with HPHT2-type crystals from Element Six)*

The attenuators will not be able to withstand full pulse train operation in beam Mode 4, but rather define, together with the $B_4C$ apertures, the conditions of beam Mode 3. Therefore, the actuators have to be interlocked to the equipment protection system.

Downstream of the solid attenuators, ports for beryllium compound refractive lenses (CRLs) are foreseen. The agreement with the FXE and MID instruments is that the UHV vessel and actuators will be the responsibility of WP73, while the CRLs themselves have to be chosen and procured by the instrument groups. The CRLs are used to collimate or slightly focus the beam, so that cutoff effects at the distribution mirrors can be avoided and the beam size at the experiments can be controlled also in the vertical plane.

Without the use of CRLs, the second adaptive offset mirror can be used to collimate or focus the beam; however, this leads to an astigmatism, which is undesirable if microfocusing is also done by rotationally symmetric CRLs, as in the FXE and MID instruments (see the corresponding instrument CDRs and TDRs). The effects of wavefront distortions from CRLs at large distances are subject of current experiments and simulations.

The mechanical design of the CRL chamber can be very close to existing designs for synchrotron radiation. All lenses need to be water-cooled and $B_4C$ apertures have to be included in the mounting scheme so that no metal can be hit directly by the FEL beam.

# Diagnostics

Several kinds of diagnostic devices are developed by the X-ray Photon Diagnostics group (WP74) and placed in the beam transport system. These are in particular:

- Gas-based beam intensity monitors (XGMDs)
- Gas-based beam position monitors (XBPMs)
- Gas-based photoemission spectrometers (PES) for spectral analysis
- Pop-in monitors and imagers for alignment and general beam diagnostics
- *K* monochromators for undulator tuning
- Micro-channel plate (MCP) detectors

The gas-based devices run typically with a Xe pressure of $1 \cdot 10^{-4}$–$5 \cdot 10^{-4}$ mbar and require differential pump stations to interface with the UHV vacuum of the beam transport. Therefore, the gas-based devices are placed at sections of the beam transport where the beam positions change not too much: either before the offset mirrors or at the end of the photon tunnels.

The PES might require different choices of gases, depending on the target energy range. Currently R&D activities in WP74 are ongoing that explore the usable parameter space of these devices.

The pop-in monitors and imagers work typically on a 10 Hz basis (Mode 1) since different scintillators are used and water cooling will most likely not be implemented.

The *K* monochromators are silicon channel-cuts that are used to calibrate the gap (*K* value) of individual undulator segments. Since the measurement method requires seeing a cone of the spontaneous radiation, a large beam aperture is desired for these devices. At SASE3, the tuning will be done at higher harmonics of the undulator.

The MCP detectors are situated behind the offset mirrors and are able to see either the direct beam or the beam deflected by one or two offset mirrors. Their main purpose is to provide accurate relative intensity information during the SASE tuning; however, they might also be useful for other diagnostic tasks like monitoring the reflectivity and diffuse scattering from the offset mirrors. The MCPs can be damaged even in single-pulse operation for high pulse energies. Therefore, special care has to be taken during the operation of these devices.

An overview of the diagnostic devices being developed by WP74 is found in:

- CDR: Framework for X-ray Photon Diagnostics at the European XFEL (EDMS D*2851121)
- CDR: The European XFEL Undulator Commissioning Spectrometer (K-mono) (EDMS D*1940181)
- CDR of MCP based detector (EDMS D*2850921)

Further information is posted on the WP74 documents website:

www.xfel.eu/project/organization/work_packages/wp_74/documents

# 8 CAD integration

To identify collisions with tunnel walls and infrastructure installations, simplified placeholder models are generated for all parts of the beam transport systems and placed in a facility-wide CAD model. This is divided into “CAD rooms” to keep the amount of elements in each model manageable (Figure 110).

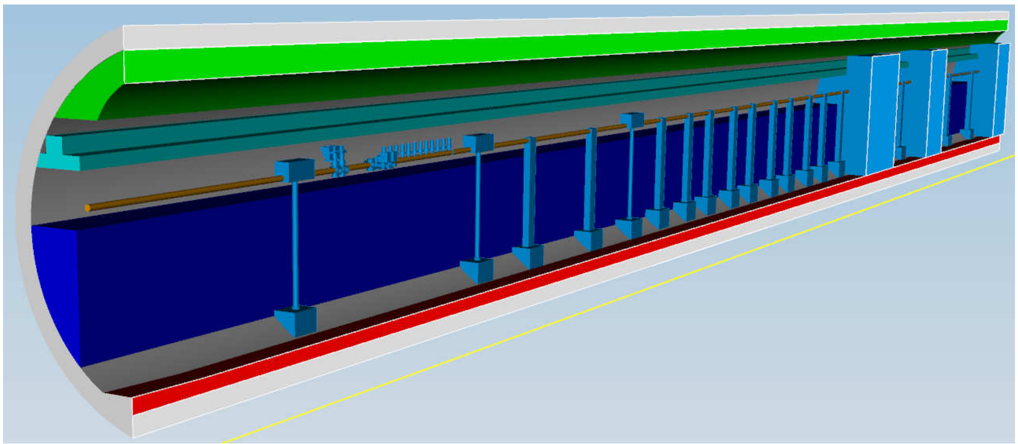

***Figure 110:*** *CAD integration model XDT2, Room 9*

Several CAD rooms can be looked at together and virtual walk-throughs, cuts, and measurements are also possible with a viewer program. Coordinates for each CAD room are available in the “BO-Liste” (EDMS D*496900) and linked to the two coordinate systems for the European XFEL, the LA and the PD system (EDMS D*497635).

The placeholder models in the CAD rooms for the photon transport systems are updated every six months and relate to the component list, which is updated at the same time (EDMS D*2278111). A description of the CAD integration process for the photon beamlines can be found at www.xfel.eu/publications. The facility-wide CAD model is managed by DESY IPP, and collisions are checked on a regular base.

# 9 Installation schedule

The top-level milestones of the project are posted on the European XFEL website under www.xfel.eu/project/construction_milestones. The current milestones relevant for the beam transport system are listed below.

| Date | Milestone |
|---|---|
| 30 June 2015 | Linac tunnel closed |
| 31 August 2015 | SASE1 instruments ready for beam |
| 30 September 2015 | First beam to XS1 dump |
| 30 September 2015 | XTDs 2, 4, 9, and 10 closed (SASE1 and SASE3 tunnels) |
| 15 October 2015 | Beam to XSDU2 |
| 15 December 2015 | First lasing SASE1 possible |
| 31 December 2015 | XTDs 1, 3, 5, 6, 7,and 8 closed (SASE2 tunnels) |
| 15 January 2016 | Beam to XSDU1 |
| 31 January 2016 | First lasing SASE3 possible, instrument ready |
| 31 March 2016 | Start of user operation |
| 31 July 2016 | All beamlines in user operation |
| December 2017 | Extended beam delivery (full performance) |

The installation of the photon beamlines follows the installation of water and electricity in the tunnels and should start at the beginning of 2014 with the XTD2 tunnel (SASE1) according to the actual planning. The last tunnel (XTD6, SASE2) is accessible for beam transport installation in spring 2015. According to the top-level milestones, 6–20 months for beam transport installations are available for each tunnel. The installation will be done by the WP73 vacuum team in collaboration with contractors and the DESY groups responsible for transportation (WP33), survey and alignment (WP32), and infrastructure (WP34). In 2013, most items required for the tunnel installation, as well as the long-lead items (mirror substrates) will have to be ordered. Also, decisions based on prototyping should be made in the first half of 2013. A more detailed project plan is shown in Appendix C.

# 10 Summary and outlook

The issues we consider the most critical today for the beam transport systems are the performance and availability of sufficiently good mirrors and gratings for the photon distribution system and the soft X-ray monochromator, including the necessary cooling. Apart from that, stability with respect to vibrations, thermal drifts, and heat load effects are important for mirrors and monochromators, due to the lengths of the beam transport systems and to the pulsed beam load. Another big organizational challenge is the implementation of the 2.5 km long vacuum system and its build-up in the tunnels.

Besides these “known problems”, there are issues that are difficult to assess today: What will be the side effects of the powerful pulse trains to the coatings of optics, like fatigue, carbon or other depositions on mirrors? What kinds of vibrations do the pulse trains induce? Will the accelerator run stably enough to allow thermal equilibration of mirrors and monochromators to achieve the performances we calculate? How will the beam typically be used by the experiments and in which scientific directions will the availability of high-repetition rate X-ray FELs lead? And finally: In which directions will FEL technology go with seeding, after-burner technology, and polarization control?

Right in between falls the questions of operating conditions, which we tried to address in Chapter 2, “Operation and safety”. The multi-user operation of the European XFEL adds complexity, compared to single-user FELs or storage rings, and will lead to crosstalk between experiments during scheduling and operation. The goal of further detailed design of the beam transport systems should be *not* to add to this complexity by defining more beam modes, but to choose a design that fits into the already defined envelopes of Mode 3 and 4 operation. Here, the concept of beam loss monitors might help to *reduce* the usage of beam modes, if it can be implemented successfully and reliably in the early commissioning and operation phase, so that the beam transport can as much as possible run in Mode 4 conditions.

# A Ray-tracing plots

Ray-tracing plots for the beam transport systems SASE1, SASE2, and SASE3 and each port are shown in the horizontal and vertical geometry on the next 12 pages. Certain apertures and dimensions are likely to change in the technical discussions leading towards a mechanical design of the beam transport systems: the apertures for the differential pumping units and the gas absorber are going to be reduced as much as possible in order to keep the gas flows low. As discussed in the section on the gas attenuator, reduced apertures that move in and out of the beam are possible, or fixed apertures that move together with XBPMs and XGMDs in the gas diagnostics sections in order to ensure optimal performance of these devices.

The apertures important for radiation safety (shown in black) can only be changed in agreement with the radiation safety group at DESY.

PDF files and Word documents for the current ray-tracing plots can be downloaded from EDMS D*3004861.

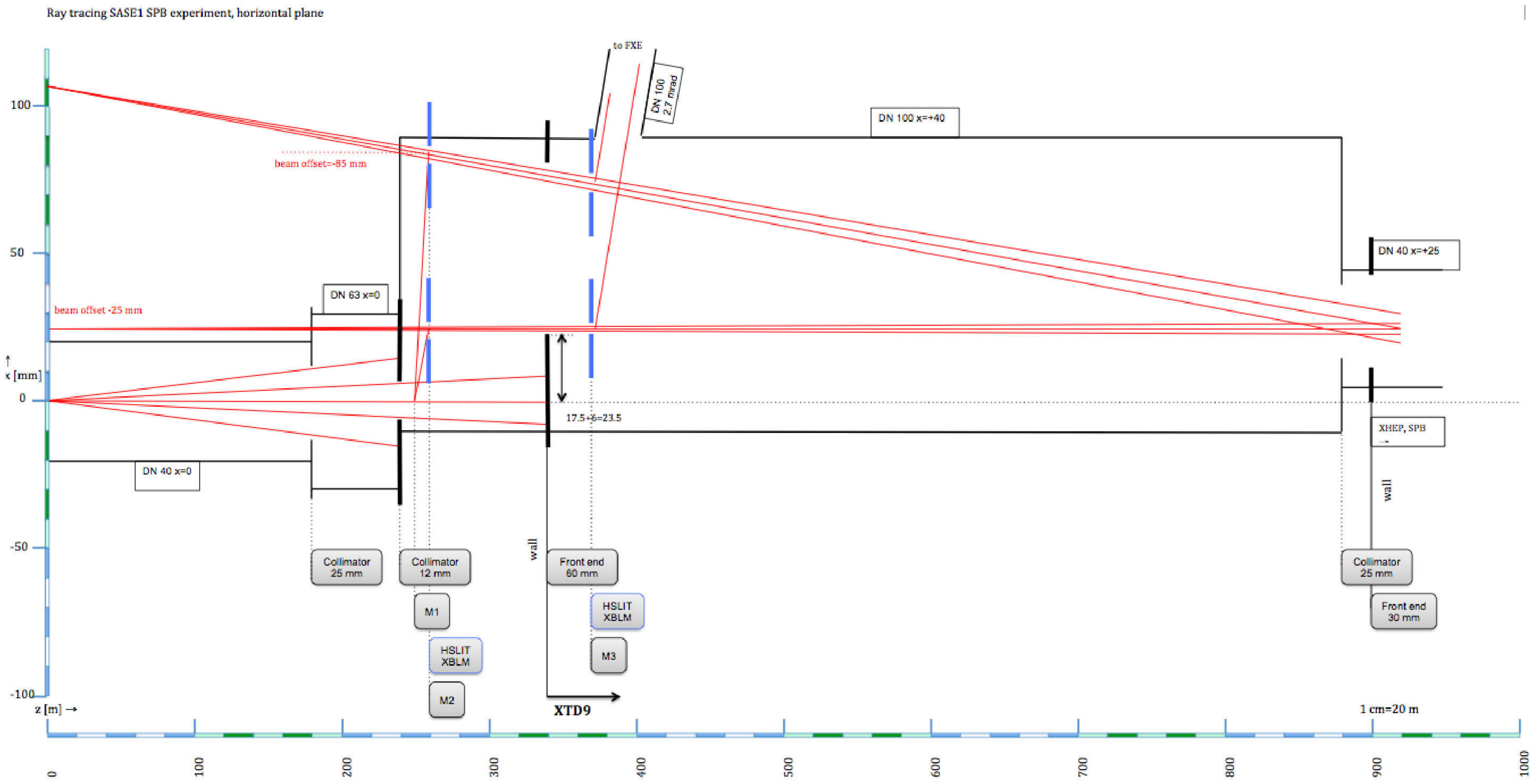

*Figure 111: Ray tracing for SASE1, SPB experiment (horizontal plane)*

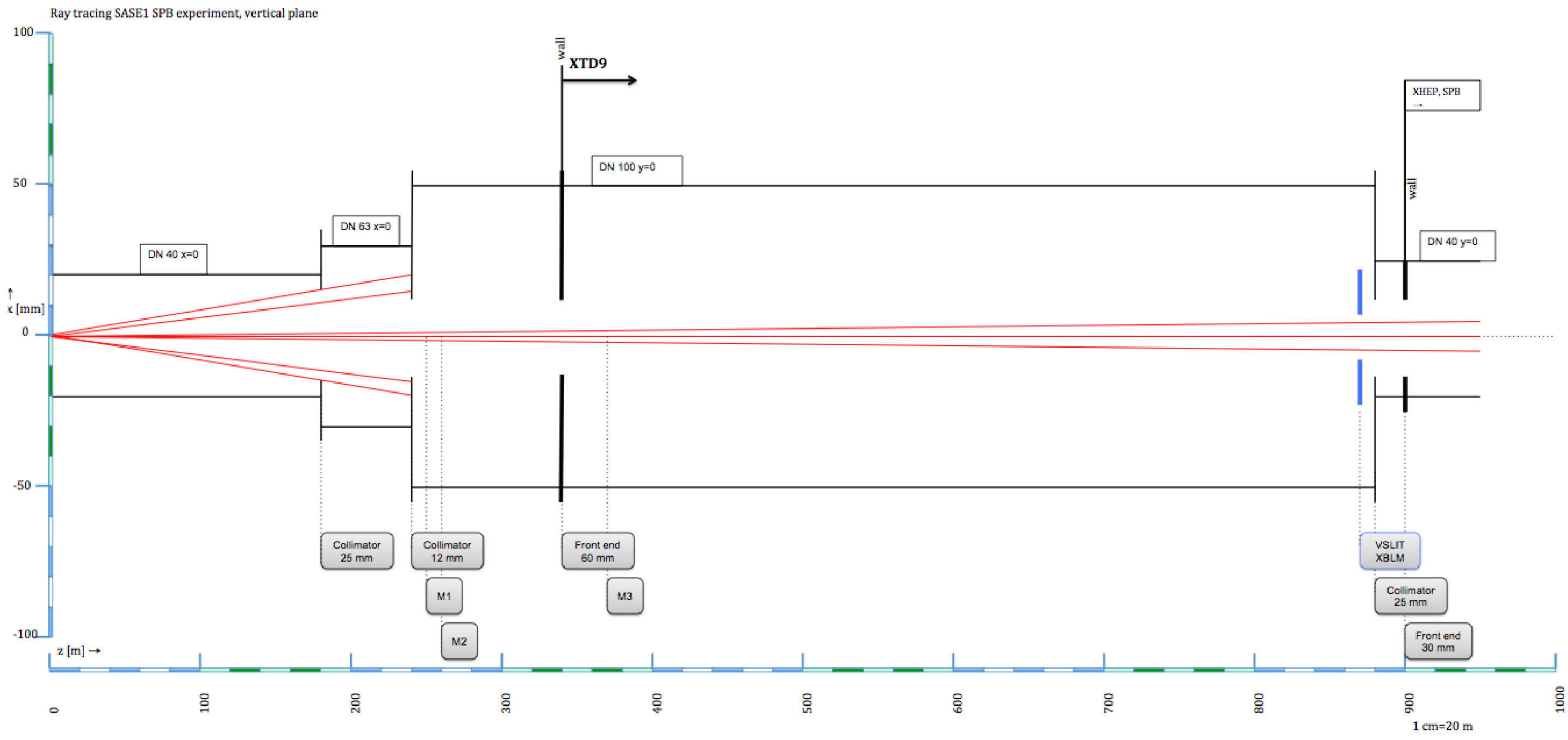

***Figure 112:*** *Ray tracing for SASE1, SPB experiment (vertical plane)*

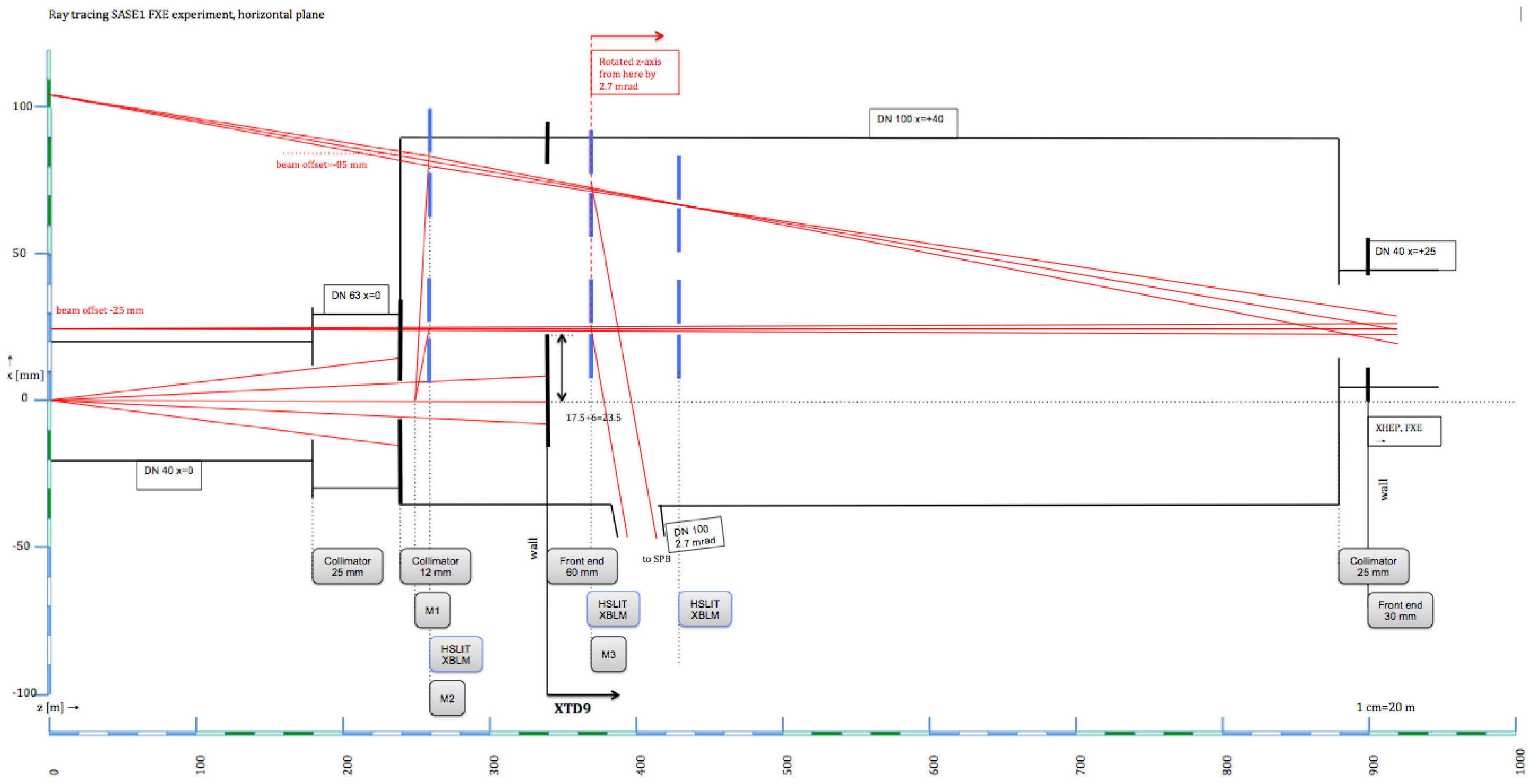

***Figure 113:*** *Ray tracing for SASE1, FXE experiment (horizontal plane)*

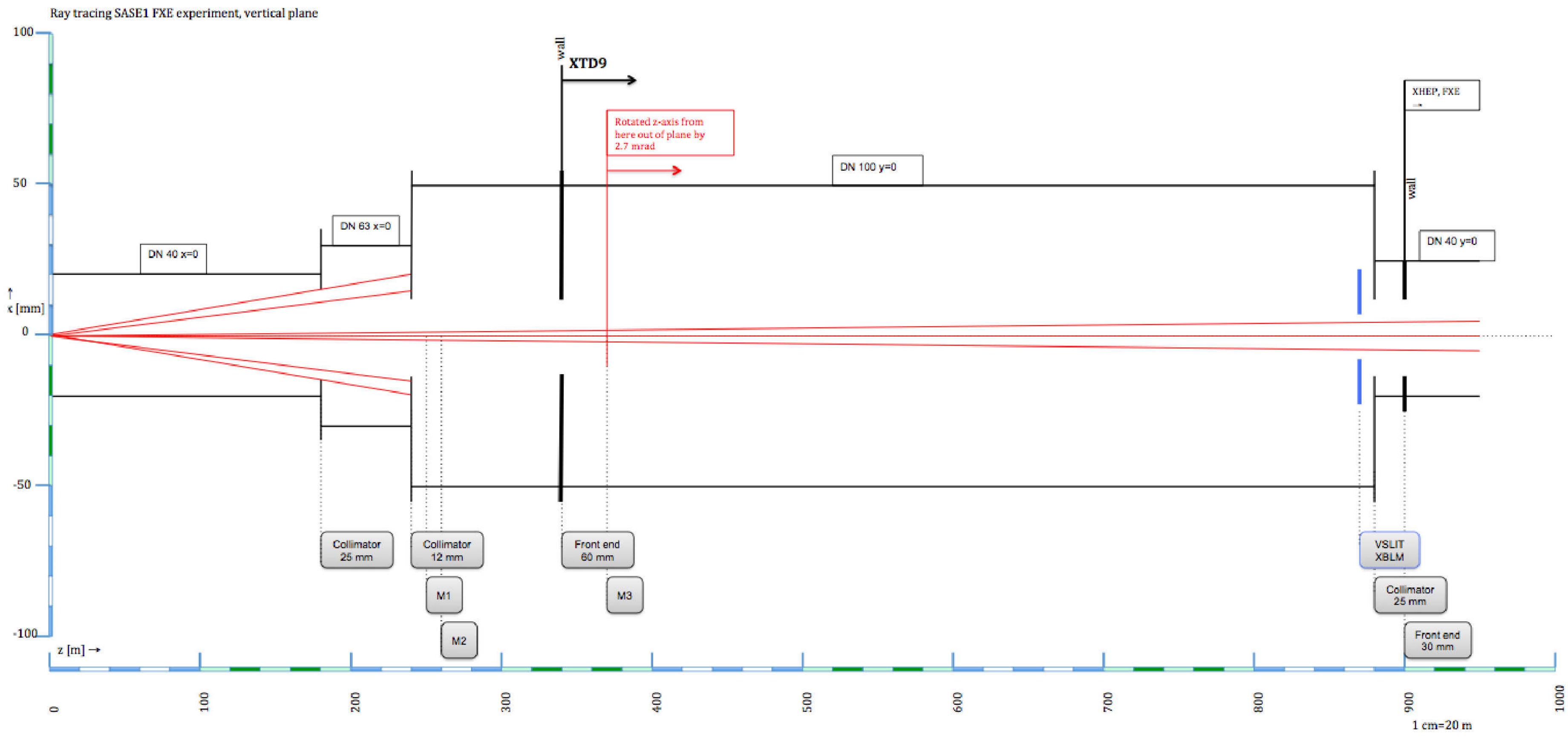

*Figure 114: Ray tracing for SASE1, FXE experiment (vertical plane)*

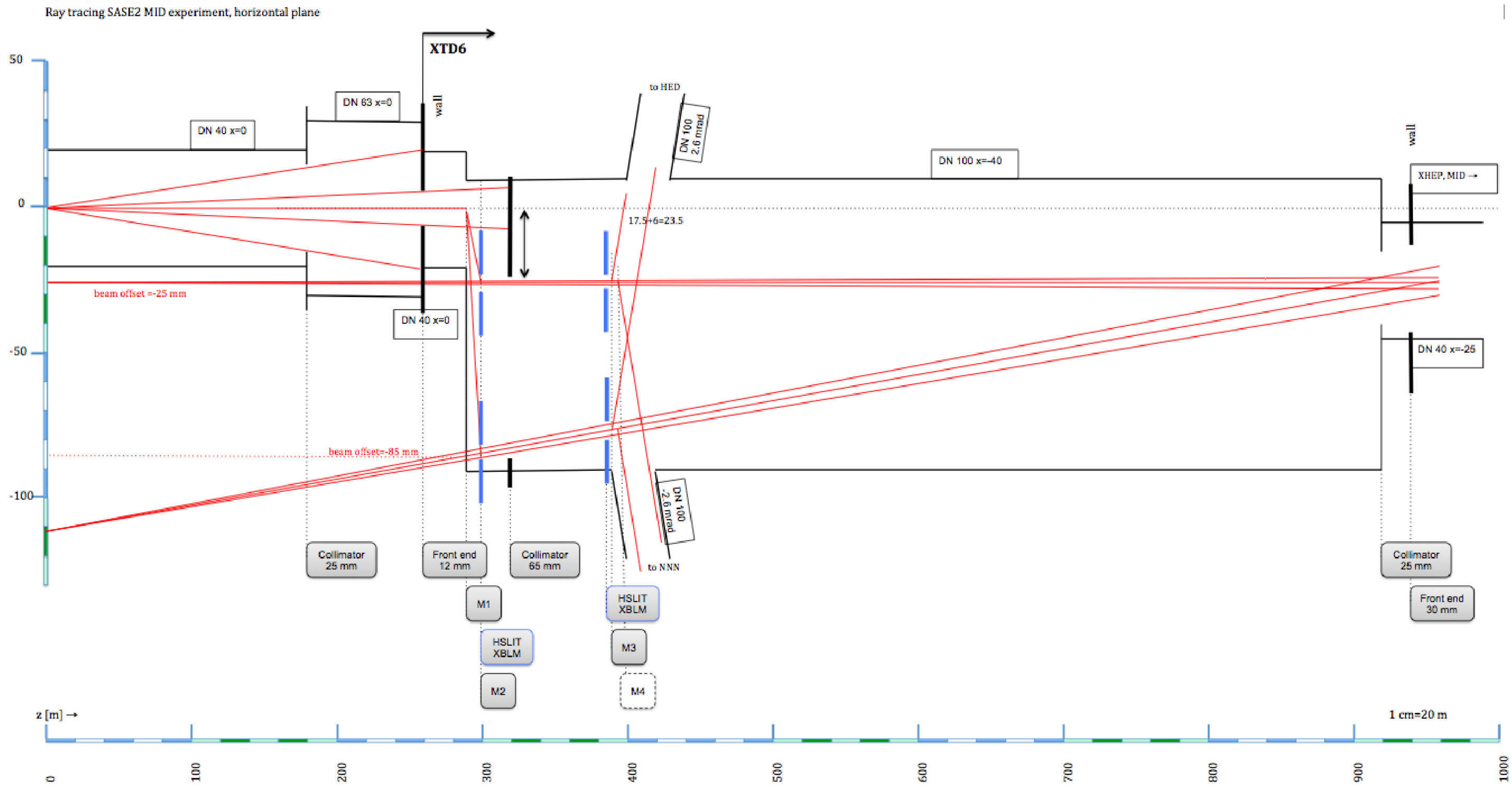

***Figure 115:*** *Ray tracing for SASE2, MID experiment (horizontal plane)*

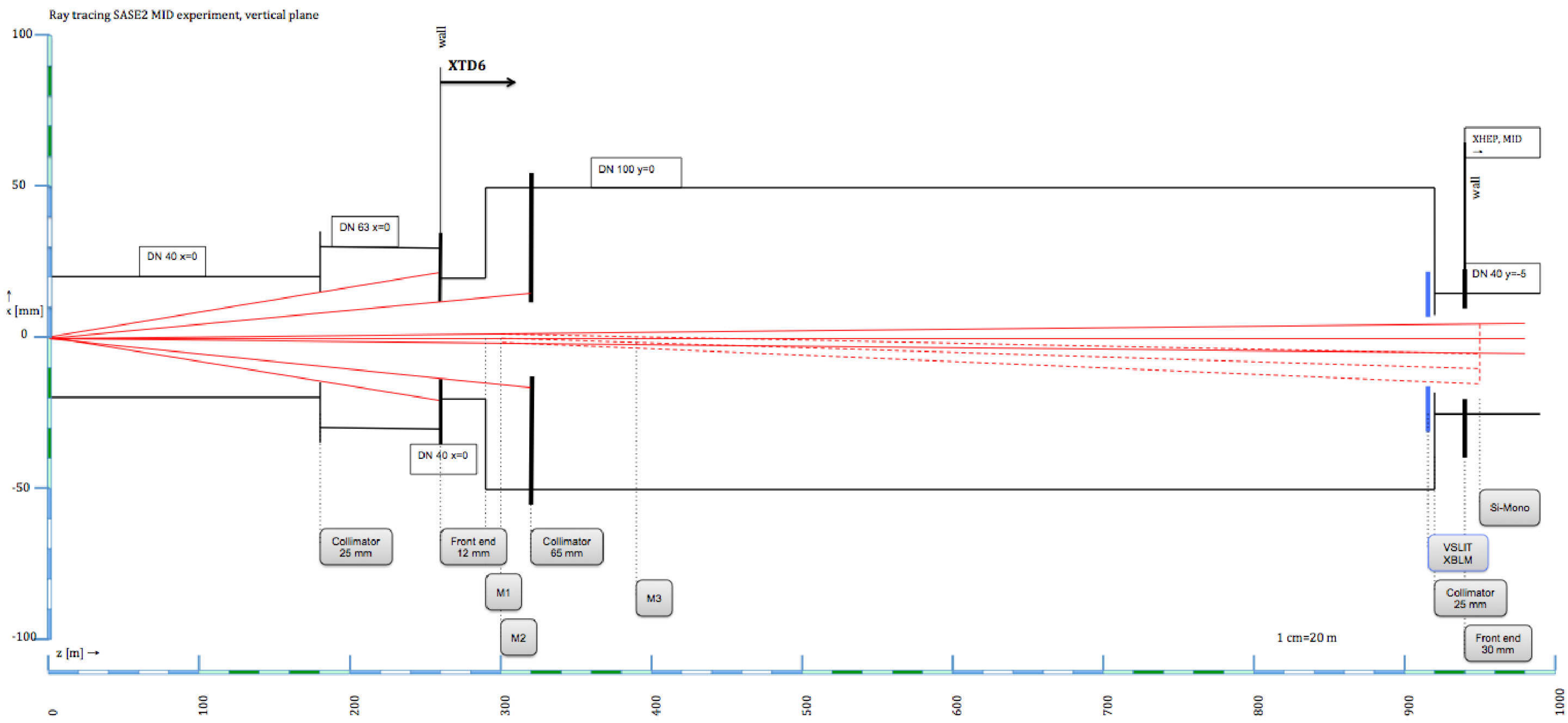

***Figure 116:*** *Ray tracing for SASE2, MID experiment (vertical plane)*

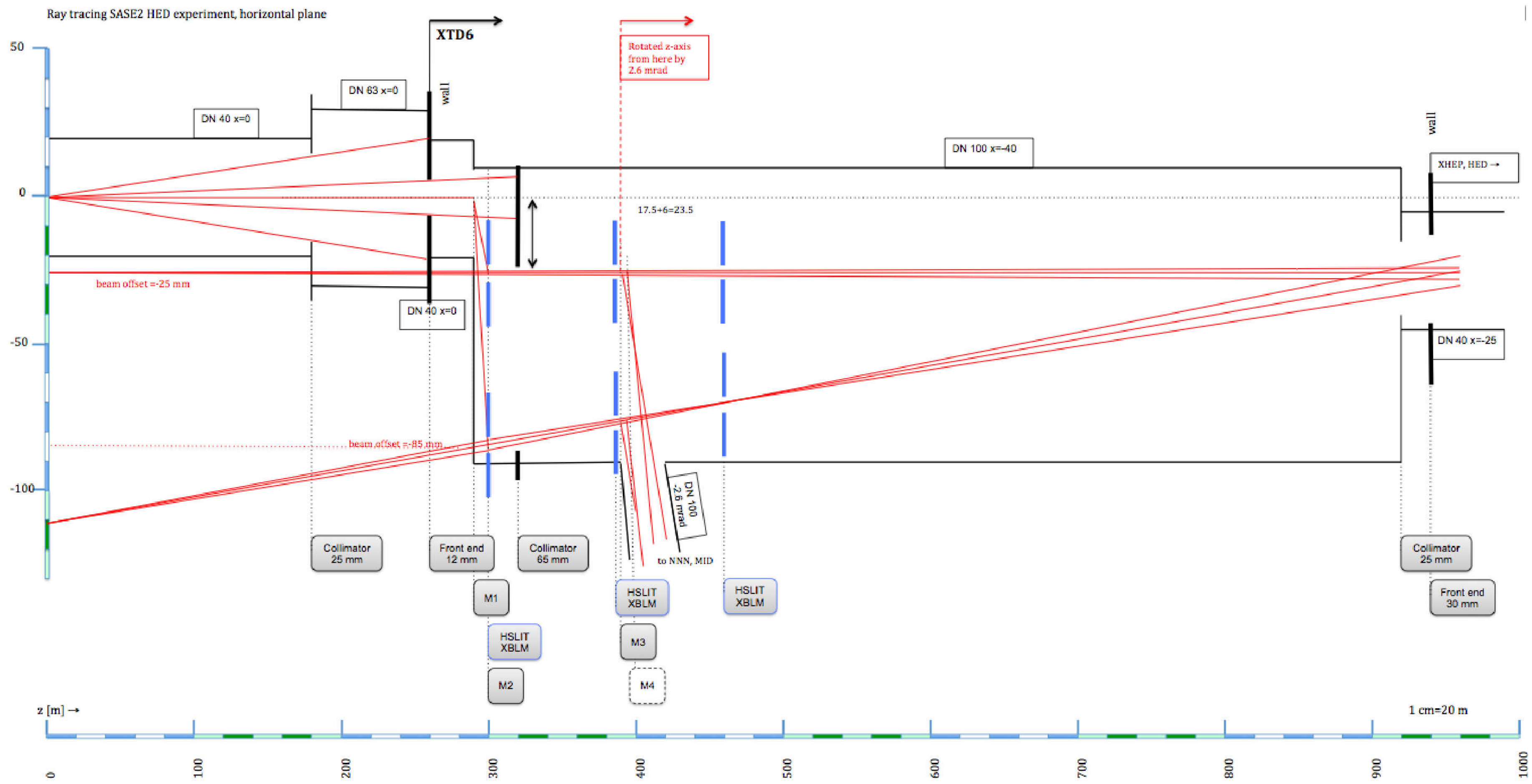

*Figure 117:* *Ray tracing for SASE2, HED experiment (horizontal plane)*

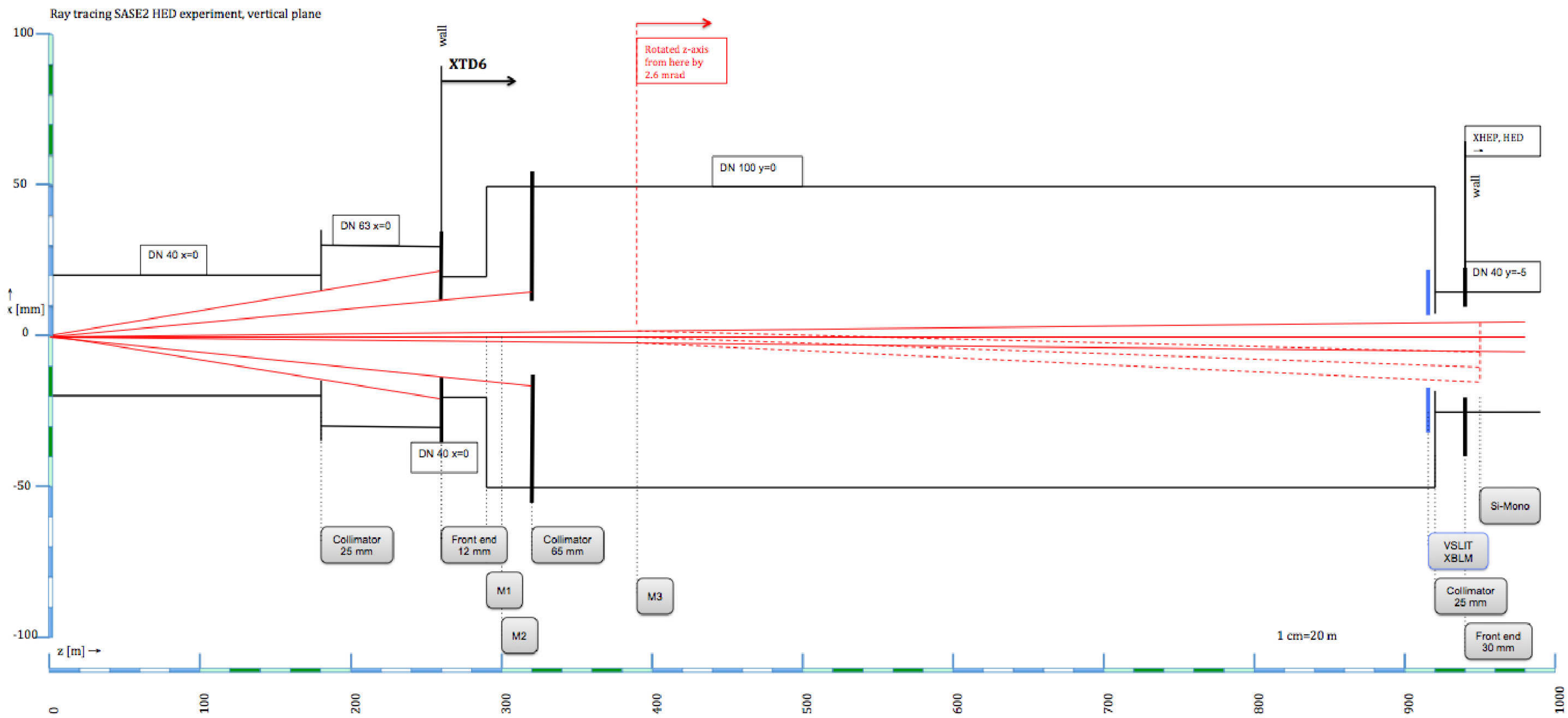

*Figure 118: Ray tracing for SASE2, HED experiment (vertical plane)*

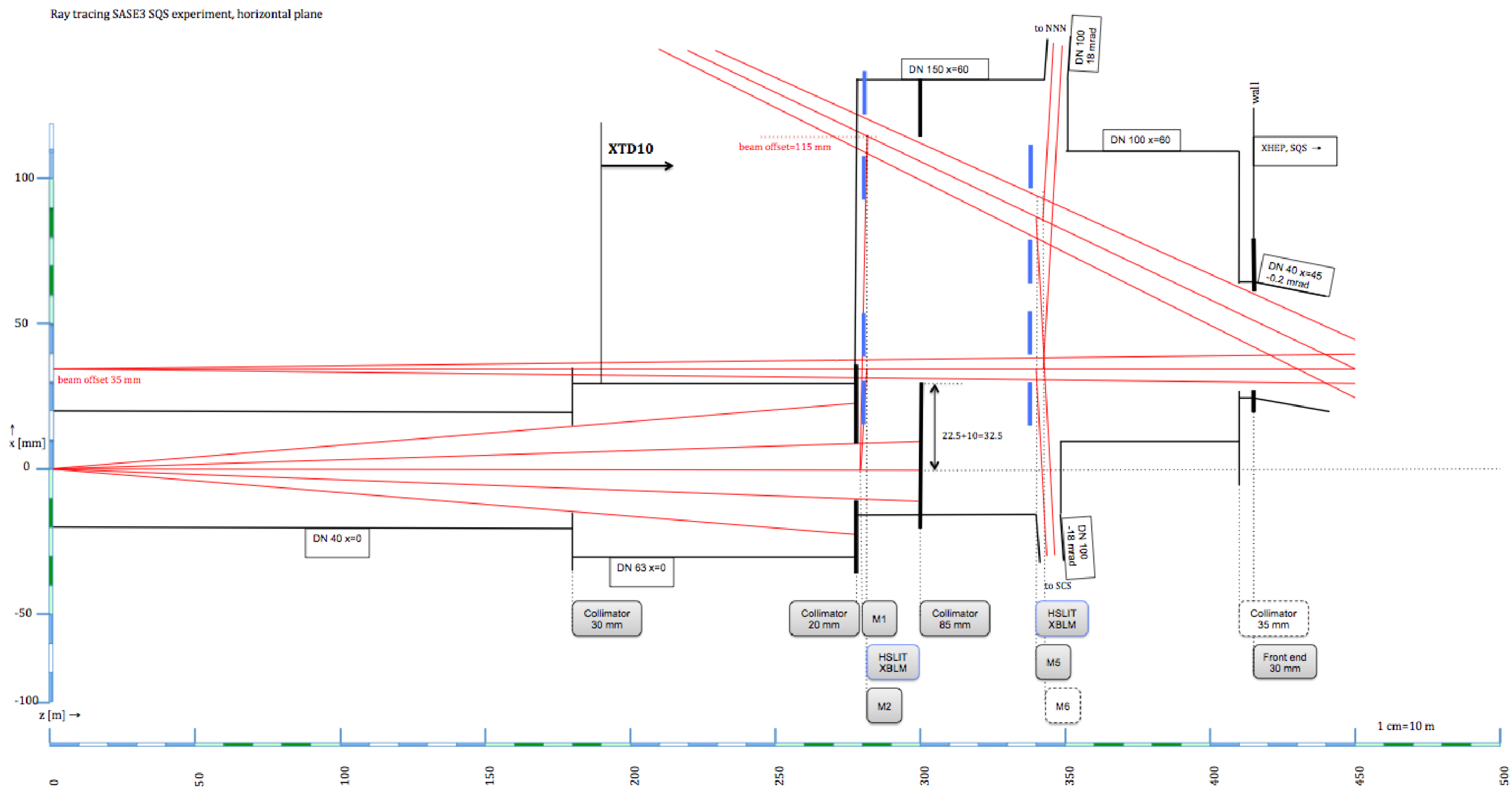

***Figure 119:** Ray tracing for SASE3, SQS experiment (horizontal plane)*

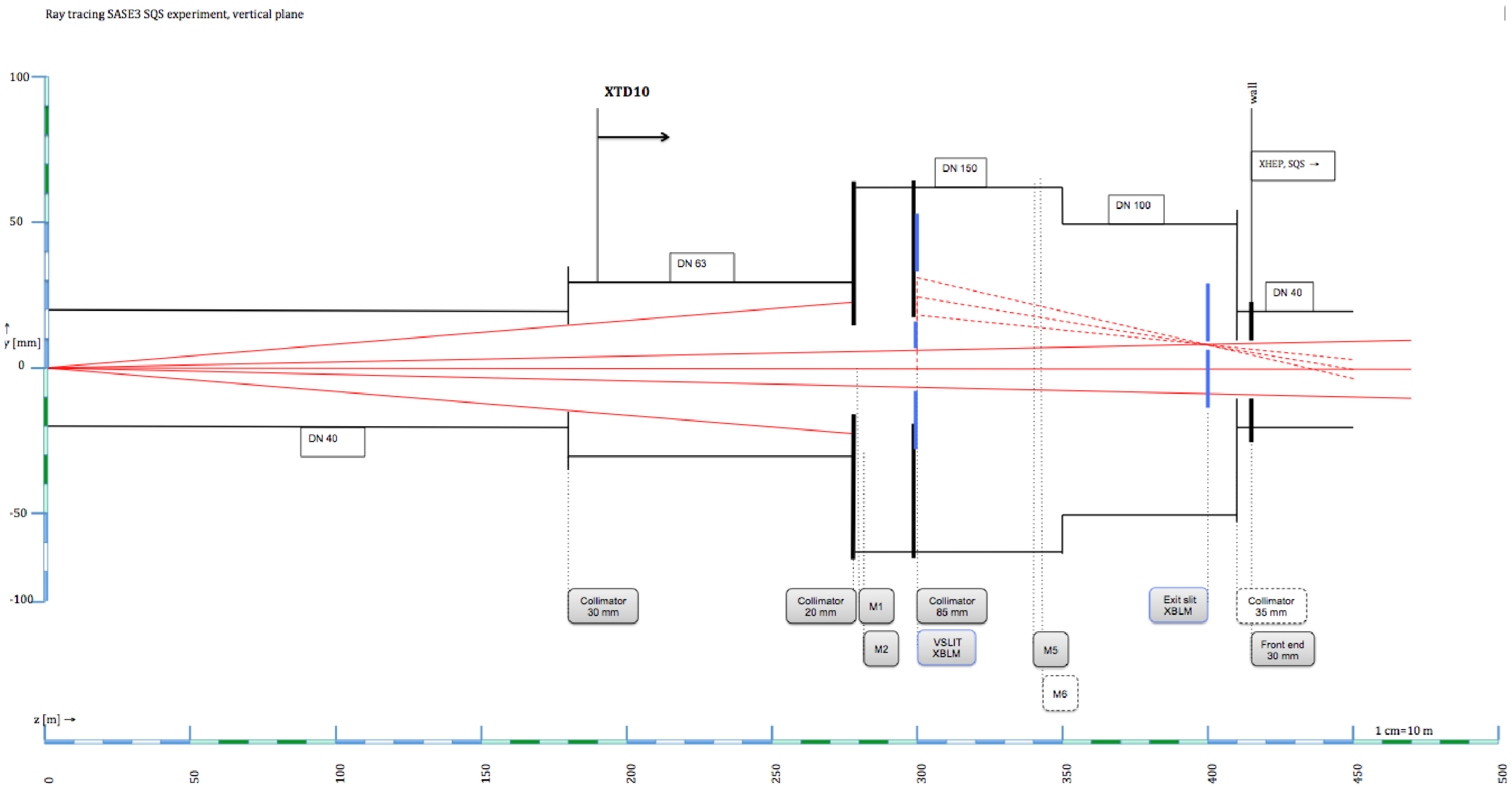

*Figure 120:* Ray tracing for SASE3, SQS experiment (vertical plane)

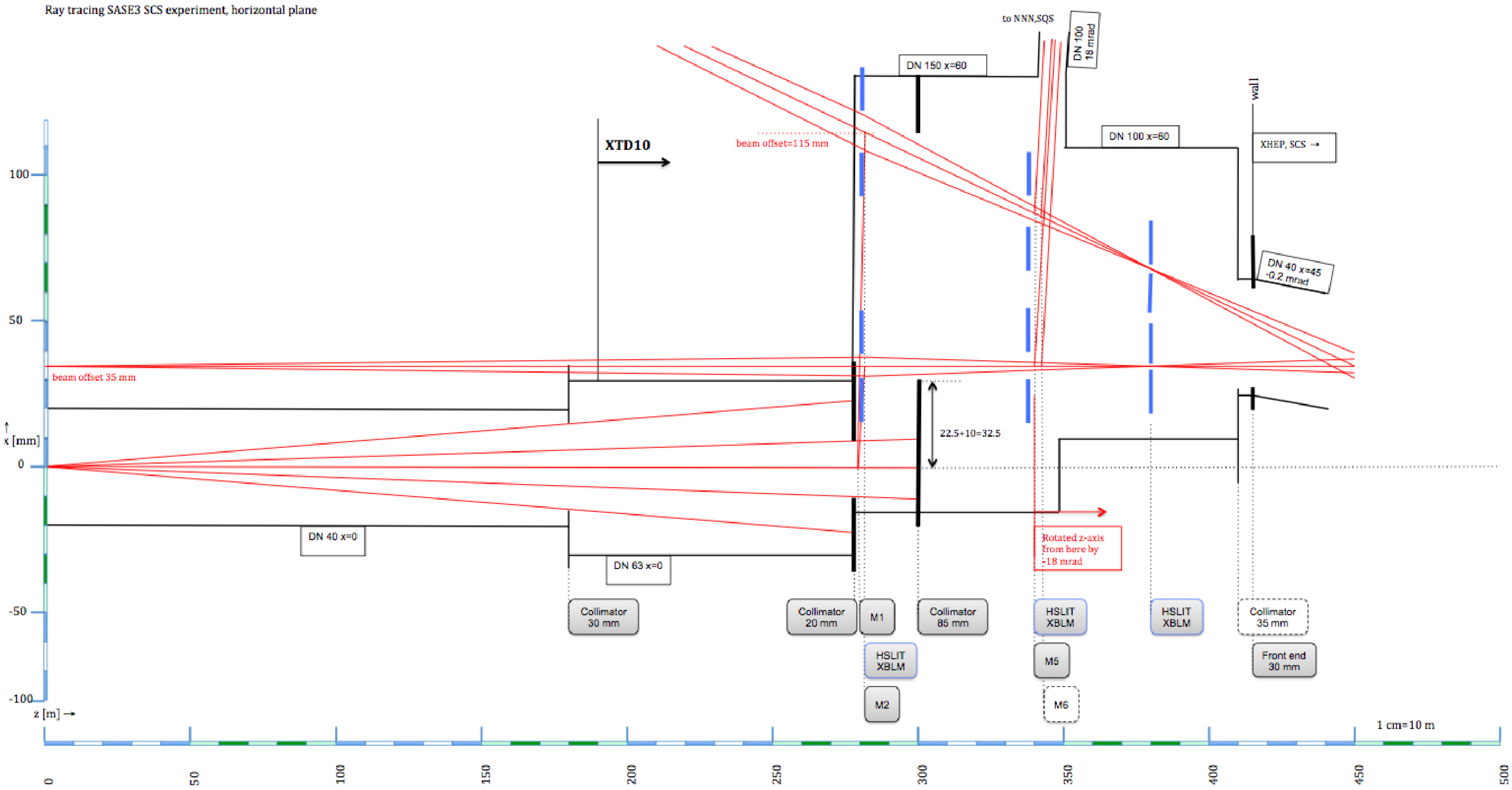

***Figure 121:*** *Ray tracing for SASE3, SCS experiment (horizontal plane)*

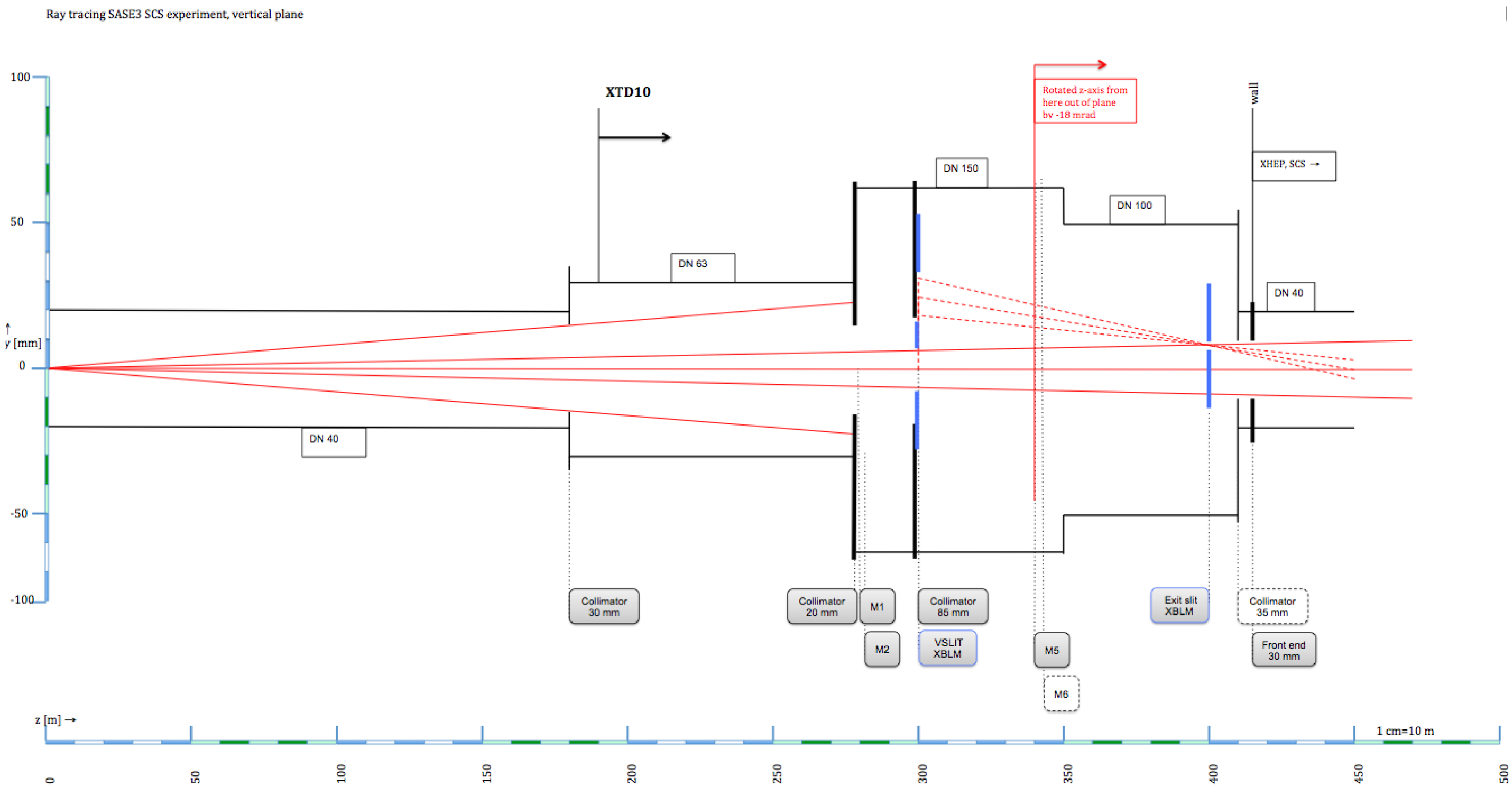

***Figure 122:*** *Ray tracing for SASE3, SCS experiment (vertical plane)*

# B Related documentation

ⓘ For some of the documents in "EDMS", a login is required.

The following documents provide additional technical documentation:

- "CDR: X-Ray Optics and Beam Transport" (EDMS D*2081421)
- "UHV Guidelines for X-Ray Beam Transport Systems"
- "CAD Integration Guidelines for Photon Beamline Components"
- "Beam transport component list" (EDMS D*2278111)
- "List with electrical rack configuration" (EDMS D*2911041)
- "Ray tracing plots" (EDMS D*3004861)
- "Specification Spontaneous Radiation Apertures (SRA)" (EDMS D*2022671)
- "Heat load calculations for SRAs (EDMS D*2004661)
- "Specifications for chamber for horizontal mirror (CHOM)" (EDMS D*3004041)
- "Bachelor thesis Jens Linnemann" (EDMS D*2597021)
- "Report FEA on mirrors" (EDMS D*1964541, D*2029231)
- "Vibration measurements in the XTD1 tunnel"
- "CDR: Framework for X-Ray Photon Diagnostics" (EDMS D*2851121)
- "CDR for K-mono for undulator tuning"  (EDMS D*1940181)
- "CDR for MCP based detector" (EDMS D*2850921)
- "'BO-Liste' with coordinate systems for CAD rooms" (EDMS D*496900)
- "LA and PD coordinate systems for XFEL" (in German, EDMS D*497635)
- "Coordinate Systems for the Beam Distribution Systems"

# Project plan

| ID | | Task Name | Duration | Start | Finish |
|---|---|---|---|---|---|
| 1 | | **Incomming Milestones** | **878 days** | **Mon 2/4/13** | **Thu 6/16/16** |
| 2 | | **WP32 Initial survey ready** | **163 days** | **Mon 2/4/13** | **Thu 9/19/13** |
| 3 | | XTD2 | 0 days | Wed 3/6/13 | Wed 3/6/13 |
| 4 | | XS3 | 0 days | Thu 9/19/13 | Thu 9/19/13 |
| 5 | | XTD9 | 0 days | Mon 2/4/13 | Mon 2/4/13 |
| 6 | | XTD10 | 0 days | Mon 6/3/13 | Mon 6/3/13 |
| 7 | | XTD1 | 0 days | Tue 4/16/13 | Tue 4/16/13 |
| 8 | | XS2 | 0 days | Thu 9/19/13 | Thu 9/19/13 |
| 9 | | XTD6 | 0 days | Fri 9/13/13 | Fri 9/13/13 |
| 10 | | XHEXP | 0 days | Thu 8/1/13 | Thu 8/1/13 |
| 11 | | **WP34 Infrastrucure ready** | **435 days** | **Tue 12/31/13** | **Tue 9/1/15** |
| 12 | | XTD2 | 0 days | Tue 12/31/13 | Tue 12/31/13 |
| 13 | | XS3 | 0 days | Fri 9/12/14 | Fri 9/12/14 |
| 14 | | XTD9 | 0 days | Fri 9/12/14 | Fri 9/12/14 |
| 15 | | XTD10 | 0 days | Fri 9/12/14 | Fri 9/12/14 |
| 16 | | XTD1 | 0 days | Fri 3/27/15 | Fri 3/27/15 |
| 17 | | XS2 | 0 days | Tue 9/1/15 | Tue 9/1/15 |
| 18 | | XTD6 | 0 days | Tue 9/1/15 | Tue 9/1/15 |
| 19 | | XHEXP | 0 days | Mon 9/1/14 | Mon 9/1/14 |
| 20 | | WP38 interlock RFI | 0 days | Thu 2/20/14 | Thu 2/20/14 |
| 21 | | **WP74 Diagnostics RFI** | **176 days** | **Fri 2/7/14** | **Mon 10/13/14** |
| 22 | | Pop-in monitor RFI | 0 days | Fri 5/30/14 | Fri 5/30/14 |
| 23 | | High res imagers RFI | 0 days | Mon 4/7/14 | Mon 4/7/14 |
| 24 | | K-Monos RFI | 0 days | Mon 4/28/14 | Mon 4/28/14 |
| 25 | | MCPs RFI | 0 days | Mon 10/13/14 | Mon 10/13/14 |
| 26 | | XGMDs XBPMs RFI | 0 days | Wed 5/28/14 | Wed 5/28/14 |
| 27 | | PES RFI | 0 days | Fri 2/7/14 | Fri 2/7/14 |
| 28 | | **WP76 Controls ready** | **479 days** | **Fri 8/15/14** | **Thu 6/16/16** |
| 29 | | **SASE1** | **413 days** | **Fri 8/15/14** | **Wed 3/16/16** |
| 30 | | minimal | 0 days | Fri 8/15/14 | Fri 8/15/14 |
| 31 | | pre-operational | 0 days | Tue 3/17/15 | Tue 3/17/15 |
| 32 | | operational | 0 days | Wed 3/16/16 | Wed 3/16/16 |
| 33 | | **SASE3** | **414 days** | **Fri 11/14/14** | **Thu 6/16/16** |
| 34 | | minimal | 0 days | Fri 11/14/14 | Fri 11/14/14 |
| 35 | | pre-operational | 0 days | Wed 6/17/15 | Wed 6/17/15 |
| 36 | | operational | 0 days | Thu 6/16/16 | Thu 6/16/16 |
| 37 | | **SASE2** | **436 days** | **Wed 10/15/14** | **Thu 6/16/16** |
| 38 | | minimal | 0 days | Wed 10/15/14 | Wed 10/15/14 |
| 39 | | pre-operational | 0 days | Fri 5/15/15 | Fri 5/15/15 |
| 40 | | operational | 0 days | Thu 6/16/16 | Thu 6/16/16 |
| 41 | | **Hardware production** | **931 days** | **Mon 1/2/12** | **Tue 7/28/15** |
| 42 | | **CHOMs (Mirror Chambers)** | **711 days** | **Mon 1/2/12** | **Tue 9/23/14** |
| 43 | | Design + Prototyping | 400 days | Mon 1/2/12 | Mon 7/15/13 |

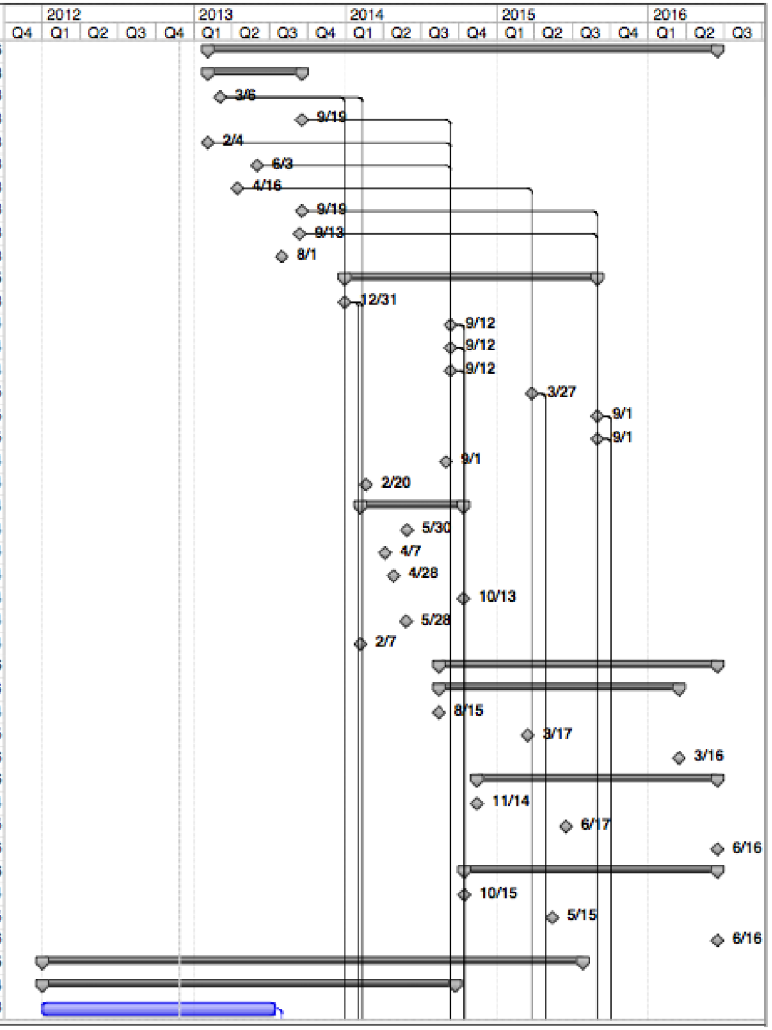

| ID |  | Task Name | Duration | Start | Finish |
|---|---|---|---|---|---|
| 44 | ▦ | Two prototypes received | 0 days | Mon 7/1/13 | Mon 7/1/13 |
| 45 |  | Procurement | 100 days | Mon 7/15/13 | Mon 12/2/13 |
| 46 |  | Manufacturing | 180 days | Mon 12/2/13 | Mon 8/11/14 |
| 47 |  | Testing | 30 days | Mon 8/11/14 | Mon 9/22/14 |
| 48 | ▦ | Two CHOMs RFI | 1.13 days | Wed 1/1/14 | Thu 1/2/14 |
| 49 |  | RFI (ready for installation) | 1 day | Mon 9/22/14 | Tue 9/23/14 |
| 50 |  | **HOMs, HDMs (Mirrors)** | **931 days** | **Mon 1/2/12** | **Tue 7/28/15** |
| 51 |  | Design + Prototyping | 330 days | Mon 1/2/12 | Mon 4/8/13 |
| 52 | ▦ | Prototype adaptive mirror received | 0 days | Mon 3/4/13 | Mon 3/4/13 |
| 53 |  | Procurement | 120 days | Mon 4/8/13 | Mon 9/23/13 |
| 54 |  | Manufacturing | 360 days | Mon 9/23/13 | Mon 2/9/15 |
| 55 |  | Testing | 120 days | Mon 2/9/15 | Mon 7/27/15 |
| 56 | ▦ | 3 mirrors RFI | 1.13 days | Fri 1/2/15 | Mon 1/5/15 |
| 57 |  | RFI (ready for installation) | 1 day | Mon 7/27/15 | Tue 7/28/15 |
| 58 |  | **Soft X-ray Mono** | **695 days** | **Mon 1/2/12** | **Mon 9/1/14** |
| 59 |  | Concept + design phase | 280 days | Mon 1/2/12 | Mon 1/28/13 |
| 60 |  | Procurement | 180 days | Mon 1/28/13 | Mon 10/7/13 |
| 61 |  | Manufacturing | 230 days | Mon 10/7/13 | Mon 8/25/14 |
| 62 |  | Acceptance tests | 4 days | Mon 8/25/14 | Fri 8/29/14 |
| 63 |  | RFI | 1 day | Fri 8/29/14 | Mon 9/1/14 |
| 64 |  | **Exits Slits** | **621 days** | **Mon 1/2/12** | **Tue 5/20/14** |
| 65 |  | Conceptual design | 310 days | Mon 1/2/12 | Mon 3/11/13 |
| 66 |  | Procurement | 120 days | Mon 3/11/13 | Mon 8/26/13 |
| 67 |  | Manufacturing | 180 days | Mon 8/26/13 | Mon 5/5/14 |
| 68 |  | Testing | 10 days | Mon 5/5/14 | Mon 5/19/14 |
| 69 |  | RFI | 1 day | Mon 5/19/14 | Tue 5/20/14 |
| 70 |  | **Gratings** | **861 days** | **Mon 1/2/12** | **Tue 4/21/15** |
| 71 |  | Conceptual design | 260 days | Mon 1/2/12 | Mon 12/31/12 |
| 72 |  | Procurement substartes | 120 days | Mon 12/31/12 | Mon 6/17/13 |
| 73 |  | Manufacturing substrates | 200 days | Mon 6/17/13 | Mon 3/24/14 |
| 74 |  | Test phase ruling | 60 days | Mon 3/24/14 | Mon 6/16/14 |
| 75 |  | Ruling | 60 days | Mon 6/16/14 | Mon 9/8/14 |
| 76 |  | Metrology | 120 days | Mon 9/8/14 | Mon 2/23/15 |
| 77 |  | Coating | 40 days | Mon 2/23/15 | Mon 4/20/15 |
| 78 |  | RFI (ready for installation) | 1 day | Mon 4/20/15 | Tue 4/21/15 |
| 79 |  | **Pre-mirrors** | **921 days** | **Mon 1/2/12** | **Tue 7/14/15** |
| 80 |  | Conceptual Design | 280 days | Mon 1/2/12 | Mon 1/28/13 |
| 81 |  | Procurement | 120 days | Mon 1/28/13 | Mon 7/15/13 |
| 82 |  | Manufacturing | 360 days | Mon 7/15/13 | Mon 12/1/14 |
| 83 |  | Metrology | 120 days | Mon 12/1/14 | Mon 5/18/15 |
| 84 |  | Coating | 40 days | Mon 5/18/15 | Mon 7/13/15 |
| 85 |  | RFI (ready for installation) | 1 day | Mon 7/13/15 | Tue 7/14/15 |
| 86 |  | **Hard X-ray Monos** | **825.88 days** | **Mon 1/2/12** | **Mon 3/2/15** |

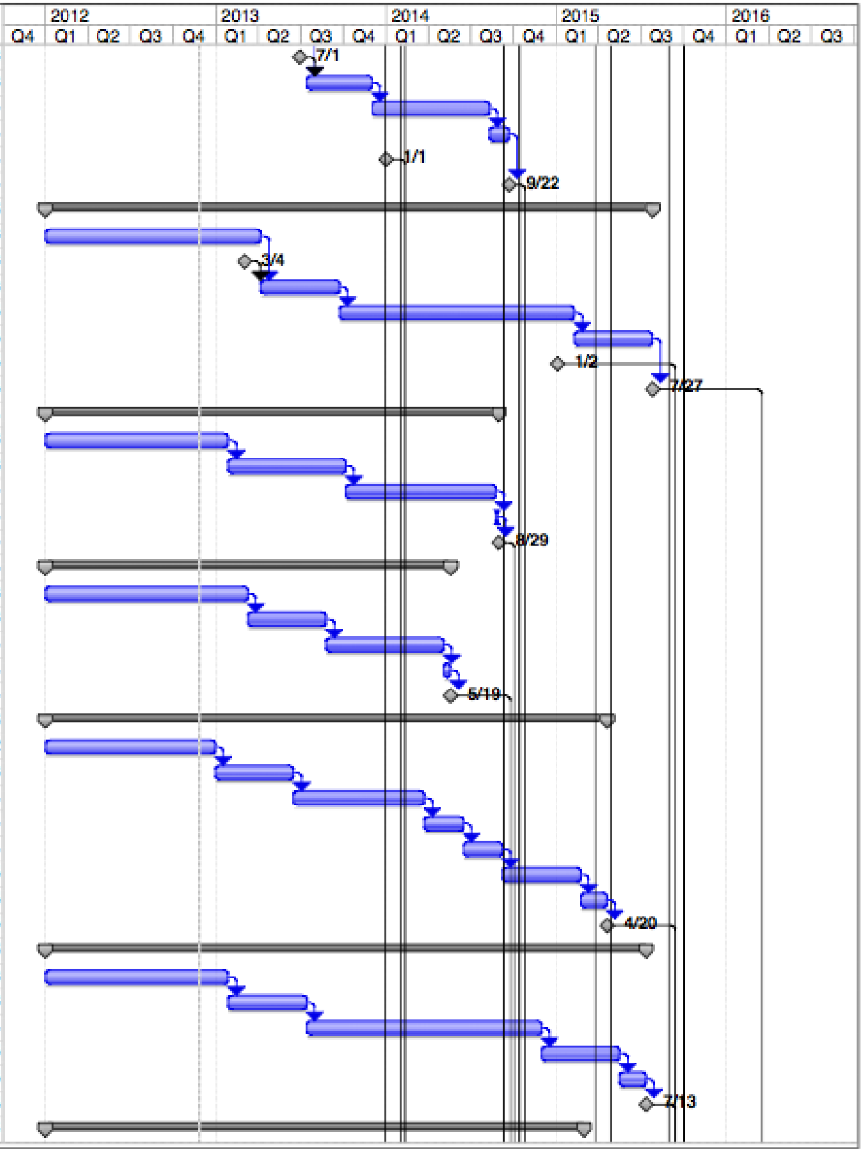

| ID | | Task Name | Duration | Start | Finish |
|---|---|---|---|---|---|
| 87 | | Design phase | 220 days | Mon 1/2/12 | Mon 11/5/12 |
| 88 | | Procurement prototype (SASE1) w/o table | 212 days | Mon 11/5/12 | Wed 8/28/13 |
| 89 | | Manufacturing | 140 days | Wed 8/28/13 | Wed 3/12/14 |
| 90 | | Tests | 60 days | Wed 3/12/14 | Wed 6/4/14 |
| 91 | ▦ | Procurement series (SASE2 monos) | 180 days | Mon 9/2/13 | Fri 5/9/14 |
| 92 | | Manufacturing | 180 days | Mon 5/12/14 | Fri 1/16/15 |
| 93 | | Accptance tests | 30 days | Mon 1/19/15 | Fri 2/27/15 |
| 94 | | RFI | 1 day | Mon 3/2/15 | Mon 3/2/15 |
| 95 | | **Vacuum System** | **781 days** | **Mon 1/2/12** | **Tue 12/30/14** |
| 96 | | **Vacuum pipes** | **781 days** | **Mon 1/2/12** | **Tue 12/30/14** |
| 97 | | Design phase | 500 days | Mon 1/2/12 | Mon 12/2/13 |
| 98 | | Procurement | 120 days | Mon 12/3/12 | Mon 5/20/13 |
| 99 | | Manufacturing | 300 days | Mon 5/20/13 | Mon 7/14/14 |
| 100 | | Acceptance tests? | 120 days | Mon 7/14/14 | Mon 12/29/14 |
| 101 | ▦ | First components RFI | 1.13 days | Thu 1/2/14 | Fri 1/3/14 |
| 102 | | All comoments RFI | 1 day | Mon 12/29/14 | Tue 12/30/14 |
| 103 | | **Stands** | **781 days** | **Mon 1/2/12** | **Tue 12/30/14** |
| 104 | | Design phase | 500 days | Mon 1/2/12 | Mon 12/2/13 |
| 105 | | Procurement | 120 days | Mon 12/3/12 | Mon 5/20/13 |
| 106 | | Manufacturing | 300 days | Mon 5/20/13 | Mon 7/14/14 |
| 107 | | Testing | 120 days | Mon 7/14/14 | Mon 12/29/14 |
| 108 | ▦ | first components RFI | 1.13 days | Thu 1/2/14 | Fri 1/3/14 |
| 109 | | all comoments RFI | 1 day | Mon 12/29/14 | Tue 12/30/14 |
| 110 | | **Valves, Ion pumps** | **701 days** | **Mon 1/2/12** | **Tue 9/9/14** |
| 111 | | Design phase | 500 days | Mon 1/2/12 | Mon 12/2/13 |
| 112 | | Procurement | 120 days | Mon 12/31/12 | Mon 6/17/13 |
| 113 | | Manufacturing | 200 days | Mon 6/17/13 | Mon 3/24/14 |
| 114 | | Testing | 120 days | Mon 3/24/14 | Mon 9/8/14 |
| 115 | ▦ | first components RFI | 1.13 days | Thu 1/2/14 | Fri 1/3/14 |
| 116 | | all comoments RFI | 1 day | Mon 9/8/14 | Tue 9/9/14 |
| 117 | | **Gas Attenuator (GAT)** | **521 days** | **Mon 1/2/12** | **Tue 12/31/13** |
| 118 | | Design phase | 200 days | Mon 1/2/12 | Mon 10/8/12 |
| 119 | | Procurement+Manufacturing | 120 days | Mon 10/8/12 | Mon 3/25/13 |
| 120 | | Testing + optimization | 200 days | Mon 3/25/13 | Mon 12/30/13 |
| 121 | | RFI | 1 day | Mon 12/30/13 | Tue 12/31/13 |
| 122 | | **Differential pumps** | **541 days** | **Mon 1/2/12** | **Tue 1/28/14** |
| 123 | | Design phase | 320 days | Mon 1/2/12 | Mon 3/25/13 |
| 124 | | Procurement+Manufacturing | 100 days | Mon 3/25/13 | Mon 8/12/13 |
| 125 | | Testing | 120 days | Mon 8/12/13 | Mon 1/27/14 |
| 126 | | RFI | 1 day | Mon 1/27/14 | Tue 1/28/14 |
| 127 | | **SRAs (BLM-Apertures)** | **481 days** | **Mon 4/2/12** | **Mon 2/3/14** |
| 128 | ▦ | Prototype received | 0 days | Mon 4/2/12 | Mon 4/2/12 |
| 129 | | Test + re-design | 160 days | Mon 4/2/12 | Fri 11/9/12 |

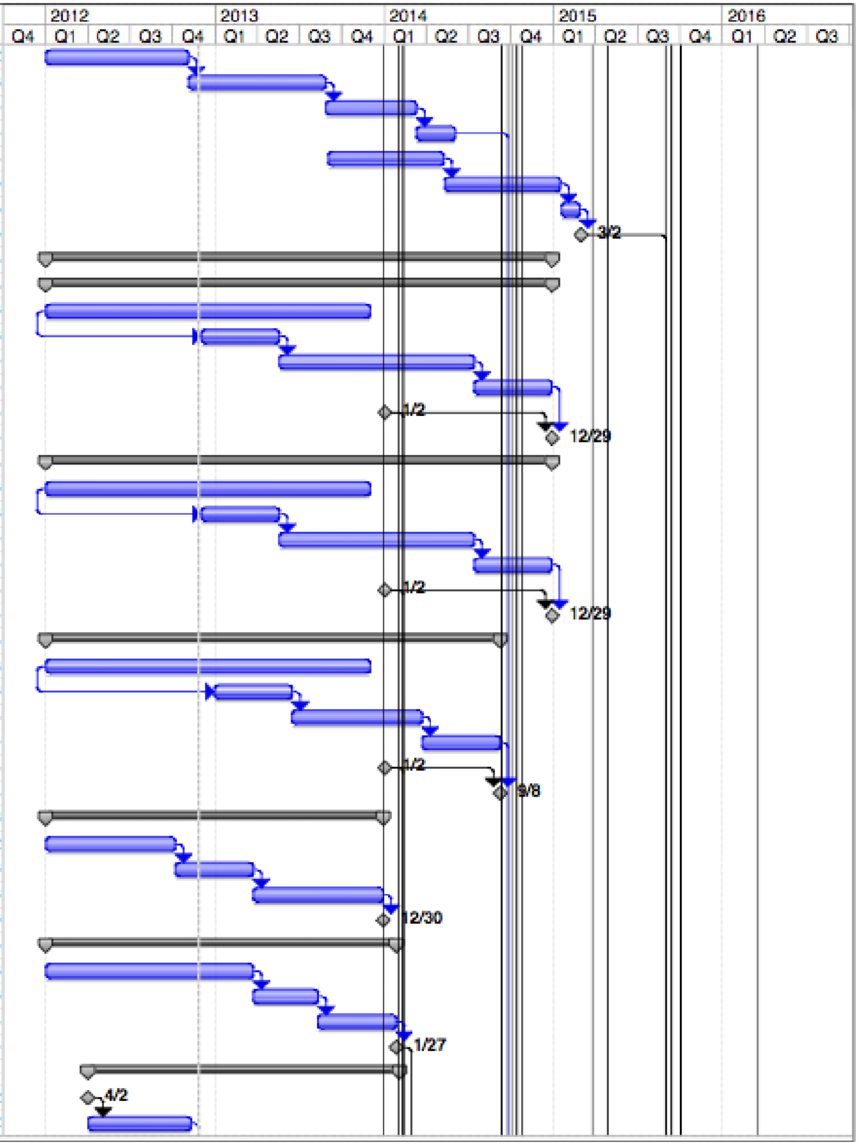

| ID | | Task Name | Duration | Start | Finish |
|---|---|---|---|---|---|
| 130 | | Procurement | 100 days | Mon 11/12/12 | Fri 3/29/13 |
| 131 | | Manufacturing | 200 days | Mon 4/1/13 | Fri 1/3/14 |
| 132 | | Acceptance tests | 20 days | Mon 1/6/14 | Fri 1/31/14 |
| 133 | | RFI | 1 day | Mon 2/3/14 | Mon 2/3/14 |
| 134 | | **Front ends** | **541 days** | **Mon 1/2/12** | **Tue 1/28/14** |
| 135 | | Conceptual design | 240 days | Mon 1/2/12 | Mon 12/3/12 |
| 136 | | Procurement | 120 days | Mon 12/3/12 | Mon 5/20/13 |
| 137 | | Manufacturing | 160 days | Mon 5/20/13 | Mon 12/30/13 |
| 138 | | Acceptance tests | 20 days | Mon 12/30/13 | Mon 1/27/14 |
| 139 | | RFI | 1 day | Mon 1/27/14 | Tue 1/28/14 |
| 140 | | **Solid Attenutors** | **501 days** | **Mon 1/2/12** | **Tue 12/3/13** |
| 141 | | Design phase | 240 days | Mon 1/2/12 | Mon 12/3/12 |
| 142 | | Procurement | 120 days | Mon 12/3/12 | Mon 5/20/13 |
| 143 | | Manufacturing | 120 days | Mon 5/20/13 | Mon 11/4/13 |
| 144 | | Acceptance tests | 20 days | Mon 11/4/13 | Mon 12/2/13 |
| 145 | | RFI | 1 day | Mon 12/2/13 | Tue 12/3/13 |
| 146 | | **CRLs** | **521 days** | **Mon 1/2/12** | **Tue 12/31/13** |
| 147 | | Design phase | 260 days | Mon 1/2/12 | Mon 12/31/12 |
| 148 | | Procurement | 120 days | Mon 12/31/12 | Mon 6/17/13 |
| 149 | | Manufacturing | 120 days | Mon 6/17/13 | Mon 12/2/13 |
| 150 | | Acceptance tests | 20 days | Mon 12/2/13 | Mon 12/30/13 |
| 151 | | RFI | 1 day | Mon 12/30/13 | Tue 12/31/13 |
| 152 | | **Fixed Collimators** | **541 days** | **Mon 1/2/12** | **Tue 1/28/14** |
| 153 | | Design phase | 280 days | Mon 1/2/12 | Mon 1/28/13 |
| 154 | | Procurement | 120 days | Mon 1/28/13 | Mon 7/15/13 |
| 155 | | Manufacturing | 120 days | Mon 7/15/13 | Mon 12/30/13 |
| 156 | | Acceptance tests | 20 days | Mon 12/30/13 | Mon 1/27/14 |
| 157 | | RFI | 1 day | Mon 1/27/14 | Tue 1/28/14 |
| 158 | | **Controls Hardware** | **541 days** | **Mon 1/2/12** | **Tue 1/28/14** |
| 159 | | Design phase | 240 days | Mon 1/2/12 | Mon 12/3/12 |
| 160 | | Procurement | 120 days | Mon 12/3/12 | Mon 5/20/13 |
| 161 | | Manufacturing | 120 days | Mon 5/20/13 | Mon 11/4/13 |
| 162 | | Testing | 60 days | Mon 11/4/13 | Mon 1/27/14 |
| 163 | | RFI | 1 day | Mon 1/27/14 | Tue 1/28/14 |
| 164 | | **Tunnels RFI , closed** | **548.25 days** | **Tue 2/25/14** | **Fri 4/1/16** |
| 165 | ▤ | XTD2 RFI | 1.13 days | Tue 2/25/14 | Wed 2/26/14 |
| 166 | ▤ | XDT9 and XS3 RFI | 1 day | Fri 10/10/14 | Fri 10/10/14 |
| 167 | ▤ | XTD10 RFI | 1 day | Fri 10/10/14 | Fri 10/10/14 |
| 168 | ▤ | XTD1 RFI | 1 day | Fri 4/24/15 | Fri 4/24/15 |
| 169 | ▤ | XTD6 and XS2 RFI | 1 day | Tue 9/15/15 | Tue 9/15/15 |
| 170 | ▤ | XDT2,9,10 closed | 1 day | Mon 9/28/15 | Mon 9/28/15 |
| 171 | ▤ | XTD1,6 closed | 1.13 days | Thu 3/31/16 | Fri 4/1/16 |
| 172 | | **Installation** | **586 days** | **Tue 12/31/13** | **Wed 3/30/16** |

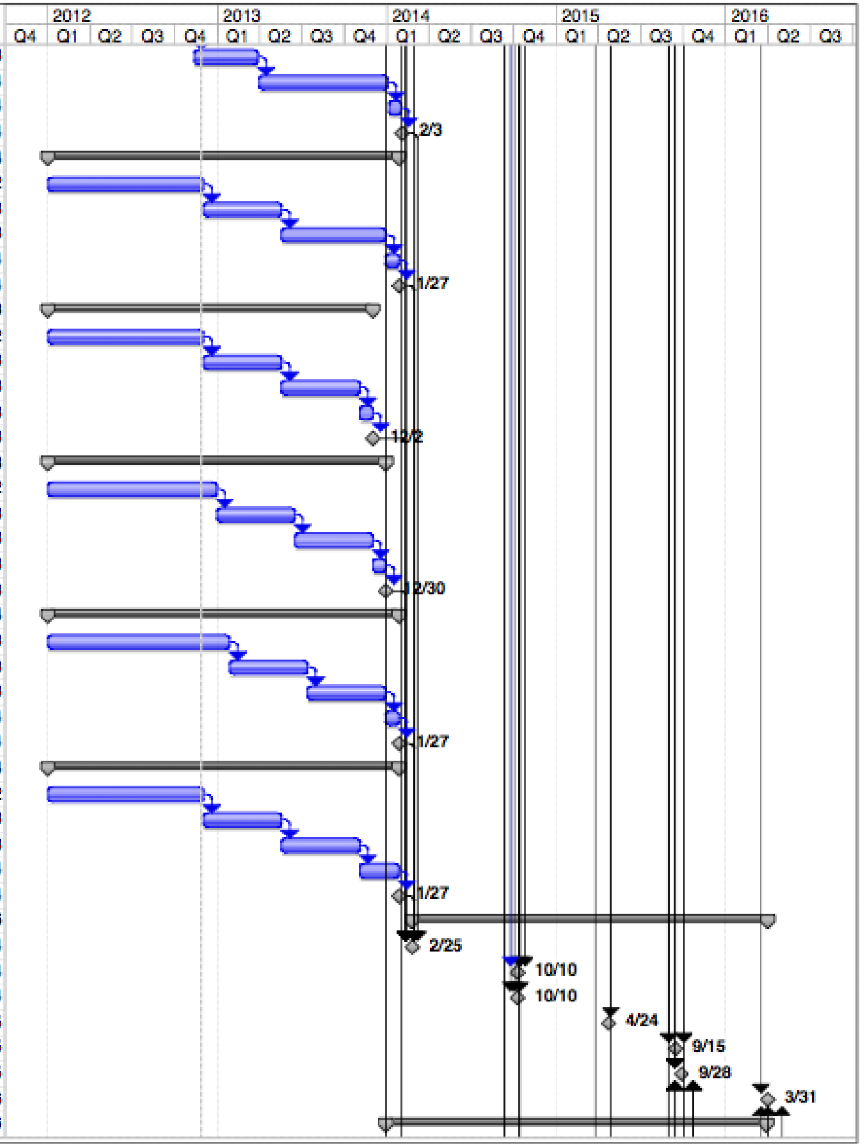

| ID | Task Name | Duration | Start | Finish |
|---|---|---|---|---|
| 173 | **XTD2 (SASE 1)** | **371 days** | **Tue 12/31/13** | **Wed 6/3/15** |
| 174 | Drilling holes + concrete work | 20 days | Tue 12/31/13 | Tue 1/28/14 |
| 175 | Transport of Material | 20 days | Tue 1/28/14 | Tue 2/25/14 |
| 176 | E-racks | 30 days | Tue 2/25/14 | Tue 4/8/14 |
| 177 | Stands | 30 days | Tue 4/8/14 | Tue 5/20/14 |
| 178 | UHV beam pipes | 60 days | Tue 5/20/14 | Tue 8/12/14 |
| 179 | UHV optics components | 60 days | Tue 8/12/14 | Tue 11/4/14 |
| 180 | UHV diagnostics | 30 days | Tue 11/4/14 | Tue 12/16/14 |
| 181 | UHV pump down&testing | 60 days | Tue 12/16/14 | Tue 3/10/15 |
| 182 | Controls testing | 60 days | Tue 3/10/15 | Tue 6/2/15 |
| 183 | RFB | 1 day | Tue 6/2/15 | Wed 6/3/15 |
| 184 | **XS3 (SASE 1)** | **158 days** | **Fri 9/12/14** | **Wed 4/22/15** |
| 185 | Drilling holes + concrete work | 2 days | Fri 9/12/14 | Tue 9/16/14 |
| 186 | Transport of Material | 5 days | Tue 9/16/14 | Tue 9/23/14 |
| 187 | E-racks | 5 days | Tue 9/23/14 | Tue 9/30/14 |
| 188 | Stands | 5 days | Tue 9/30/14 | Tue 10/7/14 |
| 189 | UHV beam pipes | 10 days | Tue 10/7/14 | Tue 10/21/14 |
| 190 | UHV optics components | 10 days | Tue 10/21/14 | Tue 11/4/14 |
| 191 | UHV pump down&testing | 60 days | Tue 11/4/14 | Tue 1/27/15 |
| 192 | Controls testing | 60 days | Tue 1/27/15 | Tue 4/21/15 |
| 193 | RFB | 1 day | Tue 4/21/15 | Wed 4/22/15 |
| 194 | **XTD9 (SASE1)** | **266 days** | **Fri 9/12/14** | **Mon 9/21/15** |
| 195 | Drilling holes + concrete work | 20 days | Fri 9/12/14 | Fri 10/10/14 |
| 196 | Transport of Material | 20 days | Fri 10/10/14 | Fri 11/7/14 |
| 197 | E-racks | 20 days | Fri 11/7/14 | Fri 12/5/14 |
| 198 | Stands | 20 days | Fri 12/5/14 | Fri 1/2/15 |
| 199 | UHV beam pipes | 60 days | Fri 1/2/15 | Fri 3/27/15 |
| 200 | UHV optics components | 50 days | Fri 3/27/15 | Fri 6/5/15 |
| 201 | UHV diagnostics | 20 days | Fri 6/5/15 | Fri 7/3/15 |
| 202 | UHV pump down&testing | 40 days | Fri 7/3/15 | Fri 8/28/15 |
| 203 | Controls testing | 15 days | Fri 8/28/15 | Fri 9/18/15 |
| 204 | RFB | 1 day | Fri 9/18/15 | Mon 9/21/15 |
| 205 | **XTD10 (SASE3)** | **266 days** | **Fri 9/12/14** | **Mon 9/21/15** |
| 206 | Drilling holes + concrete work | 20 days | Fri 9/12/14 | Fri 10/10/14 |
| 207 | Transport of Material | 20 days | Fri 10/10/14 | Fri 11/7/14 |
| 208 | E-racks | 20 days | Fri 11/7/14 | Fri 12/5/14 |
| 209 | Stands | 20 days | Fri 12/5/14 | Fri 1/2/15 |
| 210 | UHV beam pipes | 40 days | Fri 1/2/15 | Fri 2/27/15 |
| 211 | UHV optics components | 60 days | Fri 2/27/15 | Fri 5/22/15 |
| 212 | UHV diagnostics | 30 days | Fri 5/22/15 | Fri 7/3/15 |
| 213 | UHV pump down&testing | 40 days | Fri 7/3/15 | Fri 8/28/15 |
| 214 | Controls testing | 15 days | Fri 8/28/15 | Fri 9/18/15 |
| 215 | RFB | 1 day | Fri 9/18/15 | Mon 9/21/15 |

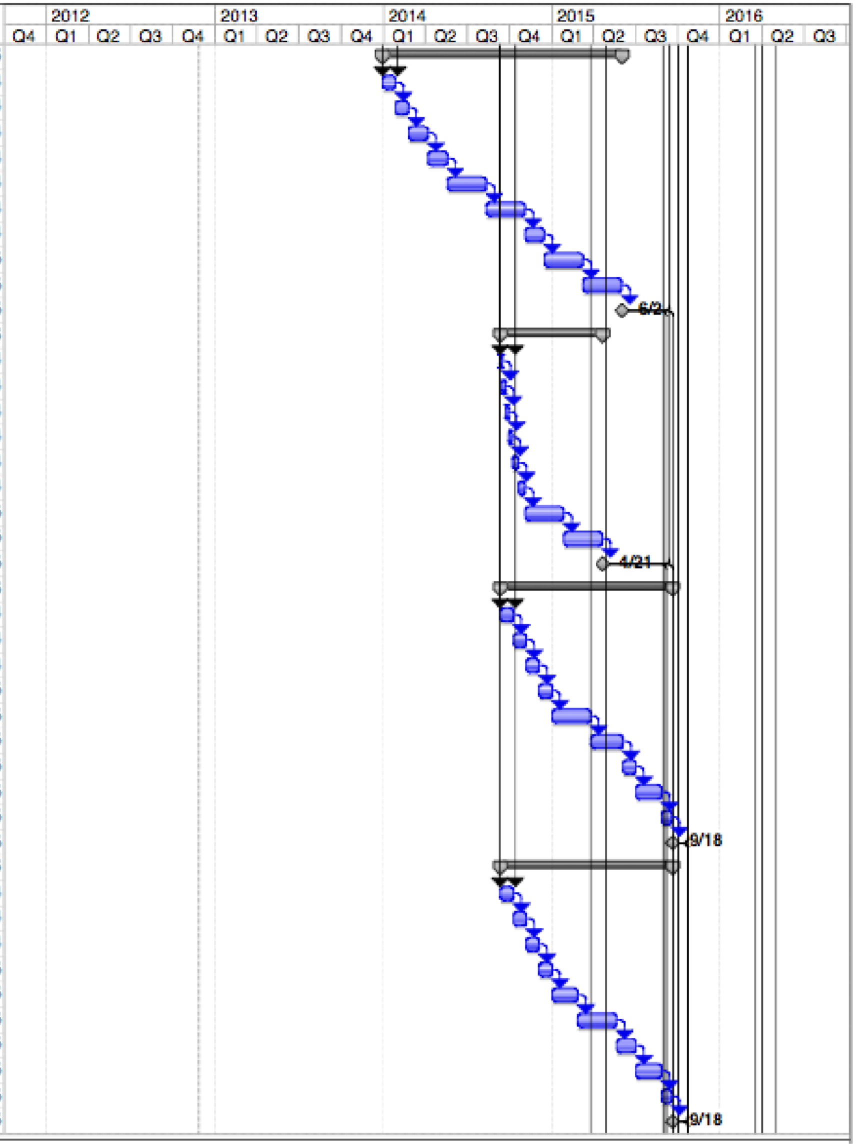

| ID | Task Name | Duration | Start | Finish |
|---|---|---|---|---|
| 216 | **XTD1 (SASE2)** | **241 days** | **Fri 3/27/15** | **Mon 2/29/16** |
| 217 | Drilling holes + concrete work | 20 days | Fri 3/27/15 | Fri 4/24/15 |
| 218 | Transport of Material | 20 days | Fri 4/24/15 | Fri 5/22/15 |
| 219 | E-racks | 20 days | Fri 5/22/15 | Fri 6/19/15 |
| 220 | Stands | 20 days | Fri 6/19/15 | Fri 7/17/15 |
| 221 | UHV beam pipes | 30 days | Fri 7/17/15 | Fri 8/28/15 |
| 222 | UHV optics components | 40 days | Fri 8/28/15 | Fri 10/23/15 |
| 223 | UHV diagnostics | 30 days | Fri 10/23/15 | Fri 12/4/15 |
| 224 | UHV pump down&testing | 40 days | Fri 12/4/15 | Fri 1/29/16 |
| 225 | Controls testing | 20 days | Fri 1/29/16 | Fri 2/26/16 |
| 226 | RFB | 1 day | Fri 2/26/16 | Mon 2/29/16 |
| 227 | **XS2 (SASE2)** | **68 days** | **Tue 9/1/15** | **Fri 12/4/15** |
| 228 | Drilling holes + concrete work | 2 days | Tue 9/1/15 | Thu 9/3/15 |
| 229 | Transport of Material | 5 days | Thu 9/3/15 | Thu 9/10/15 |
| 230 | E-racks | 5 days | Thu 9/10/15 | Thu 9/17/15 |
| 231 | Stands | 5 days | Thu 9/17/15 | Thu 9/24/15 |
| 232 | UHV beam pipes | 10 days | Thu 9/24/15 | Thu 10/8/15 |
| 233 | UHV optics components | 10 days | Thu 10/8/15 | Thu 10/22/15 |
| 234 | UHV pump down&testing | 10 days | Thu 10/22/15 | Thu 11/5/15 |
| 235 | Controls testing | 20 days | Thu 11/5/15 | Thu 12/3/15 |
| 236 | RFB | 1 day | Thu 12/3/15 | Fri 12/4/15 |
| 237 | **XTD6 (SASE2)** | **151 days** | **Tue 9/1/15** | **Wed 3/30/16** |
| 238 | Drilling holes + concrete work | 10 days | Tue 9/1/15 | Tue 9/15/15 |
| 239 | Transport of Material | 10 days | Tue 9/15/15 | Tue 9/29/15 |
| 240 | E-racks | 20 days | Tue 9/29/15 | Tue 10/27/15 |
| 241 | Stands | 20 days | Tue 10/27/15 | Tue 11/24/15 |
| 242 | UHV beam pipes | 30 days | Tue 11/24/15 | Tue 1/5/16 |
| 243 | UHV optics components | 30 days | Tue 11/24/15 | Tue 1/5/16 |
| 244 | UHV diagnostics | 20 days | Tue 1/5/16 | Tue 2/2/16 |
| 245 | UHV pump down&testing | 30 days | Tue 2/2/16 | Tue 3/15/16 |
| 246 | Controls testing | 10 days | Tue 3/15/16 | Tue 3/29/16 |
| 247 | RFB | 1 day | Tue 3/29/16 | Wed 3/30/16 |
| 248 | **Commisioning** | **177 days** | **Mon 9/21/15** | **Wed 5/25/16** |
| 249 | SASE1 | 40 days | Mon 9/21/15 | Mon 11/16/15 |
| 250 | SASE3 | 40 days | Mon 9/21/15 | Mon 11/16/15 |
| 251 | SASE2 | 40 days | Wed 3/30/16 | Wed 5/25/16 |
| 252 | **Outgoing Milestones** | **178 days** | **Mon 9/21/15** | **Thu 5/26/16** |
| 253 | first beam through SASE1 | 1 day | Mon 9/21/15 | Tue 9/22/15 |
| 254 | user beam SASE1 | 1 day | Mon 11/16/15 | Tue 11/17/15 |
| 255 | first beam through SASE3 | 1 day | Mon 9/21/15 | Tue 9/22/15 |
| 256 | user beam SASE3 | 1 day | Mon 11/16/15 | Tue 11/17/15 |
| 257 | first beam through SASE2 | 1 day | Wed 3/30/16 | Thu 3/31/16 |
| 258 | user beam SASE2 | 1 day | Wed 5/25/16 | Thu 5/26/16 |

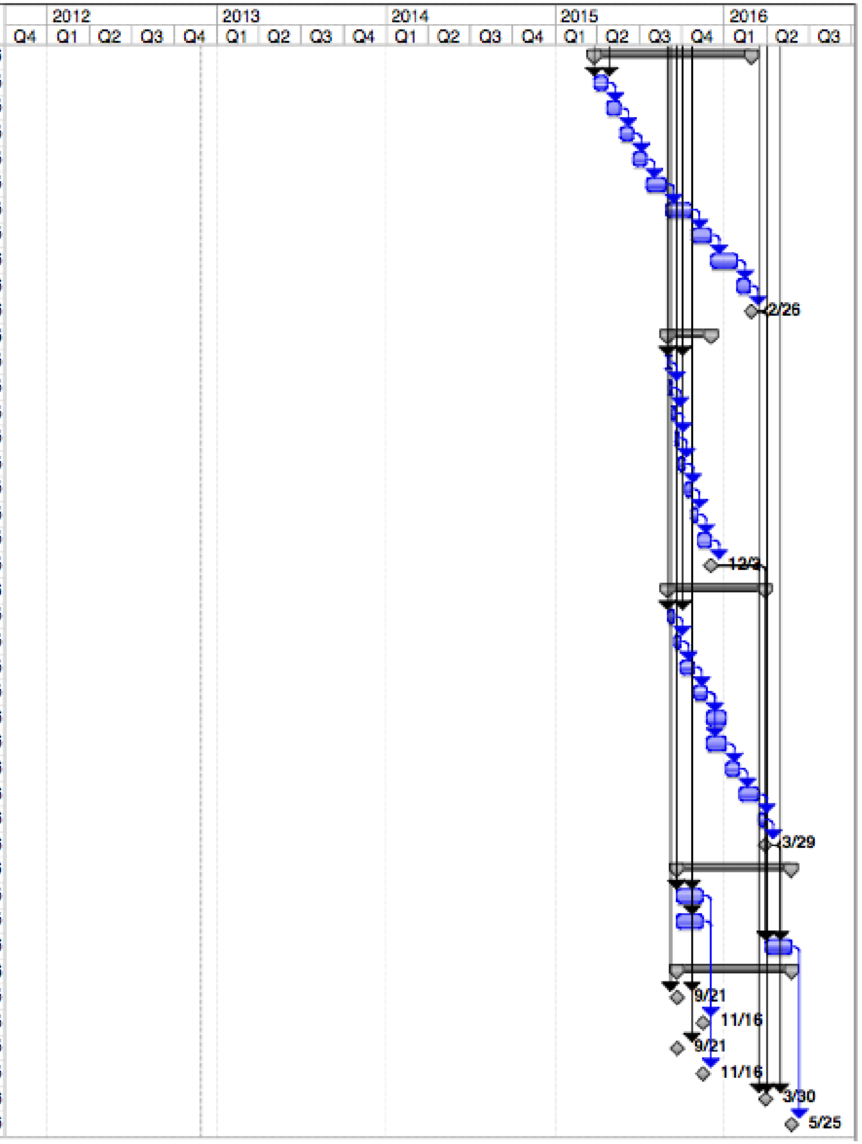

# References

[1] H. Sinn et al.: “Conceptual Design Report: X-Ray Optics and Beam Transport”, XFEL.EU TR-2011-002 (2011)

[2] T. Leitner et al.: “Shot-to-shot and average absolute photon flux measurement of a femtosecond laser high-order harmonic photon source”, New Journal of Physics **13**, 093003 (2011)

[3] R. Brinkmann, E.A. Schneidmiller, M.V. Yurkov, “Possible Operation of the European XFEL with Ultra-Low Emittance Beams”, Nucl. Instrum. Meth. A 616, 81 (2010).

[4] J. Gaudin et al.: “Amorphous to crystalline phase transition in carbon induced by intense femtosecond x-ray free-electron laser pulse”, Physical Review B 86, 024103 (2012)

[5] J. Gaudin et al: “Investigating the interaction of x-ray free electron laser radiation with laminar grating structure”, Optics Letters, 37, 3033–3035, 15 (2012)

[6] S. Rutishauser et al.: "Exploring the wavefront of hard x-ray laser radiation", Nature Communications 3, 947, DOI: 10.1038/ncomm1950 (2012)

[7] S. Berujon et al, Physical Review Letters 108, 158102 (2012).

[8] F. Siewert, et al.: “Ultra-precise characterization of LCLS hard Xray focusing mirrors by high resolution slope measuring deflectometry”, Optics Express 20, 4525, 4 (2012)

[9] T. Noll, K. Holldack, G. Reichardt, et al.: “Parallel kinematics for nanoscale Cartesian motions”, Precision Engineering 33 , 291–304 (2009)

[10] Patents:
WO 02/16092 A1: “Device for Multi-Axis fine Adjustable Bearing of a Component”, T. Noll, W. Gudat, H. Lammert, 2001
DE 100 42 801.0: “Flexibles Gelenk hoher axialer Steifigkeit”, T. Noll, W. Gudat, (2000)
DE 200 15 988.7: “Spindelantrieb zur hochgenauen Positionierung eines linear zu verschiebenden Bauteils”, T. Noll, H. Lammert, W. Gudat, (2000)

[11] T. Noll: “Flexure Joints of High Axial Stiffness”, Precision Engineering 26, 460–465 (2002)

[12] T. Noll, “Elastische parallelkinematische Führungsgetriebe für ultrapräzise Bewegungen im Vakuum", PhD thesis, Technical University Berlin (2003)

[13] J. Linnemann, Bachelor thesis, Universität Emden (2011)

[14] M.D. Roper, NIMA, A635 S80–S87 (2011)

[15] M.R. Howells, “X-ray Data Booklet”, Chapter 4.3, Lawrence Berkeley National Laboratory, xdb.lbl.gov (2008)

[16] R. Soufli et al.: “Development and calibration of mirrors and gratings for the soft x-ray materials science beamline at the LCLS free-electron laser”, Applied Optics, 51 (2012)

[17] M. Dommach: “UHV Guidelines for X-Ray Beam Transport Systems”, XFEL.EU TN-2011-001-02 (2011)

[18] J. Bahrdt, U. Flechsig S. Gerhard, I. Schneider, PHASE: “A Universal Software Package for the Propagation of Time-Dependent Coherent Light Pulses along Grazing Incidence Optics”, Proc. of SPIE, 8141 81410E-1 (2011)

[19] L. Samoylova, et al.: “Requirements on hard x-ray grazing incidence optics for European XFEL: analysis and simulation of wavefront transformations”, SPIE Proceedings, 7360, EUV and X-Ray Optics: Synergy between Laboratory and Space, R. Hudec; L. Pina, Editors, 73600E (2009) DOI: 10.1117/12.822251

[20] F. Siewert: Private communication (2011)

[21] ISO 14644-1 cleanroom standard

[22] B.L. Henke, E.M., Gullikson, J.C. Davis: “X-Ray Interactions: Photoabsorption, Scattering, Transmission, and Reflection at E = 50-30,000 eV, Z = 1-92”, Atomic Data and Nuclear Data Tables, 54, 181–342, 2

[23] A. Madsen, at al.: “Conceptual Design Report: Scientific Instrument MID”, XFEL.EU TR-2011-008 (2011)

[24] Ch. Bressler et al.: “Conceptual Design Report: Scientific instrument FXE”, XFEL.EU TR-2011-005 (2011)

[25] X.R.Vision 2.0 is a simulation program for X-ray sources and optics and SpotX a program for ray tracing. Both were developed by Caminotec (Thierry Moreno <thierry.moreno@synchrotron-soleil.fr>, +33-0145841171). They are similar to the widely used programs of XOP/ShadowVUI.

[26] S. Narayanan, A. Sandy, D. Shu et al.: “Design and performance of an ultra-high-vacuum compatible artificial channel-cut monochromator”, J. Synchrotron Rad. 15, 12–18 (2008)

[27] D. Shu, Narayanan, A. Sandy, et al.: “Precision mechanical design of an UHV-compatible artificial channel-cut X-ray monochromator”, Proc. SPIE 6665, 66650O-1 (2007)

[28] D. Shu T.S. Toellner, E.E. Alp, US Patent granted No. 6,607,840 (2003)

[29] Test report from manufacturer ALCA technology, s.r.l

[30] TISNCM –Technological Institute for Superhard and Novel Carbon Materials http://www.ntcstm.troitsk.ru/en/about.html

# Acknowledgements

Apart from those listed in the author list, other people from WP73 contributed material to this TDR: Idoia Freijo, Antje Trapp, Nicole Kohlstrunk, Jens Linnemann, Germano Galasso, Tommaso Molaro, Jérôme Gaudin, Alexander Bartmann, Timo Korsch, Bianca Dickert, Massimiliano de Felice, and Shafagh Dastjani Farahani. Special thanks also to Tino Noll from HZB for the development of the prototype mirror chamber, Deming Shu from Argonne National Laboratory for the development of the hard X-ray monochromator, Riccardo Signorato from Bruker ASC for the ongoing development of the adaptive mirror prototype and many discussion about possible and impossible X-ray mirrors, Rolf Follath from HZB for ray-tracing calculations, guidance, and discussions during the development of the soft X-ray monochromator, Frank Siewert for discussions on mirror and grating specifications and the provision of metrology data, and Igor Kozhevnikov from IC RAS, Moscow, for discussions and contributions concerning roughness effects.

Thanks to people from European XFEL who stimulated with many fruitful discussions the developments described here in the TDR and contributed with corrections in the manuscript: Thomas Tschentscher, Serguei Molodtsov, Jan Grünert and his group members, the instrument scientists Adrian Mancuso, Christian Bressler, Michael Meyer, Anders Madsen and Andreas Scherz and their group members, Chris Youngman, Nicola Coppola, and Tobias Haas. Thanks to Kurt Ament and Ilka Flegel for editing the manuscript.

Thanks to colleagues from DESY who were and are involved in many discussions concerning the interfaces and technical realization: Sven Lederer, Martin Staak, Winfried Decking, Dirk Noelle, Albrecht Leuschner, Brunhilde Racky, Kai Rehlich, Johannes Prenting, Jens-Peter Jensen and Norbert Meyners.

Thanks to the ART committee for valuable input during the CDR and TDR reviews: Christian Schroer, Edgar Weckert, John Arthur, Rolf Follath, Timm Weitkamp, Aymeric Robert, Horst Schulte-Schrepping, and Ray Barrett. Finally, our thanks go to the European XFEL management and all other

European XFEL and DESY employees not mentioned explicitly for creating a pleasant working atmosphere.